2023

# Characterizing & Mitigating Interstellar Scattering in Radio Observations of Pulsars

Jacob E. Turner
*West Virginia University*, jet0027@mix.wvu.edu

# Characterizing & Mitigating Interstellar Scattering in Radio Observations of Pulsars

**Jacob E. Turner**

**Dissertation submitted to the Eberly College of Arts & Sciences at West Virginia University in partial fulfillment of the requirements for the degree of PhD in The Department of Physics & Astronomy**

Dr. Maura McLaughlin, Research Advisor/Committee Chair

Dr. Dan Stinebring, Research Advisor

Dr. Duncan Lorimer, Committee Member

Dr. Loren Anderson, Committee Member

Department of Physics & Astronomy

Morgantown, West Virginia

2023

Keywords: Pulsars, gravitational waves, interstellar medium

# Abstract


## Characterizing & Mitigating Interstellar Scattering in Radio Observations of Pulsars

Jacob Turner

Pulsars are rapidly rotating neutron stars that emit concentrated beams of radiation from their magnetic poles. Measuring the arrival of these pulses via pulsar timing is a powerful tool in efforts to detect low frequency gravitational waves (GWs). However, the interstellar medium (ISM) presents a significant source of timing uncertainty that must be mitigated to improve the sensitivity of pulsar timing efforts to these GW signals. By examining the effects of pulsar emission interactions with this medium, we can properly correct for the resulting effects in pulsar timing efforts, as well as study the astronomical unit-to-parsec scale structure and behavior of the ISM and characterize this medium across many lines of sight in our Galaxy and localize the regions that dominate these interactions. Emerging data processing techniques that take advantage of the periodic nature of pulsar signals are also now allowing us to probe these features with incredible resolution. This thesis serves to highlight some valuable studies related to understanding the structure and behavior of the ionized ISM via the interstellar scattering of pulsar emission.

To examine scattering behavior across many lines of sight, we extract interstellar scintillation parameters for pulsars observed by the North American Nanohertz Observatory for Gravitational Waves (NANOGrav) radio pulsar timing program in the 12.5 year data release. We find good agreement between our scattering delay measurements and electron-density model predictions for most pulsars. For most pulsars for which scattering delays are measurable, we find that time-of-arrival uncertainties for a given epoch are larger than our scattering delay measurements, indicating that variable scattering delays are currently subdominant in our overall noise budget but are important for achieving precisions of tens of nanoseconds or less.

Next, we use the Upgraded Giant Metrewave Radio Telescope to measure scintillation arc properties in six bright canonical pulsars with simultaneous dual frequency coverage. We perform more robust determinations of arc curvature, scattering delay, and scintillation timescale frequency-dependence, and comparison between arc curvature and pseudo-curvature than allowed by single-frequency-band-per-epoch measurements, which we find to agree with theory and previous literature. We find a strong correlation between arc asymmetry and arc curvature, which we have replicated using simulations, and attribute to a bias in the Hough transform approach to scintillation arc analysis.

We then simulate scattering delays from the ISM to examine the effectiveness of three estimators in recovering these delays in pulsar timing data. Two of these estimators use the more traditional process of fitting autocorrelation functions (ACFs) to pulsar dynamic spectra to extract scintillation bandwidths, while the third estimator uses the newer technique of cyclic spectroscopy on baseband pulsar data to recover the ISM's impulse response function (IRF). We find that, given sufficient S/N, cyclic spectroscopy is more accurate than both ACF estimators at recovering scattering delays at specific epochs, suggesting that cyclic spectroscopy is a superior method for scattering estimation in high quality data.

Finally, we use cyclic spectroscopy to perform high frequency-resolution, frequency dependent analyses of the millisecond pulsar B1937+21. We present among the most robust intra-epoch scattering delay scaling estimations performed at 1.4 GHz, using eight individual measurements across our observing bands, and find our results to agree with those previously quoted in the literature.

# Acknowledgments

This thesis would not be possible without years of support from many people. I would first and foremost like to thank Maura McLaughlin and Dan Stinebring for helping me to become the scientist I am today. Simply put I would not have made it to grad school without Dan's willingness to take me on as a research assistant in undergrad and provide me with such an abundance of opportunities and an incredible collaborative network (thank you for everything you have done for me, NANOGrav). Maura has been an invaluable mentor, providing me with the guidance necessary for me to transform from a data analyst that can follow directions into a fully independent researcher. I am eternally grateful for the confidence and ability you have instilled in me.

Thank you to Bhal Chandra Joshi for your mentorship and the many late night (for me)/early morning (for you) zoom calls as we worked through and analyzed our GMRT observations. I hope we continue to work together for many years to come.

Thank you to Ryan Lynch for helping me get acquainted with the exciting field of cyclic spectroscopy and for giving me such an incredible opportunity for the next stage of my career. I look forward to working closely with you over the next few years as we see the GBO CS pipeline through to being fully operational.

I would like to thank my parents, Kevin and Lisa Turner, and brother, Dylan Turner, for their constant love, support, and encouragement, especially when I was at my lowest and questioning whether a career in astrophysics was the right path for me. Your continued push for me to pursue my passions is why I have never given up despite the many instances where it would have been very easy to just call it quits and change career paths.

Thank you to my close friends Sid Mahesh, Dylan Linville, and Tyler Gilbert for helping in the daunting task of making grad school an enjoyable experience. Our many nights of team trivia (Go Quizzicists!) and D&D were some of my fondest memories of the past five years and a much needed break from the occasionally demoralizing problem sets and research roadblocks.

Thank you to my partner Erica Kushner for your endless love and support over the past 4.5 years. You have helped ground me through countless periods of stress and anxiety and I truly could not have made it to this point without you by my side.

Lastly, thank you to my grandfather and biggest cheerleader Earl Goldberg for your love and your unwavering confidence that I would succeed. I am so glad you were able to see me live out my dreams.

# Dedication

To my #1 fan Earl Goldberg. Thank you for your endless love.

# Table of Contents

**Abstract** . . . . . **ii**

**Acknowledgments** . . . . . **iii**

**Dedication** . . . . . **iv**

**Table of Contents** . . . . . **viii**

**List of Figures** . . . . . **ix**

**List of Tables** . . . . . **xii**

**Chapter 1. Introduction** . . . . . **1**

1.1 Pulsars . . . . . 1

1.2 Pulsar Timing . . . . . 2

1.3 Interstellar Medium . . . . . 5

1.3.1 Dispersion . . . . . 6

1.3.2 Scattering . . . . . 9

1.3.3 Cyclic Spectroscopy . . . . . 15

1.3.4 Scintillation Arcs . . . . . 19

1.4 Thesis Overview . . . . . 22

**Chapter 2. The NANOGrav 12.5-Year Data Set: Monitoring Interstellar Scattering Delays** . . . . . **24**

2.1 Introduction . . . . . 24

2.2 Data . . . . . 26

2.3 Analysis . . . . . 27

2.3.1 Scintillation Parameters . . . . . 27

2.3.2 Scaling Behavior . . . . . 38

2.3.3 Transverse Velocities . . . . . 41

2.4 Results . . . . . 42

2.4.1 Scintillation Parameters and Variations . . . . . 42

2.4.2 Scaling over Multiple Frequency Bands . . . . . 51

2.4.3 Transverse Velocity Measurements . . . . . 53

2.5 Discussion . . . . . 57

2.5.1 Scattering Variability and Correlations with Dispersion Measure & Flux Density Variations . . . . . 57

2.5.2 Measuring Scaling Indices . . . . . 64

2.5.3 Transverse Velocity Measurements . . . . . 67

2.5.4 Scaling of Scattering Delay with DM . . . . . 71

2.6 Conclusions . . . . . 74

**Chapter 3. A Simultaneous Dual-Frequency Scintillation Arc Survey of Six Bright Canonical Pulsars Using the Upgraded Giant Metrewave Radio Telescope . . . . . 78**

3.1 Introduction . . . . . 78

3.2 Data . . . . . 80

3.3 Analysis . . . . . 81

3.4 Results & Discussion . . . . . 83

3.4.1 Scintillation Arc Curvature Scaling Behavior . . . . . 83
3.4.2 Scintillation Bandwidth & Scintillation Timescale Scaling Behavior 87
3.4.3 Relation Between Arc Curvature and Scintillation Parameters . . 93
3.4.4 155 Minute Observation . . . . . 98
3.4.5 J0630-2834 . . . . . 99
3.4.6 J1136+1551 . . . . . 101
3.4.7 J1509+5531 . . . . . 105
3.4.8 J1645-0317 . . . . . 107
3.4.9 J1932+1059 . . . . . 108
3.4.10 J2048-1616 . . . . . 112
3.5 Conclusions & Future Work . . . . . 112

**Chapter 4. Scattering Delay Mitigation in High Accuracy Pulsar Timing: Cyclic Spectroscopy Techniques . . . . . 115**

4.1 Introduction . . . . . 115
4.2 Theoretical Basics . . . . . 117
4.3 Simulation Methodology . . . . . 119
4.4 Simulation Results . . . . . 123
4.5 Conclusions and Future Developments . . . . . 137

**Chapter 5. A Cyclic Spectroscopy-Aided Scintillation Study of Multi-Hour L-Band Observations of PSR B1937+21 I. Intra-Epoch Frequency Evolution . . . . . 141**

5.1 Introduction . . . . . 141
5.2 Data . . . . . 145
5.3 Analyses . . . . . 145

5.4 Results & Discussion . . . . . 149

5.4.1 Scintillation Bandwidth Measurements & Scaling . . . . . 149

5.4.2 Scintillation Arcs . . . . . 151

5.5 Conclusions & Future Work . . . . . 156

**Chapter 6. Conclusions** . . . . . **159**

6.1 Assessing the Effects of Scattering Delays Within NANOGrav Data . . . . 159

6.2 Studying Scintillation Arcs Using Simultaneous Dual-Frequency Observations 160

6.3 Determining the Effectiveness of Cyclic Spectroscopy at Recovering Scattering Delays in Pulsar Timing Data . . . . . 161

6.4 Using Cyclic Spectroscopy to Reveal Rich Scintillation Information In L-Band Observations of a Millisecond Pulsar . . . . . 162

6.5 Looking to the Future . . . . . 162

**References** . . . . . **164**

**Appendix A: Derivation of Fractional Error and Uncertainty As Related To Observable Quantities** . . . . . **174**

# List of Figures


1.1 Pulsar period-period derivative diagram . . . 3
1.2 Predicted vs measured Hellings & Downs correlations . . . 5
1.3 Comparison of uncorrected vs corrected pulsar signal affected by dispersion . . 8
1.4 Example dynamic spectrum . . . 11
1.5 Illustration of propagation of pulsar emission through interstellar medium . . . 12
1.6 Example of pulse profile evolution over observing frequency . . . 13
1.7 Simulated cyclic spectrum . . . 17
1.8 Example of a recovered impulse response function and instrinsic pulse . . . 17
1.9 Dynamic spectrum processed with and without cyclic spectroscopy . . . 18
1.10 Example secondary spectrum with multiple scintillation arcs . . . 20
1.11 Example scintillation arc . . . 22

2.1 Example dynamic spectrum with corresponding 2D and 1D ACFs . . . 30
2.2 Dynamic spectrum example with corresponding 2D and 1D ACFs . . . 33
2.3 Subband scattering delay scaling index fit . . . 39
2.4 Example scattering delay scaling index plot over both observing bands . . . 40
2.5 Scattering delay, flux density, and dispersion measure timeseries . . . 48
2.6 Example dynamic and secondary spectra . . . 49
2.7 Secondary spectrum power dissipation . . . 52
2.8 Comparison between transverse velocities derived from proper motion and scintillation parameters . . . 54
2.9 Semi-log comparisons of pulsar scattering delay and flux density variability . . 68
2.10 Scattering delay scaling index timeseries for PSR J2010-1323 . . . 69
2.11 Scattering delay scaling index timeseries for PSR B1855+09 . . . 69
2.12 Measured average scattering delays vs predicitions by NE2001 electron density model . . . 72
2.13 Measured average scattering delays vs dispersion measure compared with various model fits . . . 73

3.1 Example fits for the arc curvature scaling index . . . . . 85
3.2 Example scaling index fits . . . . . 90
3.3 Example comparison between $\eta_{\rm ISS}$ and $\eta$ for PSR J1136+1551 on MJD 58991 . 94
3.4 Comparison of scintillation scaling indices to arc curvature correlation coefficients 95
3.5 Example dynamic and secondary spectrum for PSR J0630-2834 . . . . . 100
3.6 Example of secondary spectrum with multiple scintillation arcs . . . . . 101
3.7 Example dynamic and secondary spectrum for PSR J1136+1551 . . . . . 104
3.8 Normalized secondary spectrum power profile of PSR J1136+1551 . . . . . 105
3.9 Comparison of simulated and measured asymmetry indices as a function of arc curvature . . . . . 106
3.10 Example dynamic and secondary spectrum for PSR J1509+5531 on MJD 58987 107
3.11 Example dynamic and secondary spectrum for PSR J1509+5531 on MJD 59115 108
3.12 Example dynamic and secondary spectrum for PSR J1645-0317 . . . . . 109
3.13 Example dynamic and secondary spectrum for PSR J1932+1059 . . . . . 111
3.14 Example dynamic and secondary spectrum for PSR J2048-1616 . . . . . 113

4.1 Example normalized simulated cyclic spectrum . . . . . 121
4.2 Example simulated cyclic phase . . . . . 124
4.3 Injected and recovered IRF and corresponding residuals . . . . . 125
4.4 Example recovered frequency ACF and fits . . . . . 126
4.5 Average recovered delay as a function of S/N using cyclic spectrum estimator . 127
4.6 Average recovered delay as a function of S/N using ACF estimators . . . . . 129
4.7 Average fractional error as a function of injected delay for all estimators . . . . 132
4.8 Timeseries of injected and recovered delays for all estimators . . . . . 133
4.9 Injected vs recovered delay for all estimators over 1000 realizations at S/N of 10 134
4.10 Correlation between injected and recovered delays for cyclic spectrum estimator 136
4.11 Correlation between injected and recovered delays for ACF estimators . . . . . 138
4.12 Absolute differences, $|z|$, between the various estimators and $\tau_{\rm cent}$ as a function of the average injected scattering delay, $\tau$ . . . . . 139

5.1 Dynamic spectrum before and after processing using cyclic spectroscopy . . . . 146
5.2 Example dynamic spectrum with corresponding ACFs . . . . . 148

5.3 Example fit for scattering delay scaling index on MJD 56206 . . . . . 151
5.4 Example scintillation arcs with overlaid fits . . . . . 152
5.5 Asymmetry index vs observing frequency on MJD 56206 . . . . . 154
5.6 Scintillation arc curvature scaling indices in both arms on MJD 56183 . . . . . 157

# List of Tables


2.1 Measured Scintillation Parameters . . . . . 31
2.1 Measured Scintillation Parameters . . . . . 32
2.2 NE2001 Electron Density Model Predicted Scintillation Parameters . . . . . 34
2.2 NE2001 Electron Density Model Predicted Scintillation Parameters . . . . . 35
2.2 NE2001 Electron Density Model Predicted Scintillation Parameters . . . . . 35
2.3 Comparison with Previously Published Scintillation Parameters . . . . . 37
2.3 Comparison with Previously Published Scintillation Parameters . . . . . 38
2.3 Comparison with Previously Published Scintillation Parameters . . . . . 38
2.4 Estimated Scattering Delay Scaling Indices . . . . . 54
2.4 Estimated Scattering Delay Scaling Indices . . . . . 55
2.4 Estimated Scattering Delay Scaling Indices . . . . . 55
2.5 Pulsar Transverse Velocities Inferred from Interstellar Scattering and Proper Motions . . . . . 56
2.5 Pulsar Transverse Velocities Inferred from Interstellar Scattering and Proper Motions . . . . . 57
2.5 Pulsar Transverse Velocities Inferred from Interstellar Scattering and Proper Motions . . . . . 57
2.6 Scattering Delay Trends & Correlations . . . . . 62
2.6 Scattering Delay Trends & Correlations . . . . . 63
2.6 Scattering Delay Trends & Correlations . . . . . 63

3.1 Pulsars Observed . . . . . 80
3.1 Summary of pulsar observations. . . . . 81
3.2 Fitted Pulsar Scintillation Arc Curvature Scaling Indices . . . . . 86
3.2 Fitted Pulsar Scintillation Arc Curvature Scaling Indices . . . . . 86
3.3 Fitted Pulsar Scintillation Bandwidth & Scintillation Timescale Scaling Indices 91
3.3 Fitted Pulsar Scintillation Bandwidth & Scintillation Timescale Scaling Indices 92
3.3 Fitted Pulsar Scintillation Bandwidth & Scintillation Timescale Scaling Indices 92
3.4 Relation Between $\eta$ and $\eta_{\rm ISS}$ . . . . . 96

3.4 Relation Between $\eta$ and $\eta_{\rm ISS}$ . . . . . 97
3.4 Relation Between $\eta$ and $\eta_{\rm ISS}$ . . . . . 97

5.1 Fitted Pulsar Scattering Delay Scaling Indices . . . . . 150
5.1 Fitted Pulsar Scattering Delay Scaling Indices . . . . . 150
5.2 Fitted Pulsar Scintillation Arc Curvature Scaling Indices . . . . . 155
5.2 Fitted Pulsar Scintillation Arc Curvature Scaling Indices . . . . . 156

# Chapter 1. Introduction

## 1.1 Pulsars

Pulsars are rotating neutron stars that form within core-collapse supernovas of massive stars between 10–25 $M_{\odot}$ (Heger et al., 2003). Believed to have among the strongest magnetic fields of any object in the universe (Güver et al., 2007), these stars act as spinning magnetic dipoles, accelerating electrons along curved magnetic field lines. It is theorized that this acceleration causes these electrons to emit high-energy curvature radiation, and as these resulting photons interact with the magnetic field and lower-energy photons, electrons-positron pairs are produced, in turn creating more high-energy radiation, creating a cascade of radiation-emitting charged particles (Ruderman & Sutherland, 1975). This results in groups of charged particles emitting radio waves, eventually leading to the coherent beam of synchrotron emission from the pulsar's magnetosphere at the magnetic poles which we observe. If these beams sweep across our line of sight, they can be observed as a pulsed signal, which is observed to be periodic in most cases. However, many instances of signals turning off for periods of time (nulling) (Backer, 1970), as well as giant pulses (Staelin & Reifenstein, 1968), with signals many times stronger than a typical observed pulse, and pulsars with incredibly sporadic pulses (RRATs) (McLaughlin et al., 2006), or pulsars with no discernable periodicity, have also been observed. Pulsars originating from the scenario described above, known as canonical pulsars, typically have observed periods ranging from around 20 ms $-$ 20 s (Dirson et al., 2022). An additional class of pulsars, known as recycled (Bisnovatyi-Kogan & Ruzmaikin, 1974) or millisecond pulsars (Backer et al., 1982), formed initially as in the scenario described above. However, they then underwent accretion-powered spin-up from material siphoned from a binary pulsar's companion

star. These pulsars can have spin periods ranging from around 1−30 ms (Kramer et al., 1998). Canonical pulsars have period derivatives, or spin-down rates, ranging from $10^{-12} - 10^{-18}$ s s$^{-1}$; millisecond pulsar spin-down rates are considerably smaller, with rates around $10^{-19} - 10^{-21}$ s s$^{-1}$, as can be seen by examining a period-period derivative diagram like in Figure 1.1. Additionally, millisecond pulsars typically have wider pulses relative to their rotation periods and have characteristic average pulse shapes, also known as pulse profiles, that are remarkably stable over long periods of time, making them ideal candidates for high precision timing projects such as the search for and detection of nanohertz-frequency gravitational waves (Foster & Backer, 1990).

The flux density and features of pulses have been observed to change with frequency. At lower frequencies of the radio band, pulsars are observed to increase in flux density with increasing frequency, which is followed by a spectral turnover where the observed flux density gets progressively dimmer as one observes at increasingly higher frequencies, following power-law trends in both cases (O'Dell & Sartori, 1970; Rankin et al., 1970). Following the spectral turnover, the spectral index of this power law seems to vary widely between pulsars, ranging from as shallow as $\nu^{-0.4}$ down to $\nu^{-4}$, with the average spectral index being around $-1.4$ (Bates et al., 2013). Pulse profiles can undergo major structural changes depending on the observing frequency as well, with features gradually emerging or receding in many pulsars, although generally pulse widths tend to decrease and features tend to merge as we observe at progressively higher frequencies, although this effect appears to be less pronounced in millisecond pulsars (Kramer et al., 1998). This has been attributed to emission at different frequencies originating at varying heights above the surface of the neutron star (Komesaroff, 1970), with millisecond pulsars having smaller emission regions than canonical ones.

## 1.2 Pulsar Timing

The incredibly stable average profiles of millisecond pulsars make them valuable tools for high-precision science, and their being widely distributed throughout the Galaxy allows for

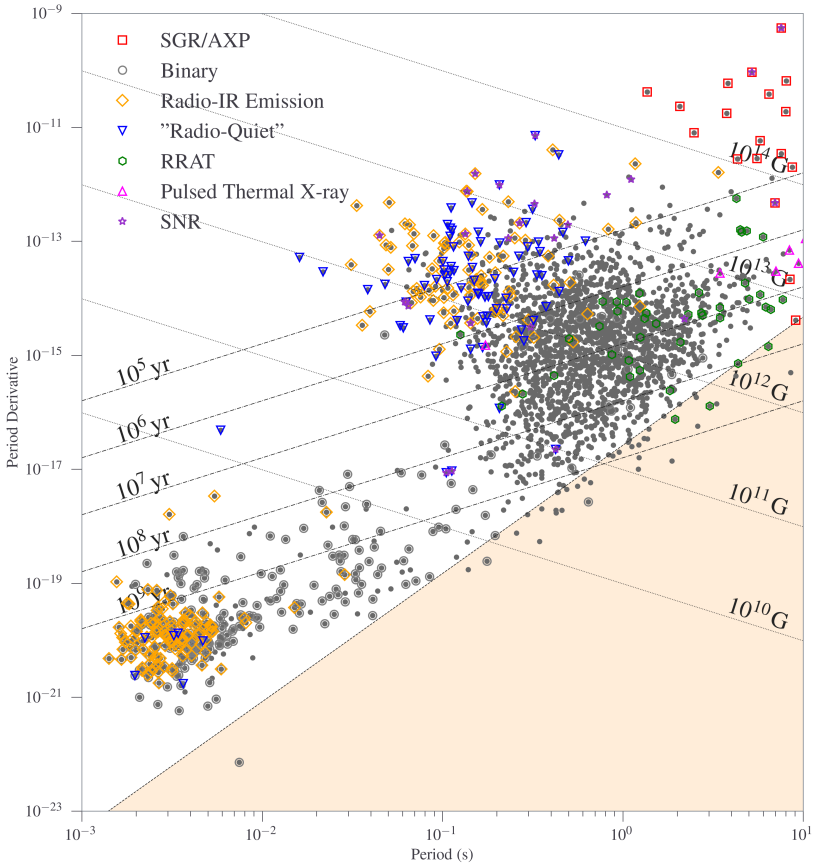


**Figure 1.1:** A period-period derivative diagram detailing a variety of physical properties for a wide range of pulsars using the most up-to-date data. Downward sloped lines represent pulsar magnetic field strength in Gauss, while the shallower upward sloped lines represent pulsar age in thousands, millions, or billions of years, and the steeper upward sloped lines represent rotational energy loss, also known as spin-down luminosity, in ergs $s^{-1}$. Pink triangles represent pulsars visible at X-ray/$\gamma$-ray frequencies. Gray circles represent pulsars in binary systems, while purple stars are pulsars with known associated supernova remnants. Red squares represent magnetars, a highly magnetized type of neutron star and green hexagons represent sporadically pulsing RRATs.

close examination of phenomena that may be dependent on both time and physical location. To develop a robust pulsar timing model, one needs to account for information intrinsic to the pulsar, such as period and period derivative, as well as all potential sources that could affect the expected arrival time of a pulse, including, but not limited to the distance, position on the sky, and motion of the pulsar, the motion and rotation of the Earth, the changing center of mass of the solar system, gravitational influence of any orbital companions to the pulsar, and material along the propagation path, primarily free electrons (see next section).

For a given observation, a pulse profile of the observed pulsar is created by summing over all pulses. These profiles are then compared with reference profiles, and the difference in phase can be converted into a time offset between the two. This offset is multiplied by a modeled pulse period and added to the midpoint time of the observation to determine the time of arrival (TOA; see e.g., Lommen & Demorest (2013)). The differences in the arrival time delay and the predicted delay from the timing model are known as timing residuals, and structure within the residuals can provide valuable information about information that was not included or properly corrected for in the model. For example, residuals that properly account for all sources of timing noise will appear uncorrelated over time, whereas an improperly corrected period derivative would result in quadratic residuals, or an improperly corrected proper motion would result in a gradually increasing sinusoid.

The characterization of timing residual structure is of vital importance for the goal of detecting nanohertz-frequency gravitational waves, as a gravitational wave propagating through spacetime between Earth and a given pulsar will cause perturbations in pulse arrival times that are dependent on what portion of the gravitational wave is interacting with that Earth-pulsar system at the instant of observation. As an Earth-pulsar system is observed over many years, different portions of the gravitational wave will influence the system, resulting in changes in these residuals that are correlated in time, creating a red noise signature in the data. Since each unique Earth-pulsar system in our detector will interact with a different portion of the gravitational wave signal at a given time, we expect the existence of these waves to manifest in the structure of the timing residuals as red noise that is correlated across all pulsars and

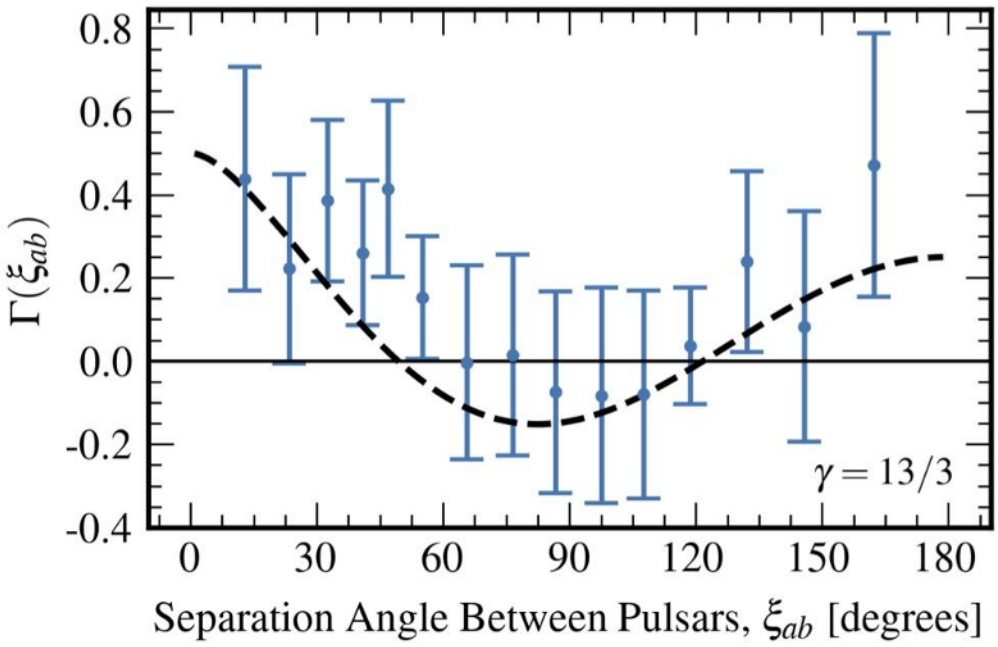


**Figure 1.2:** Predicted (dashed black curve) vs. measured (blue points) correlations between the timing residuals of pulsar pairs from the 15 year data release of the North American Nanohertz Observatory for Gravitational Waves (NANOGrav) pulsar timing array collaboration as a function of those pairs' angular separation on the sky (Agazie et al., 2023a). The results shown above represent evidence for a gravitational wave background at least $3\sigma$ significance.

changes with pulsar location on the sky (Foster & Backer, 1990). Evidence for the existence of a background of such gravitational waves as seen through these spatial correlations was recently confirmed, as can be seen in Figure 1.2 (Agazie et al., 2023a).

## 1.3 Interstellar Medium

Pulsars can serve as valuable probes of the interstellar medium (ISM), which comprises all space between the stars in our Galaxy. The interactions between pulsar emission and this medium during the signal's propagation towards Earth affects both the propagation path and

the coherence of the received signal, providing what could be argued as one of the best tools for examining from sub-AU up to parsec-scale structures within the medium.

### 1.3.1 Dispersion

While mostly empty, the matter that permeates the ISM consists of gas, mostly in the form of molecular and atomic hydrogen, dust, as well as charged particles, such as free electrons and ionized hydrogen. For this reason, the ISM is classified as a plasma, and, consequently, pulsar emission will experience frequency-dependent delays as the result of charged particle interactions with the emission, introducing different refractive indices, $\mu = \sqrt{1 - (\nu_{\rm med}/\nu)^2}$, where $\nu_{\rm med}$ is the frequency of oscillations of particle density of the medium and $\nu$ is the observing frequency, to the propagation path relative to empty space, assumed to be a vacuum (Lorimer & Kramer, 2004).

In pulsar astronomy, we are primarily concerned with how pulsar emission interacts with free electrons in the ISM during its propagation to Earth. They are typically assumed to permeate the ISM at number densities of around $n_e \sim 0.03$ cm$^{-3}$ (Ables & Manchester, 1976). While the group velocity, $v_{\rm g}$, of a wave through a vacuum is simply the speed of light, $c$, with corresponding propagation time $t = d/c$, waves propagating through any non-vacuum medium such as the ISM will have a refractive index less than 1, meaning that the modified group velocity equation, $v_{\rm g} = c\mu$, will result in a group velocity less than $c$. This will result in a new propagation time of

$$t_{\rm non-vacuum} = \int_0^d \frac{{\rm d}l}{c\mu} \tag{1.1}$$

as a result of the delayed signal.

For a given dispersion measure, DM $= \int_0^d n_e {\rm d}l$, which represents the integrated column density of electrons along the propagation path, the corresponding delay $t_{\rm DM}$ at observing frequency $\nu$ relative to an undispersed signal can be found by substituting the plasma frequency, $\nu_{\rm p}$, as the frequency of the medium within the expression for refractive index and then taking difference between the vacuum and non-vacuum propagation times. Here, DM has units of pc

cm$^{-3}$ and the plasma frequency is expressed as $\nu_{\rm p} = \sqrt{e^2 n_e/\pi m_e}$, where $e$ and $m_e$ are the charge and mass of the electron, respectively. Under the assumption that the plasma frequency is much less than our observing frequency (for pulsar observations it is typically around five to six orders of magnitude smaller, so this is a good approximation),

$$t_{\rm DM} = \left[\int_0^d \frac{{\rm d}l}{c\mu}\right] - \frac{d}{c} \approx \frac{1}{c}\int_0^d \left[1 + \frac{1}{2}\left(\frac{\nu_{\rm p}}{\nu}\right)^2\right]{\rm d}l - \int_0^d \frac{{\rm d}l}{c} = \frac{e^2}{2\pi m_e c}\frac{\int_0^d n_e {\rm d}l}{\nu^2} = K\frac{\rm DM}{\nu^2}, \quad (1.2)$$

where $\nu$ is the observing frequency in MHz and $K$, known as the dispersion constant, is roughly $4.15\times10^3$ MHz$^2$ pc$^{-1}$ cm$^3$ s (Lorimer & Kramer, 2004). This is one of the largest sources of delay that arise in pulsar timing, and we can see through a simple example that a nearby pulsar with a dispersion measure of 10 pc cm$^{-3}$ observed at a typical frequency of 1 GHz will have its signal delayed by 41.5 ms. Taking this a step further, if this pulsar were observed across L−band (which we shall henceforth use to refer to the band spanning 1.1–1.9 GHz in pulsar timing array observations), our detectors will measure around a 22.8 ms arrival time difference between the top and bottom of the band.

Left uncorrected, dispersion will result in a curved "dispersion sweep" when examining the pulsar signal's intensity across frequency and phase (see Figure 1.3). Since measurements are made using filterbanks with multiple discrete frequency channels, a simple way to fix this, known as incoherent dedispersion, is by calculating the difference in expected arrival time at a given frequency (in this case the frequency of a given frequency channel) relative to a reference frequency, typically the center of the observing band, and retroactively applying the negative of that delay offset. This technique, while useful, is inherently limited by the frequency channel width of the observation, i.e., the fact that the frequency channels have a width at all means they will retain some small level of delay related to dispersion, as we can only remove inter-channel delays in this way. This limits the time resolution to the inverse of the frequency channel width and can result in widened, smoothed out pulses, known as dispersive smearing, that are often unable to resolve the finer features of a fully resolved pulse. Taking a real world example, using NANOGrav's L-band frequency resolution of 1.5625 MHz frequency channels (Agazie et al.,

2023b), using incoherent dedispersion would limit us to a timing precision of approximately 130 $\mu$s at 1 GHz.

More advanced methods for dispersion measure correction also exist that examine the voltage phase of the signal in the frequency domain and model the dispersive effect as a transfer function of the ISM. In this way, the transfer function can be written in terms of a constant phase offset, a time domain delay, and a phase rotation of the signal that can be used to dedisperse the signal by taking its inverse. Since this technique, known as coherent dedispersion (Hankins & Rickett, 1975), is not limited by the frequency channel width of the observation, we can completely remove the dispersive delay from our signal without the side effect of dispersive smearing, which also results in finer time resolution of the pulse. Indeed, the benefits of this method over incoherent dedispersion make it the preferred dedispersion technique for all high-precision pulsar timing efforts.

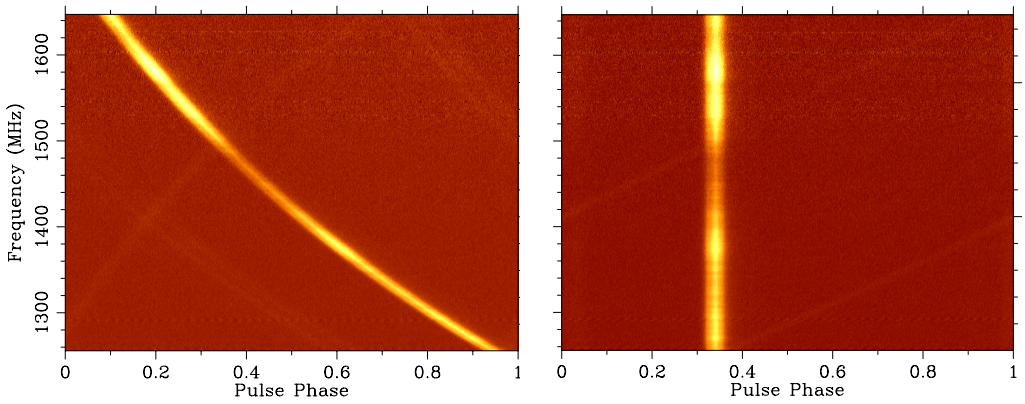


**(a)** Observation before dispersion is corrected. The quadratic sweep across the observation as a function of frequency is quite prominent, reflecting the disparate arrival time from data at opposite ends of the observing band.

**(b)** Observation after dispersion is corrected and removed. Signals from all frequencies are now aligned in phase.

**Figure 1.3:** An example observation of PSR J1744–1134 taken from Levin (2015) that demonstrates the effect dispersion has on arrival time as a function of frequency.

### 1.3.2 Scattering

In addition to the dispersion-based time delays associated with signal propagation through the interstellar medium, further changes to both the propagation time and the structure of the pulsar signal itself occur as the result of scattering interactions with smaller-scale inhomogeneities ($10^7 - 10^{10}$ cm for minutes-to-hours long timescale diffractive scattering and $10^{12} - 10^{15}$ cm for days-to-weeks long timescale refractive scattering (Stinebring et al., 2000a)), in the free electron density along the propagation path. Typically, this interaction is modeled as occurring at a thin screen of free electrons, usually halfway between the pulsar and the observer. As mentioned in the previous section, the refractive index $\mu$ of these free electrons is different than the surrounding medium, and as a result of this difference, pulsar emission passing through this screen will be phase-shifted by some amount $\delta\Phi = \Delta k a$, where $\Delta k = 2\pi\Delta\mu\nu/c$ is the wavenumber, or the number of wavelengths per unit distance, and $a$ is the length of a given inhomogeneity (Lorimer & Kramer, 2004). In the specific case of an ionized plasma, the refractive index yields a frequency-dependent phase shift of

$$\delta\Phi \approx \frac{2e^2 a \Delta n_e}{m_e c \nu}. \tag{1.3}$$

Following Hewish (1980), for a propagation distance $d$, we would expect a signal to pass through $d/a$ irregularities, resulting in rms phase deviations of

$$\Delta\Phi \approx \frac{2e^2 \Delta n_e \sqrt{ad}}{m_e c \nu}, \tag{1.4}$$

randomly distorting the wavefront by some angle $\theta_0$, approximated as $\Delta\Phi/ka$.

Due to the turbulent nature of the ISM, each photon will interact slightly differently with the phase screen, resulting in a multipath propagation of the signal and slightly different phase shifts for each photon. Consequently, we see this as an interference pattern evolving over both observing frequency and time at our telescopes in what are known as dynamic spectra (see Figure 1.4). These intensity fluctuations, a phenomenon known as scintillation, provide

us with an indirect way to quantify the amount of scattering in our data. When examining these fluctuations, we can see discrete structures, known as scintles, that demonstrate slices in frequency and time over which the pulsar signal has largely the same intensity. By quantifying over what ranges in frequency and time these structures appear, that is, their widths in frequency and time, known as the scintillation bandwidth ($\Delta\nu_{\rm d}$) and timescale ($\Delta t_{\rm d}$), respectively, we can determine the level of scintillation present in the data. If the intensity is similar over a large range of neighboring frequencies then that means not much scattering has occurred, resulting in wide scintles, a large scintillation bandwidth, and a small scattering delay. Conversely, if the intensity changes noticeably across neighboring observing frequencies, then that means a greater degree of scattering is taking place, leading to small scintles, a small scintillation bandwidth, and a large scattering delay. The same principle applies to the time axis with scintillation timescale.

As mentioned earlier, delays arise from phase shifts caused by pulsar emission traveling through regions with a frequency dependent index of refraction. This means a corresponding delay will be related to some fraction of the wavelength of a given ray, $\delta\Phi c/(2\pi\nu)$. Using the knowledge that interference from multipath propagation results from rays with phase differences of less than around 1 radian (Lorimer & Kramer, 2004), the bandwidth over which rays at a given frequency can interfere is in fact this scintillation bandwidth, also known as the decorrelation bandwidth, mentioned earlier. The full approximation for quantifying scattering delays in pulsar observations using this approach is consequently

$$\tau_{\rm d} \approx \frac{1}{2\pi\Delta\nu_{\rm d}}, \tag{1.5}$$

although in reality the numerator, usually represented as $C_1$, can vary from around $0.6-1.5$ depending on the geometry of the ISM (Lambert & Rickett, 2000).

In addition to the interference pattern phenomenon, another consequence of this multipath propagation of the signal is that the image we see will undergo angular broadening, with

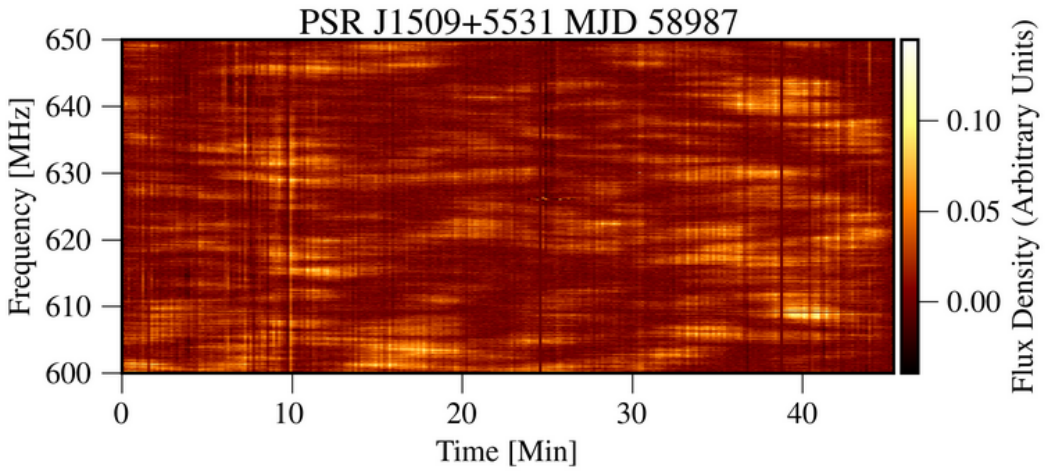


**Figure 1.4:** A dynamic spectrum of PSR J1509+5531 from Chapter 3. The large structures visible in the spectrum detailing the intensity fluctuations of the pulsar signal are a result of the multipath propagation of the signal through the ISM as a consequence of interstellar scattering.

a radial angular diffusion

$$\theta_{\rm d} = \theta_0/2 \approx \frac{e^2}{2\pi m_e} \frac{\Delta n_e}{\sqrt{a}} \frac{\sqrt{d}}{\nu^2}, \tag{1.6}$$

where $\theta_d$ is the angle of the broadened image, resulting in an angular intensity that varies with the incidental propagation angle at the observer as

$$I(\theta)d\theta \propto e^{-(\theta/\theta_d)^2} 2\pi\theta d\theta, \tag{1.7}$$

with an angle of zero indicating a signal unimpeded or undeflected during its propagation (Lorimer & Kramer, 2004). See Figure 1.5 for an illustrative aid detailing the above described phenomena.

A significant ramification of the angular broadening is that the signal itself is smeared out in a process known as scatter broadening. This effect is frequency-dependent (see Figure 1.6), and we can see the pulse gets increasingly stretched out in phase as we go to lower frequencies. More specifically, by taking the equation for geometric time delay, $t = \theta^2 d/c$,

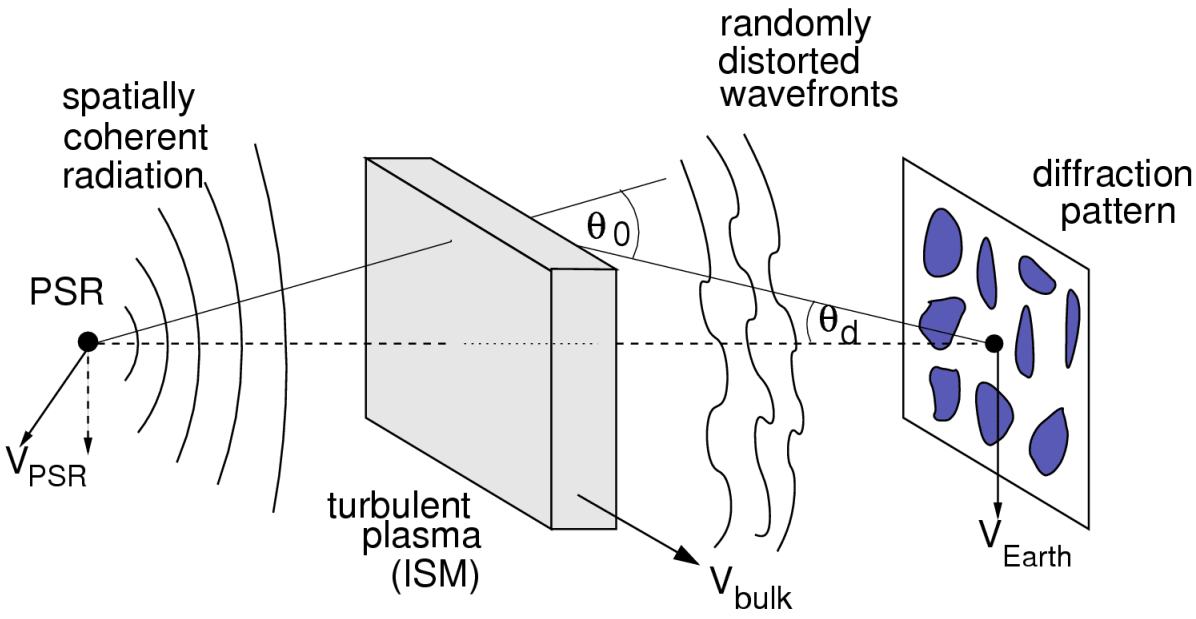


**Figure 1.5:** An illustrative guide to the propagation process of the pulsar signal through the interstellar medium and the corresponding effects of the signal once it reaches the observer (Cordes, 2002).

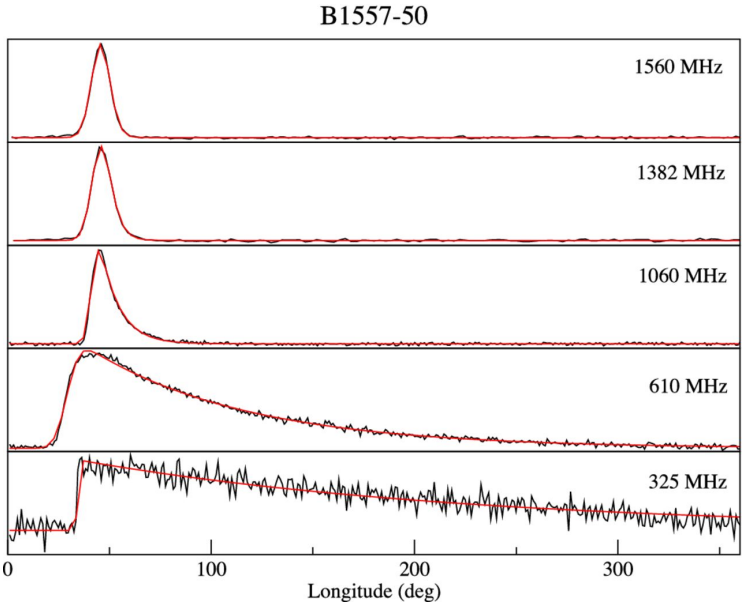


**Figure 1.6:** Pulse profiles from PSR B1557−50 at varying frequencies. The appearance of a scattering tail becomes increasingly pronounced the lower in frequency at which the observation is made (Lewandowski et al., 2013a).

and applying it to scattering, $\tau_{\rm d} = \theta_{\rm d}^2 d/c$, we can see that the relationship between delay and frequency follows a power law relation of $\tau_{\rm d} \propto \nu^{-4}$, or $-4.4$ if we are assuming the medium can be described by Kolmogorov turbulence, meaning the ISM can be described by a distribution of inhomogeneity length scales that follows a wavenumber power law of $k^{-11/3}$. Additionally, plugging these two delay expressions into Equation 1.7, we get an expression describing the intensity of the signal over time,

$$I(t) \propto e^{-t/\tau_{\rm d}}, \tag{1.8}$$

which is a one-sided exponential decay and well-characterizes the dominant feature we see in broadened pulses.

The scintillation bandwidth and timescale of a given observation can be measured by examining the frequency and time autocorrelation functions (ACFs) of the dynamic spectrum, with $\Delta\nu_{\rm d}$ defined as the half width at half maximum of central peak of the frequency ACF

and $\Delta t_{\rm d}$ defined as the half width at $e^{-1}$ of the central peak of the time ACF fit (Cordes et al., 1986). These quantities are typically measured through a Gaussian or Lorenztian fit to the ACFs. However, while the Gaussian function is good approximation of the frequency ACF, as shown above, the ISM's impulse response function (IRF) is characterized by a one-sided decaying exponential in the time domain. Given that the Fourier pair of the one-sided exponential in the frequency domain is the Lorentzian function, and that the IRF is effectively the signal codification of the scattering that is imparted onto the pulsar emission as a result of its propagation through the medium, it makes more mathematical sense to fit the corresponding frequency domain ACF using a Lorentzian (Bracewell, 1978).

The resulting scattering delays measured from these scintillation bandwidths are expected to increase with distance, as more ISM to travel through along a given LOS means more material for the pulsar signal to interact with, bringing about further path deviations and increased propagation time. The scintillation bandwidth is expected to scale with distance and observing frequency as $\Delta\nu_{\rm d} \propto \nu^{22/5} d^{-11/5}$ (Rickett, 1977). Since DM is a proxy for distance that also accounts for the actual structure of the ISM, it can be valuable to understand how scattering delays depend on DM, particularly when looking along different LOSs, as electron densities are much higher in the Galactic plane than above or below. Models like NE2001 (Cordes & Lazio, 2002) attempt to accomplish this by modeling the electron density structure in our galaxy, along with additional known features such as HII regions, to predict scintillation bandwidths and timescales using sky location, observing frequency, and DM as input parameters. We can also model the relation between delay and DM through fits over observations of many pulsars. These fits can either rely on an assumed scaling index or treat the scaling index an additional free parameter. These are well described in terms of a log parabolic function such as

$$\log \tau_{\rm d,\mu s} = a + b(\log {\rm DM}) + c(\log {\rm DM})^2 - \alpha \log \nu_{\rm GHz}, \tag{1.9}$$

used in Bhat et al. (2004), where $\alpha$ is the scaling index, or exponential functions like

$$\tau_{\mathrm{d,s}} = a\mathrm{DM}^{\gamma}(1 + b\mathrm{DM}^{\zeta})\nu^{-\alpha}, \tag{1.10}$$

used in Ramachandran et al. (1997), Krishnakumar et al. (2015), and Cordes et al. (2016), where $\alpha$ is again the scaling index and $\gamma$ is set to 2.2 under the assumption of a Kolmogorov medium.

Mathematically, during the propagation of the pulse through the ISM, the pulse undergoes a convolution with the (IRF) of the ISM. This signal is generally expected to follow the exponential decay seen in Equation 1.8, meaning that if we can deconvolve an IRF from a given pulse and fit it the IRF intensity using this exponential decay model (or just find the centroid of the IRF intensity if the signal is strong enough) we now have a direct way of measuring the scattering delay in a given signal. It should be noted that the signal-to-noise (S/N) limit on centroid approach stems from the ability to sufficiently align the recovered IRF intensity with the pulse profile intensity for the centroid calculation. The direct nature of the IRF approach makes it preferable to the dynamic spectrum approach, albeit more difficult to achieve in practice due to the high S/N generally required for effective deconvolution. In addition, the scattering in a given observation must be strong enough to resolve the deconvolved IRF.

### 1.3.3 Cyclic Spectroscopy

One promising method to perform deconvolution is a technique adopted by the pulsar community known as cyclic spectroscopy (Demorest, 2011). Widely used in the engineering community for decades (Gardner, 1987; Roberts et al., 1991; Brown & Loomis, 1993; Antoni, 2007) , this technique takes advantage of the periodic and amplitude-modulated nature of pulsar signals to extract phase information from the voltage data, and exploits the fact that the scintillation time spans many pulse periods, allowing the impulse response of the multipath propagation to be estimated. Consequentially, this allows us to obtain information necessary to reconstruct various extractable signals from our data, such as the ISM's impulse response

function, as we can recover both amplitude and phase information, which is in stark contrast to conventional spectroscopy, which can achieve only amplitude recovery.

This technique requires the raw voltage signal, necessitating baseband observations. The cyclic spectrum itself, which is the Fourier transform of the periodic spectrum (the time-averaged profile intensity as a function of profile phase and observing frequency), is given by

$$S_E(\nu, \alpha_k) = \langle E(\nu + \alpha_k/2)E^*(\nu - \alpha_k/2)\rangle = \langle H(\nu + \alpha_k/2)H^*(\nu - \alpha_k/2)\rangle S_x(\nu, \alpha_k), \quad (1.11)$$

where $E(\nu)$ is the electric field of the signal, given by $[p(\nu) * N(\nu)]H(\nu) + N_{\text{sys}}(\nu)$, $p(\nu)$ is the frequency domain of the original, pre-convolution, pulse profile $p(t)$ at time $t$ mod $P$, with $P$ being the pulse period, $N(\nu)$ is the frequency domain representation of the time domain intrinsic modulated pulsar noise, $H(\nu)$ is the transfer function of the ISM, also known as the Fourier transform of the ISM IRF, $\alpha_k = k/P$ is the cyclic frequency, and $S_x(\nu, \alpha_k)$ is the Fourier transform of the intrinsic pulse profile (Dolch et al., 2021). Quickly touching on the transfer function, dynamic spectra themselves are simply intensity representations of the transfer function at the zeroth cyclic frequency. An example cyclic spectrum can be seen in Figure 1.7, and an example deconvolved pulse with the recovered IRF is shown in Figure 1.8.

In conventional spectroscopy, frequency resolution is inherently tied to time resolution. Another benefit of cyclic spectroscopy is that, by utilizing the newly accessible harmonic information, limitations on frequency resolution can be separated from the inherent pulse phase resolution of the signal. As a result, multiple cyclic channels can be created per original pulse filterbank channel, allowing for massive improvements in the frequency resolution of observations while maintaining high pulse phase resolution. This is particularly useful in resolving finer details in intensity profiles as well as resolving previously unresolvable scintles in dynamic spectra (see Figure 1.9). This would allow for valuable scintillation science to be performed on many pulsars where current traditional filterbank resolution is limited such that their scintillation bandwidths at various frequencies are unresolvable.

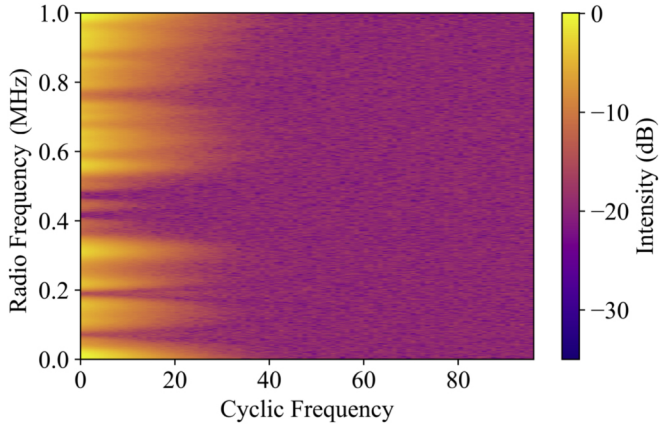


**Figure 1.7:** A simulated cyclic spectrum from Dolch et al. (2021). The cyclic frequency out to which there is power in the signal depends on a number of factors including pulsar S/N and duty cycle.

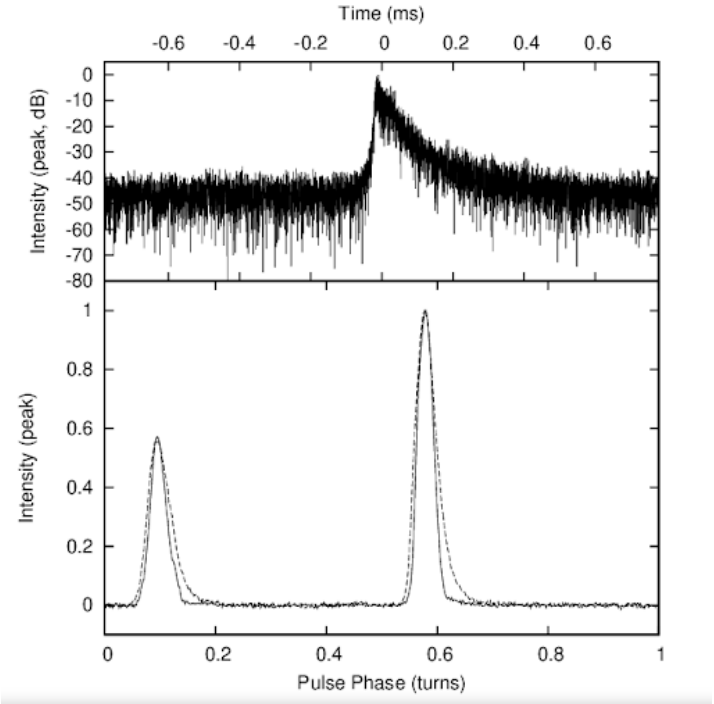


**Figure 1.8:** (Top) An example recovered impulse response function from an observation of PSR B1937+21. (Bottom) The intrinsic profile (solid line) and pulse profile prior to deconvolution of the IRF (dashed line) (Demorest, 2011).

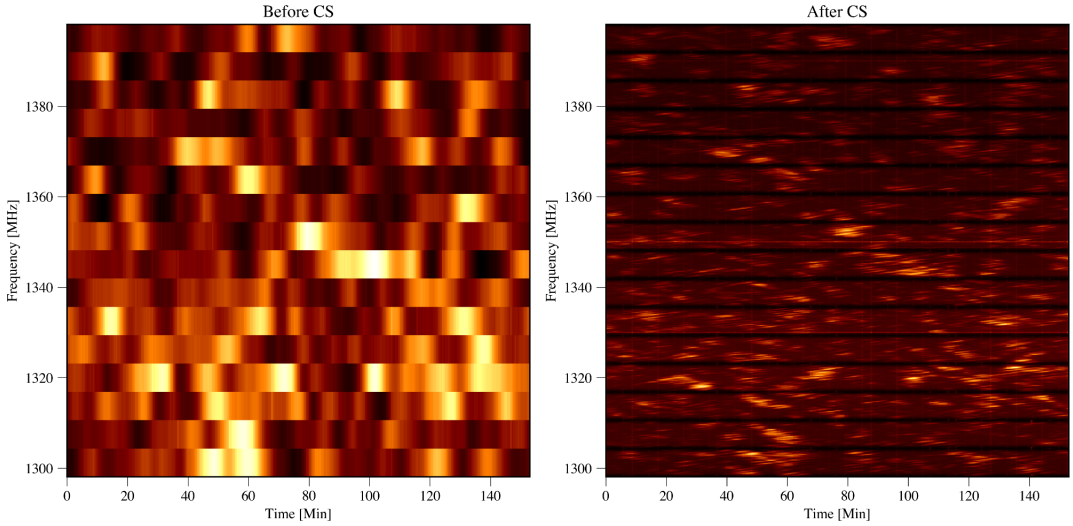


**Figure 1.9:** A dynamic spectrum created from archival data from 2012 of PSR B1937+21 processed using traditional filterbanks (left) and with 1024 cyclic channels per filterbank (right). There is a striking improvement in frequency resolution in the CS-processed dynamic spectrum, which is now useable for various scintillation analyses (Chapter 5).

### 1.3.4 Scintillation Arcs

When scintles in a pulsar dynamic spectrum are fully resolved in observing frequency and time, interesting parabolic structures can arise in the pulsar's two-dimensional secondary, or power, spectrum, which is the two-dimensional Fourier transform of the dynamic spectrum. These parabolas, known as scintillation arcs (see Figure 1.10), can be a powerful tool for understanding localized scattering along a LOS. First described in Stinebring et al. (2001a), this phenomenon is thought to be a consequence of scattering occurring at a thin screen at a distance $d_s$ from the pulsar, which itself is located at a distance $d$ from Earth. For interference between two rays at angles $\boldsymbol{\theta}_1$ and $\boldsymbol{\theta}_2$, at an observing wavelength $\lambda$, the conjugate variables to time and frequency, $f_t$ (also written as $f_D$) and $f_\nu$ (also written as $\tau$), known as the fringe frequency or differential doppler shift and differential delay, respectively (Cordes et al., 2006a), can be written as

$$f_t = \frac{d}{\lambda d_s}(\boldsymbol{\theta}_2 - \boldsymbol{\theta}_1)\boldsymbol{V}_{\mathrm{eff},\perp} \tag{1.12}$$

and

$$f_\nu = \frac{d}{2cd_s}(d - d_s)(\boldsymbol{\theta}_2^2 - \boldsymbol{\theta}_1^2), \tag{1.13}$$

where the effective velocity of the pulsar perpendicular to the LOS,

$$\boldsymbol{V}_{\mathrm{eff},\perp} = \frac{1}{s}\boldsymbol{V}_{\mathrm{screen},\perp} - \frac{1-s}{s}\boldsymbol{V}_{\mathrm{pulsar},\perp} - \boldsymbol{V}_{\mathrm{Earth},\perp}. \tag{1.14}$$

Here the fractional screen distance, $s$, is given by $s = 1 - d_s/d$, $\boldsymbol{V}_{\mathrm{pulsar},\perp}$ is the perpendicular velocity of the pulsar, $\boldsymbol{V}_{\mathrm{screen},\perp}$ is the perpendicular velocity of the screen, and $\boldsymbol{V}_{\mathrm{Earth},\perp}$ is the perpendicular velocity of Earth (Stinebring et al., 2001a; Cordes et al., 2006a; McKee et al., 2022; Reardon et al., 2020a).

Setting one angle as a point source at the origin, therefore making $\boldsymbol{\theta}_1 = 0$, orienting the $x$-axis perpendicular to the pulsar effective velocity, only considering interference in this

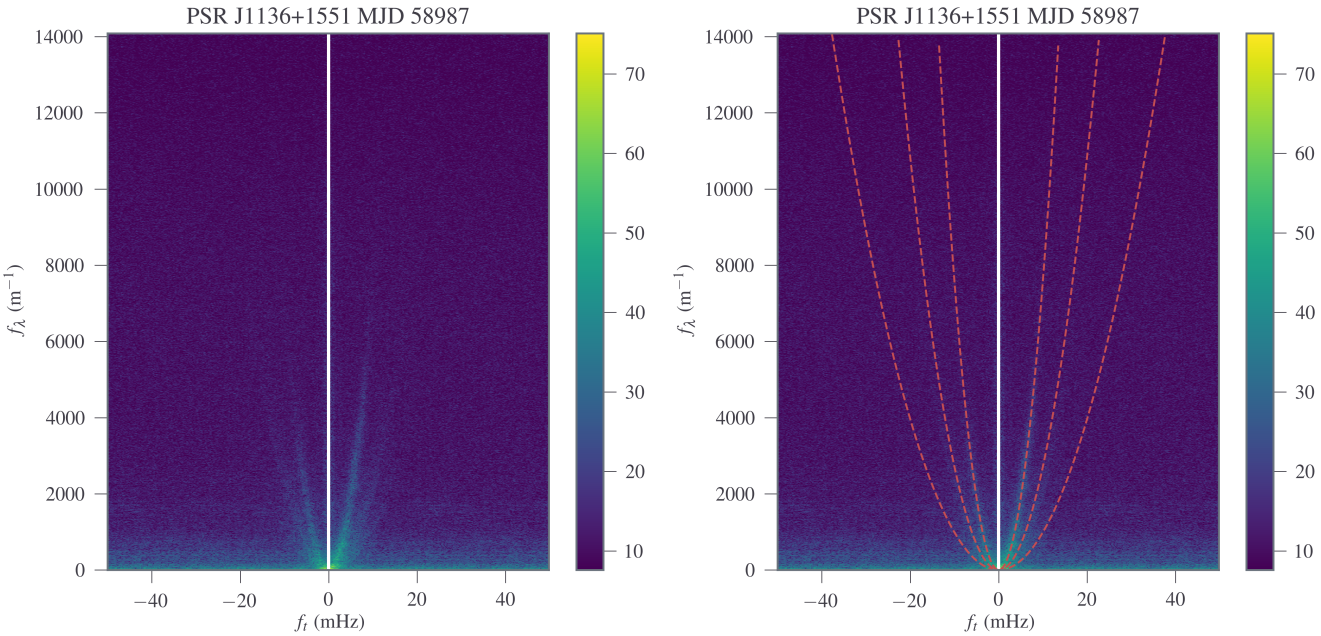


**(a)** Scintillation arcs without overlaid fits

**(b)** Scintillation arcs with overlaid fits

**Figure 1.10:** Example secondary spectrum from Chapter 3 showing an observation in which multiple scintillation arcs were visible, indicating multiple regions of pronounced scattering along the LOS to this pulsar.

direction (Hill et al., 2003a), and setting the effective distance $d_{\rm eff}$ as $d(1-s)/s$, the fringe frequency and differential delay can be related via

$$f_\nu = \frac{\lambda^2 d_{\rm eff}}{2c\boldsymbol{V}_{\rm eff,\perp}} f_t^2, \tag{1.15}$$

with the arc curvature

$$\eta = \frac{\lambda^2 d_{\rm eff}}{2c\boldsymbol{V}_{\rm eff,\perp}}. \tag{1.16}$$

By examining Equation 1.16, we can see that this model predicts that arc curvature should evolve with observing frequency as $\nu^{-2}$, following the same frequency dependence as the angular deflection of the rays, and that, given knowledge of the pulsar's effective velocity, one can use arc curvature to determine the location of the scattering screen along that LOS.

In practice, it can be difficult to determine $\boldsymbol{V}_{\mathrm{eff},\perp}$ without making many observations over a long period of time, as there is a covariance between $s$ and $\boldsymbol{V}_{\mathrm{screen},\perp}$. That being said, in many cases it is appropriate to make the assumption that the pulsar velocity dominates, and the effective velocity can be approximated at the transverse velocity calculated from the pulsar's proper motion.

Some additional information can be gained by analyzing the structure of the arcs. An asymmetric arc, where the arc appears tilted or when one arm appears brighter, is a strong indication of refraction, and high-cadence observing campaigns looking for when the dominant arm switches can help place constraints on a pulsar's refractive timescale. Additionally, sometimes inverted "arclets", which, when fully resolved, can be seen to be inverted versions of the arc (and identical in curvature) of which they are a part, can be seen along the arms of a scintillation arc, indicating small-scale – typically AU-size – inhomogeneities in a given scattering screen (see Figure 1.11).

Arc curvatures can be determined using a multitude of approaches, ranging from simply fitting by eye if the arcs are sufficiently resolved (Hill et al., 2003b), fitting the channels containing the highest power at each delay along each half of the fringe frequency axis (Stinebring et al., 2022), or the more in-depth Hough transform approach (Bhat et al., 2016). In this technique, a range of curvatures is sampled over the secondary spectrum, with the curvature resulting in the greatest summed power along the resulting fit being the measured curvature for that observation. The mean power $P$ over a given curvature $\eta$ is given by

$$P(\eta) = \frac{1}{N}\sum_{i=1}^{N} S_2(\eta f_{t,i}^2, f_{t,i}), \tag{1.17}$$

where $S_2$ is the secondary spectrum and the summation uses the $N$ points along a given curvature that ignore low frequency noise and extend only as far on the delay axis as there exists measureable power in a given arc.

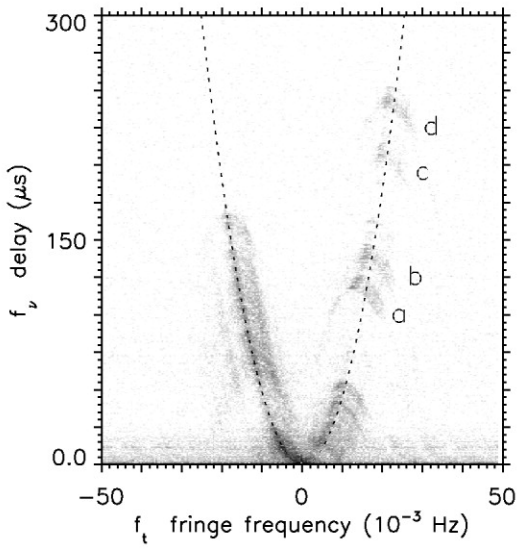


**Figure 1.11:** An example scintillation arc from Hill et al. (2005). Inverted arclets can be seen throughout the structure of the arcs, with isolated arclets labeled alphabetically with increasing position on the differential delay axis.

## 1.4 Thesis Overview

This thesis serves to highlight some valuable studies related to understanding the structure and behavior of the ionized interstellar medium via the interstellar scattering of pulsar emission. In Chapter 2 we detail the scattering delays present in the 12.5 year data release of the NANOGrav scientific collaboration. We find many pulsars exhibit typical scattering delays of tens to hundreds of nanoseconds in a given epoch which are not accounted for in pulsar timing models being used. We also perform many analyses using this scattering information to characterize the structure and behavior of the ISM along 28 lines of sight in the galaxy. In Chapter 3 we use simultaneous dual-frequency observations to analyze scintillation, with a focus on scintillation arcs, in six bright canonical pulsars to perform robust studies of the ISM. We measure important scaling relations with high precision, examine scintillation variations over short timescales, and demonstrate biases in some common scintillation arc measurement techniques.

In Chapter 4 we examine the effectiveness of cyclic spectroscopy at recovering scattering delays by simulating scattered pulses and attempting to recover the corresponding delays using CS and ACF approaches. We find that the CS approach is both more precise and accurate for individual epochs assuming sufficient S/N. In Chapter 5 we apply CS to observations of the millisecond pulsar B1937+21. We demonstrate the power of this processing technique to significantly improve the frequency resolution of observations, allowing for detailed scintillation studies that would not be possible under conventional pulsar timing array observing setups. Finally, in Chapter 6, we summarize the conclusions to this thesis and highlight the capabilities of the ongoing efforts at the Green Bank Observatory to complete a near real-time cyclic spectroscopy pipeline.

# Chapter 2. The NANOGrav 12.5-Year Data Set: Monitoring Interstellar Scattering Delays

## 2.1 Introduction

The North American Nanohertz Observatory for Gravitational Waves (NANOGrav; McLaughlin, 2013) aims to use a pulsar timing array (PTA) to detect nanohertz frequency gravitational waves. The 12.5-year data set (Alam et al., 2020a) presents observations of 47 millisecond pulsars (MSPs) with up to sub-$\mu$s precision and finds a strong, common red-noise process consistent with a gravitational-wave background but lacks the quadrupolar correlations necessary to claim a detection (Arzoumanian et al., 2020a). Pulsar timing precision is largely a result of robust timing models for each MSP, accounting for many phenomena that might affect a pulsar time of arrival (TOA) and potentially mask a gravitational wave signal in our data.

One of the most significant sources of TOA residual uncertainty for PTAs comes from the interaction between a pulsar's radio emission and free electrons in the interstellar medium (ISM). The most significant of these ISM effects is dispersion, in which a frequency-dependent time delay arises from the radio emission propagating through free electrons in the ISM. The delay at a given observing epoch can be related to the product of the integrated column density of free electrons along the line of sight (LOS), known as the dispersion measure (DM), and the inverse square of the observation frequency, $\nu$. Since the Earth, the solar system, the ISM, and the pulsars all have motions that vary the LOS from epoch to epoch, DM is time-dependent. The delay can be corrected by observing a pulsar at multiple frequencies at each observing

Published as J. E. Turner et al. 2021, ApJ, 917, 10

epoch (Roberts et al., 2005; Demorest et al., 2012; Arzoumanian et al., 2015b; Jones et al., 2017; Keith et al., 2013).

Interstellar scattering also contributes epoch-dependent delays. The phenomenon is the result of a pulsar's radio emission propagating through a non-uniform distribution of free electrons. These delays also vary with time. However, the nature of the propagation for dispersion and scattering results in different frequency dependencies for each phenomenon. As mentioned above, the dispersion delay scales as $\Delta t_{\rm DM} \propto \nu^{-2}$, and, if we assume fluctuations in the ISM can be modeled by a Kolmogorov-like spectrum, it can be shown that time delays from scattering go as $\tau_{\rm d} \propto \nu^{-4.4}$ if inner-scale effects are ignored and if the scattering properties of the medium are the same everywhere (or, for a screen, identical across the screen), and if refraction does not modify the scattering (Cordes & Rickett, 1998).

We see the effects of interstellar scattering in the broadening of pulse profiles and the delaying of pulse arrival times. Scattering also results in interstellar scintillation, which arises from two interrelated phenomenon: diffractive interstellar scintillation (DISS) and refractive interstellar scintillation (RISS) (Rickett, 1990). With NANOGrav's observing cadence, DISS is the most observable over a single epoch, primarily because the resulting variability is resolvable over typical observation lengths and bandwidths (Arzoumanian et al., 2018). More specifically, for gigahertz frequencies and pulsars at DMs $\simeq 50$ pc cm$^{-3}$ the characteristic timescale from DISS is typically on the order of minutes and the characteristic bandwidth from the accompanying pulse broadening is on the order of megahertz (Cordes & Rickett, 1998), although we observe large variations in scintillation parameters for a given DM.

Levin et al. (2016) examined effects from DISS on pulsars in the NANOGrav 9-year data set (Arzoumanian et al., 2015b) and found that, generally, NANOGrav pulsars exhibit scattering delays on the order of 1–100 ns at 1500 MHz. However, even if delays are small compared to TOA errors, if they are correlated over time they could contribute to noise in the data set. Quite a few works, including Hemberger & Stinebring (2008a), Coles et al. (2015), Lentati et al. (2017), McKee et al. (2018), and Main et al. (2020) have found at least modest evidence that delays are correlated over time. Additionally, as NANOGrav's timing precision

reaches the sub-100 ns regime for more pulsars, delays from scattering become significant enough to warrant further investigation and possibly mitigation in many pulsars. Since our current timing pipeline does not account for scattering variability, scattering delays may be partially absorbed in DM fits (Arzoumanian et al., 2015b). Because the frequency scaling of these two noise sources is different, this is an additional source of noise in our timing residuals. Levin et al. (2016) also showed that many pulsars do not follow $\nu^{-4.4}$ frequency scaling, instead exhibiting shallower power-law behaviors, further motivating the need to separate the effects of dispersion and scattering.

In this paper we aim to expand upon the work done in Levin et al. (2016) by examining the effects of scattering on TOAs for pulsars in the NANOGrav 12.5-year data set and looking for deviations from the $\nu^{-4.4}$ frequency scaling. We also explore how scattering can give us insight into other information on MSPs and the ISM, including pulsar transverse velocities and the large-scale structure of the ISM in the Milky Way.

## 2.2 Data

We used observations from the NANOGrav 12.5-year data set (Alam et al., 2020a)[1]. The data were taken and coherently dedispersed with the FPGA-based spectrometers GUPPI (Green Bank Ultimate Pulsar Processing Instrument) and PUPPI (Puerto Rico Ultimate Pulsar Processing Instrument) at the Green Bank Telescope and the Arecibo Observatory, respectively (DuPlain et al., 2008; Ford et al., 2010). This process was done on 47 pulsars, 11 of which are new to the 12.5-year data set and consequently were not included in the analysis done by Levin et al. (2016).

We reused the results from the Levin et al. (2016) analysis and augmented them by analyzing ∼3.6 years of new data not included in the nine year data set from both telescopes, with the MJD range for most pulsars spanning approximately 56603–57933 (2013 November–2017 June). Observations at Arecibo were centered near 1380 MHz using bandwidths of 800

[1] `http://data.nanograv.org`

MHz with 1 second subintegrations, while observations at Green Bank were centered near 820 and 1500 MHz using 200 and 800 MHz bandwidths, respectively, with 10 second subintegrations. Observations at both telescopes were divided into 1.56 MHz frequency channels, and were ∼30 minutes in length. While the NANOGrav 12.5-year data set also includes 327 MHz, 430 MHz, and 2.1 GHz data from Arecibo, the scintles are generally either too narrow to be frequency resolved at our current resolution in the case of 327 and 430 MHz or either too wide or with an insufficient number of scintles to be properly analyzed given our current observation bandwidth in the case of 2.1 GHz.

All observations began with a polarization calibration scan with a 25 Hz noise diode injection for both polarizations. A flux calibrator, QSO J1445+099, is also observed once per epoch per frequency. All of the analyses done in this paper used total intensity profiles, which were made by summing the polarizations of the calibrated data.

As mentioned in Alam et al. (2020a), small timing mismatches in both of these backends led to frequency-reversed "ghost images" of pulses appearing in the data. These can result in large offsets in residuals if uncorrected. This has been accounted for in the 12.5-year data set, and anything left from the subtraction will negligibly affect the information contained in our dynamic spectra.

## 2.3 Analysis

### 2.3.1 Scintillation Parameters

Following a method similar to Cordes (1986a) and identical to that of Levin et al. (2016), we created 2D dynamic spectra from each 820 and 1500 MHz observation of all pulsars in our analysis. To create a dynamic spectrum, we calculate the intensity, $S$, of the pulsar's signal at any given observing frequency, $\nu$, and time, $t$, in that observation by the relation

$$S(\nu, t) = \frac{P_{\rm on}(\nu, t) - P_{\rm off}(\nu, t)}{P_{\rm bandpass}(\nu, t)}, \tag{2.1}$$

where $P_{\rm bandpass}$ is the total power of the observation as a function of observing frequency and time, and $P_{\rm on}$ and $P_{\rm off}$ are the power in all on- and off-pulse components of the pulse profile, respectively. After smoothing from 2048 pulse profile bins to 64 bins, we define the on-pulse component as the bins in the summed profile that have an intensity $> 5\%$ of the maximum within a continuous window.

These observations were calibrated and excised of radio-frequency interference (RFI) via the median-smoothed difference channel-zapping algorithm in PSRCHIVE's paz function (Hotan et al., 2004) and converted into 2D dynamic spectra, such as those seen at the top of Figures 2.1 and 2.2. As shown in Figure 2.1, to determine the scintle sizes at each epoch, we first computed a 2D autocorrelation function (ACF) and summed separately over time and frequency to create a 1D time ACF and a 1D frequency ACF taken at zero time lag and zero frequency lag, respectively. We then fit Gaussian functions to the frequency and time axes at lag 0 of the ACF to obtain estimates for the scintillation bandwidth and timescale, respectively (see Figure 2.2).

Scattering effects can be estimated based on the size of scintles (maxima) in both time and frequency in a pulsar's dynamic spectra. Here we focus on the scintillation timescale, $\Delta t_{\rm d}$, defined as the half-width at $e^{-1}$ of the values along the time axis at ACF lag 0 of the dynamic spectrum's 2D ACF, and the scintillation bandwidth, $\Delta\nu_{\rm d}$, defined as the half-width at half-maximum of the values along the frequency ACF at lag 0 of the 2D ACF. The scattering delay, $\tau_{\rm d}$, can subsequently be obtained from the scintillation bandwidth via the relation

$$2\pi\Delta\nu_{\rm d}\tau_{\rm d} = C_1, \tag{2.2}$$

where $C_1$ is a dimensionless quantity in the range $0.6 - 1.5$ conditional on the geometry and spectrum of the electron density fluctuations of the medium (Cordes & Rickett, 1998). In this analysis we assume $C_1 = 1$, as in Levin et al. (2016). We found the results of the 1D and 2D Gaussian fits to the 1D and 2D ACFs, respectively, to be in agreement, and opted to use the 1D ACFs for our analysis since most of the pulsars have scintillation timescales longer than our observation times. If our observations were long enough to resolve the scintles in both time

and frequency, as in Shapiro-Albert et al. (2020), we would have used the 2D ACFs since there would have been a sufficient number of scintles within the observing time.

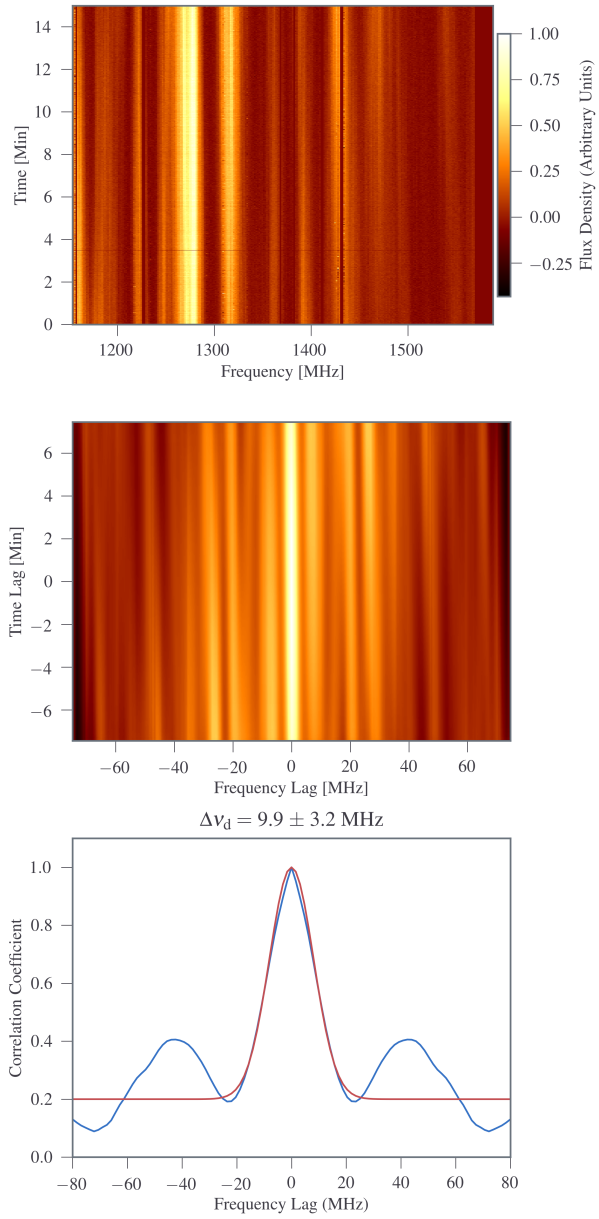


**Figure 2.1:** Example of stretched dynamic spectra (top), the corresponding 2D ACF (middle), and the resulting values along the time axis of the ACF at lag 0 (bottom, with the 1D ACF in blue and Gaussian fit in red) from a PSR B1855+09 observation with the Arecibo telescope. The $1\sigma$ error shown above includes the finite scintle error. Note in this case that the scintles are not fully resolved in time, as is typical in our data because most of our observations are shorter than the scintillation timescales of the pulsars under observation.

**Table 2.1:** Measured Scintillation Parameters

| | This work | | | | | | | | | | | | Levin et al. (2016) | |
|---|---|---|---|---|---|---|---|---|---|---|---|---|---|---|
| Pulsar | $\overline{\Delta\nu}_{\rm d}^{1500}$ (MHz) | $\overline{\tau}_{\rm d}^{1500}$ (ns) | $N_{\rm scint}^{\rm med;1500}$ | $N_{\nu}^{1500}$ | $\overline{\Delta t}_{\rm d}^{1500}$ (min) | $N_{\rm t}^{1500}$ | $\overline{\Delta\nu}_{\rm d}^{820}$ (MHz) | $\overline{\tau}_{\rm d}^{820}$ (ns) | $N_{\rm scint}^{\rm med;820}$ | $N_{\nu}^{820}$ | $\overline{\Delta t}_{\rm d}^{820}$ (min) | $N_{\rm t}^{820}$ | $\overline{\Delta\nu}_{\rm d}^{1500}$ (MHz) | $\overline{\tau}_{\rm d}^{1500}$ (ns) |
| J0340+4130 | <3.3 ± 1.3 | >33 ± 17 | 32 | 10 | — | — | — | — | — | — | — | — | 9 ± 3 | 15 ± 6 |
| J0613–0200 | 4 ± 3 | 16 ± 11 | 21 | 40 | 10 ± 4 | 4 | <1.6 ± 0.2 | >78 ± 17 | 25 | 19 | 6 ± 3 | 7 | 11 ± 4 | 12 ± 4 |
| J0636+5128 | 7 ± 4 | 12 ± 9 | 17 | 24 | 9 ± 3 | 13 | <1.5 ± 1.0 | >31 ± 37 | 23 | 26 | 8 ± 3 | 17 | — | — |
| J0740+6620 | 81 ± 30 | 1.5 ± 0.5 | 2 | 4 | — | — | 18 ± 9 | 5 ± 3 | 3 | 16 | — | — | — | — |
| J0931−1902 | 20 ± 4 | 7 ± 2 | 9 | 4 | > 30 | — | — | — | — | — | — | — | 50 | 3 |
| J1012+5307 | 40 ± 18 | 4 ± 2 | 6 | 1 | — | — | — | — | — | — | — | — | 66 ± 6 | 2.5 ± 0.1 |
| J1024−0719 | 36 ± 3 | 4.4 ± 0.3 | 5 | 3 | > 30 | — | 10 ± 3 | 11 ± 4 | 4 | 6 | 17 ± 4 | 1 | 47 ± 18 | 3 ± 1 |
| J1125+7819 | 50 ± 20 | 1.9 ± 0.9 | 3 | 25 | — | — | 7 ± 3 | 17 ± 8 | 6 | 37 | 12 ± 4 | 23 | — | — |
| J1455−3330 | 43 ± 12 | 3.2 ± 0.9 | 5 | 5 | — | — | 5 ± 1 | 27 ± 7 | 8 | 12 | — | — | 70 ± 18 | 4 ± 1 |
| J1614−2230 | 6 ± 3 | 16 ± 6 | 25 | 16 | 9 ± 3 | 1 | <2.4 ± 0.6 | >33 ± 14 | 17 | 3 | 5 ± 1 | 1 | 9 ± 3 | 16 ± 5 |
| J1640+2224 | 50 ± 26 | 1.8 ± 0.9 | 4 | 17 | > 30 | — | — | — | — | — | — | — | 56 ± 15 | 3 ± 1 |
| J1713+0747 | 23 ± 15 | 3 ± 2 | 6 | 72 | > 30 | — | — | — | — | — | — | — | 21 ± 9 | 7 ± 2 |
| J1738+0333 | 19 ± 8 | 6 ± 3 | 9 | 18 | > 30 | — | — | — | — | — | — | — | 17 ± 8 | 9 ± 2 |
| J1744−1134 | 33 ± 13 | 3.3 ± 1.6 | 5 | 18 | ¿30 | — | 10 ± 3 | 12 ± 4 | 5 | 21 | — | — | 42 ± 9 | 4 ± 1 |
| J1853+1303 | 11 ± 6 | 8 ± 4 | 14 | 6 | > 30 | — | — | — | — | — | — | — | 13 ± 5 | 12 ± 5 |
| B1855+09 | 10 ± 5 | 8 ± 4 | 11 | 25 | > 30 | — | 9 ± 3 | 18 ± 6 | 5 | 1 | — | — | 5 ± 2 | 21 ± 10 |
| J1909−3744 | 28 ± 13 | 4 ± 2 | 6 | 89 | — | — | <4 ± 1 | >21 ± 12 | 10 | 18 | 6 ± 2 | 5 | 39 ± 15 | 5 ± 2 |
| J1910+1256 | 2.3 ± 0.8 | 47 ± 23 | 71 | 17 | > 30 | — | <3.4 ± 2.6 | >90 ± 44 | 26 | 3 | > 30 | — | 2.3 ± 0.9 | 58 ± 17 |
| J1918−0642 | 9 ± 3 | 13 ± 5 | 16 | 28 | > 30 | — | — | — | — | — | — | — | 15 ± 5 | 10 ± 3 |
| J1923+2515 | 18 ± 4 | 2.4 ± 1.6 | 5 | 8 | — | — | — | — | — | — | — | — | 22 ± 10 | 6 ± 1 |
| B1937+21 | <1.5 ± 0.8 | > 76 ± 43 | 30 | 43 | 9 ± 3 | 23 | — | — | — | — | — | — | 2.8 ± 1.3 | 44 ± 21 |
| J1944+0907 | 8 ± 6 | 7 ± 6 | 17 | 28 | — | — | 3 ± 3 | 5 ± 7 | 14 | 3 | — | — | 11 ± 5 | 10 ± 6 |
| J2010−1323 | 8 ± 3 | 13 ± 6 | 18 | 29 | 7 ± 6 | 2 | — | — | — | — | — | — | 7 ± 2 | 19 ± 6 |

| | | | | | | | | | | | | | | |
|---|---|---|---|---|---|---|---|---|---|---|---|---|---|---|
| J2043+1711 | 56 ± 27 | 1.8 ± 0.9 | 4 | 2 | > 30 | — | — | — | — | — | — | — | 86 | 2 |
| J2145−0750 | 43 ± 11 | 3 ± 1 | 4 | 7 | > 30 | — | 7 ± 4 | 9 ± 5 | 5 | 19 | > 30 | — | 48 ± 13 | 2.8 ± 0.7 |
| J2229+2643 | 46 ± 15 | 2.9 ± 0.8 | 4 | 6 | — | — | — | — | — | — | — | — | — | — |
| J2302+4442 | 8 ± 7 | 16 ± 8 | 20 | 15 | — | — | < 1.5 ± 0.2 | > 37 ± 15 | 26 | 20 | — | — | 10 ± 2 | 14 ± 3 |
| J2317+1439 | 46 ± 14 | 2.8 ± 0.8 | 5 | 13 | > 30 | — | 12 ± 6 | 13 ± 5 | 5 | 1 | — | — | 42 ± 12 | 3 ± 1 |

**Table 2.1:** All parameters with bars ($\overline{\tau}_{\rm d}$, $\overline{\Delta\nu}_{\rm d}$, etc.) represent ensemble weighted averages of the individual measurements, with $1\sigma$ errors shown. $N^{\rm med}_{\rm scint;}$ represents the median number of scintles and $N_{\rm t}$ and $N_\nu$ indicate the number of estimates made for that quantity. $\tau_{\rm d}$ values represent the scattering delays, while $\Delta\nu_{\rm d}$ values represent scintillation bandwidths. All measurements and errors have been rounded to the last significant digit shown. Values with only one measurement use their measured uncertainties as opposed to weighted errors. Due to our short observation lengths, it is likely that all of our $\overline{\Delta t_{\rm d}}$ values are biased lower than their true averages.

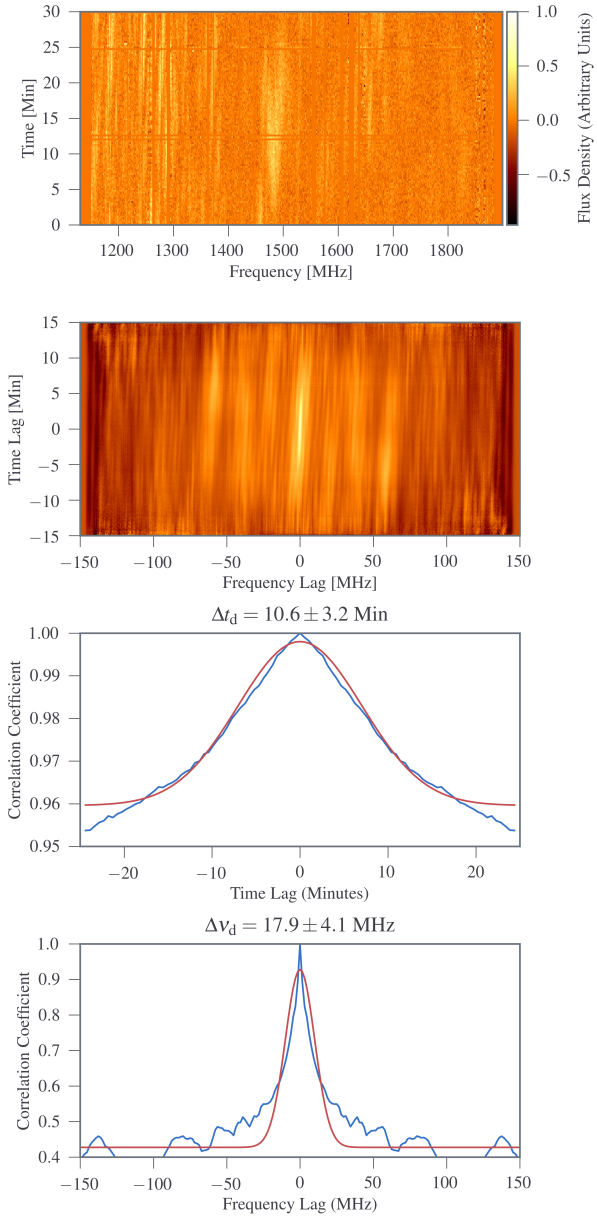


**Figure 2.2:** As in Figure 2.1, but for an observation of PSR J0636+5128 with the Green Bank telescope. For this pulsar, we are able to measure a scintillation timescale, though it is likely an underestimate due to the short durations of our observations.

**Table 2.2:** NE2001 Electron Density Model Predicted Scintillation Parameters

| Pulsar | Period | DM | $\tau_{d;1500}^{NE2001}$ | $\Delta\nu_{d;1500}^{NE2001}$ | $\Delta t_{d;1500}^{NE2001}$ | $\tau_{d;820}^{NE2001}$ | $\Delta\nu_{d;820}^{NE2001}$ | $\Delta t_{d;820}^{NE2001}$ |
|---|---|---|---|---|---|---|---|---|
| | (ms) | (pc cm$^{-3}$) | (ns) | (MHz) | (min) | (ns) | (MHz) | (min) |
| J0023+0923 | 3.05 | 14.3 | 2.5 | 42.5 | 17.4 | 40 | 9.1 | 13.2 |
| J0030+0451 | 4.87 | 4.3 | 0.06 | 1900 | 710 | 0.8 | 405 | 540 |
| J0340+4130 | 3.29 | 49.6 | 50 | 2.1 | 17.1 | 700 | 0.5 | 12.9 |
| J0613−0200 | 3.06 | 38.8 | 20 | 6.4 | 16.4 | 230 | 1.4 | 12.5 |
| J0636+5128 | 2.87 | 11.1 | 1.9 | 55.1 | 95 | 30 | 11.8 | 72 |
| J0645+5158 | 8.85 | 18.2 | 6.1 | 17.2 | 20.3 | 90 | 3.7 | 15.4 |
| J0740+6620 | 2.89 | 15.0 | 3.2 | 33.0 | 12.6 | 50 | 7.1 | 9.5 |
| J0931−1902 | 4.64 | 41.5 | 20 | 4.3 | 30.5 | 350 | 0.9 | 23.2 |
| J1012+5307 | 5.26 | 9.0 | 1.2 | 88 | 16.6 | 20 | 18.8 | 12.6 |
| J1024−0719 | 5.16 | 6.5 | 0.2 | 610 | 16.8 | 2.4 | 130 | 12.7 |
| J1125+7819 | 4.2 | 12.0 | 1.5 | 70.1 | 21.9 | 20 | 15 | 16.7 |
| J1453+1902 | 5.79 | 14.1 | 3.1 | 34.1 | 26.4 | 40 | 7.3 | 20.1 |
| J1455−3330 | 7.99 | 13.6 | 1.0 | 110 | 103 | 10 | 23.3 | 78 |
| J1600−3053 | 3.60 | 52.3 | 90 | 1.1 | 5.1 | 1,300 | 0.24 | 3.9 |
| J1614−2230 | 3.15 | 34.5 | 30 | 3.6 | 5.4 | 420 | 0.8 | 4.1 |
| J1640+2224 | 3.16 | 18.4 | 5.8 | 18.1 | 15.3 | 80 | 3.9 | 11.7 |
| J1643−1224 | 4.62 | 62.3 | 90 | 1.2 | 5.9 | 1,300 | 0.25 | 4.4 |
| J1713+0747 | 4.57 | 16.0 | 4.1 | 25.6 | 37.7 | 60 | 5.5 | 28.6 |
| J1738+0333 | 5.85 | 33.8 | 20 | 5.00 | 5.5 | 300 | 1.1 | 4.1 |
| J1741+1351 | 3.75 | 24.2 | 0.7 | 160 | 48.8 | 9.3 | 35 | 37.1 |
| J1744−1134 | 4.08 | 3.1 | 0.02 | 5,700 | 335 | 0.3 | 1,200 | 253 |
| J1747−4036 | 1.65 | 153.0 | 2,400 | 0.04 | 2.4 | 30,000 | 0.01 | 1.8 |
| J1832−0836 | 2.72 | 28.2 | 20 | 5.9 | 2.9 | 250 | 1.3 | 2.2 |
| J1853+1303 | 4.09 | 30.6 | 6.2 | 52.2 | 16.3 | 90 | 3.6 | 39.7 |
| B1855+09 | 5.36 | 13.3 | 2.2 | 4.9 | 53.9 | 30 | 10.4 | 41.1 |
| J1903+0327 | 2.15 | 297.5 | 240,000 | 0.0004 | 0.5 | 3,400,000 | 0.00009 | 0.5 |

**Table 2.2:** NE2001 Electron Density Model Predicted Scintillation Parameters

| Pulsar | Period | DM | $\tau_{\mathrm{d;1500}}^{\mathrm{NE2001}}$ | $\Delta\nu_{\mathrm{d;1500}}^{\mathrm{NE2001}}$ | $\Delta\mathrm{t}_{\mathrm{d;1500}}^{\mathrm{NE2001}}$ | $\tau_{\mathrm{d;820}}^{\mathrm{NE2001}}$ | $\Delta\nu_{\mathrm{d;820}}^{\mathrm{NE2001}}$ | $\Delta\mathrm{t}_{\mathrm{d;820}}^{\mathrm{NE2001}}$ |
|---|---|---|---|---|---|---|---|---|
| | (ms) | (pc cm$^{-3}$) | (ns) | (MHz) | (min) | (ns) | (MHz) | (min) |
| J1909−3744 | 2.95 | 10.4 | 1.5 | 68 | 7.9 | 20 | 14.6 | 6.0 |
| J1910+1256 | 4.98 | 38.1 | 8.4 | 12.5 | 19.0 | 120 | 2.7 | 14.5 |
| J1911+1347 | 4.63 | 31.0 | 5.0 | 20.8 | 21.7 | 70 | 4.5 | 16.6 |
| J1918−0642 | 7.65 | 26.6 | 10 | 10.0 | 21.3 | 150 | 2.1 | 16.1 |
| J1923+2515 | 3.88 | 18.9 | 1.7 | 61 | 22.7 | 20 | 13 | 17.2 |
| B1937+21 | 1.56 | 71.0 | 130 | 0.8 | 62.0 | 190 | 0.2 | 46.1 |
| J1944+0907 | 5.19 | 24.3 | 2.9 | 36 | 9.8 | 40 | 7.7 | 7.5 |
| J1946+3417 | 3.17 | 110.2 | 210 | 0.5 | 2.0 | 3,100 | 0.1 | 1.5 |
| B1953+29 | 6.13 | 104.5 | 240 | 0.43 | 4.3 | 3,500 | 0.09 | 3.3 |
| J2010−1323 | 5.22 | 22.2 | 6.7 | 15.7 | 16.7 | 100 | 3.4 | 12.8 |
| J2017+0603 | 2.90 | 23.9 | 3.8 | 27.9 | 52.7 | 50 | 6.0 | 40.1 |
| J2033+1734 | 5.95 | 25.1 | 3.0 | 35.4 | 53.7 | 40 | 7.6 | 40.9 |
| J2043+1711 | 2.38 | 20.7 | 2.0 | 51 | 30.8 | 30 | 11 | 23.8 |
| J2145−0750 | 16.05 | 9.0 | 0.5 | 200 | 60.5 | 7.5 | 42.3 | 45.9 |
| J2214+3000 | 3.12 | 22.5 | 3.1 | 33.8 | 41.2 | 40 | 7.2 | 31.2 |
| J2229+2643 | 2.98 | 22.7 | 4.2 | 25.2 | 18.8 | 60 | 5.4 | 14.3 |
| J2234+0611 | 3.58 | 10.8 | 0.8 | 136 | 14.9 | 10 | 29.1 | 11.3 |
| J2234+0944 | 3.63 | 17.8 | 3.3 | 31.5 | 9.9 | 0.5 | 6.7 | 7.5 |
| J2302+4442 | 5.19 | 13.8 | 0.9 | 120 | 103 | 10 | 26.4 | 79 |
| J2317+1439 | 3.45 | 21.9 | 1.9 | 54 | 57.4 | 30 | 11.6 | 43.5 |
| J2322+2057 | 4.81 | 13.4 | 1.0 | 104 | 25.3 | 10 | 22.3 | 19.2 |

**Table 2.2:** Predictions of scattering delays, scintillation bandwidths, and scintillation timescales made by the NE2001 electron density model (Cordes & Lazio, 2002). We calculated $\Delta t_{\mathrm{d}}$ values using transverse velocities derived from proper motions rather than the 100 km s$^{-1}$ transverse velocity that NE2001 assumes. DM distances were used for calculating transverse velocities if current parallax measurements were negative or if errors on parallax measurements were larger than around 25%.

Uncertainties in our scattering delay measurements are an addition in quadrature of the finite scintle error, which can be approximated as

$$\begin{aligned} \epsilon &\approx \tau_{\rm d} N_{\rm scint}^{-1/2} \\ &\approx \tau_{\rm d}[(1+\eta_{\rm t} T/\Delta t_{\rm d})(1+\eta_\nu B/\Delta\nu_{\rm d})]^{-1/2}, \end{aligned} \tag{2.3}$$

where $N_{\rm scint}$ is the number of scintles, $T$ and $B$ are total integration time and total bandwidth, respectively, and $\eta_{\rm t}$ and $\eta_\nu$ are filling factors ranging from 0.1 to 0.3 depending on the definitions of characteristic timescale and scintillation bandwidth, and in our case both set to 0.2 (Cordes & Shannon, 2010).

Since all of our observations are at most 30 minutes in length, generally $T < \Delta t_{\rm d}$, and as a result $1+\eta_{\rm t} T/\Delta t_{\rm d} \approx 1$. This allows us to rely exclusively on the observing and scintillation bandwidths when calculating $\epsilon$. It should be noted that this is a conservative approach that can only overestimate our reported uncertainties: if $T \gtrsim \Delta t_d$, then Equation 5.4 shows that we will underestimate $N_{\rm scint}$ and overestimate $\epsilon$ (Levin et al., 2016).

The limited frequency resolution also introduces selection effects into our data. We are unable to reliably measure scintillation bandwidths smaller than our 1.5 MHz wide channel widths. As a result, some of the average scattering delays quoted for the most highly scattered pulsars are lower limits. Due to this bias, we treat an individual scattering measurement $\gtrsim 30$ ns (about three channel widths) as a lower limit for a given epoch.

To account for the wide bandwidth of our observations, we assumed a Kolmogorov medium to stretch each observation's dynamic spectrum by by $\nu^{4.4}$, with the frequency axis being re-scaled to reference frequencies of 820 and 1500 MHz for the respective observing bands as in Levin et al. (2016). If the scaling index used for the stretching is correct, then all scintles in a given dynamic spectrum should be roughly equal in size. Understretching a spectrum (i.e., the epoch has a true index steeper than 4.4) would result in an overestimation of the true scattering delay at a given epoch, and vice-versa for overstretching. In some cases, this stretching can result in scintles at the lower end of the band appearing wider than the width of an individual channel despite physically being narrower, and vice-versa. This means we can then

derive scintillation bandwidths smaller than our channel widths. However, we still interpret our measurements as averages over entire observing bands. As a result, our upper limits will still be determined based on the unstretched channel width at the center of each band.

We have carried out simulations to determine the errors due to the assumption that $-4.4$ is the proper index to use for stretching by placing discrete scintles with some characteristic frequency scaling, stretching using the $-4.4$ scaling, and then measuring the resultant frequency scaling. For index values between $-1$ and $-5$, the average fractional error due to stretching by an incorrect index is roughly 10%. Furthermore, the index values measured will always be biased high, i.e. a flatter scaling than $-4.4$.

**Table 2.3:** Comparison with Previously Published Scintillation Parameters

| | **This work** | | | | **Previously Published Values** | | | | |
|---|---|---|---|---|---|---|---|---|---|
| Pulsar | $\overline{\tau}_{\rm d}$ (ns) | $\overline{\Delta\nu}_{\rm d}$ (MHz) | $\overline{\Delta t}_{\rm d}$ (min) | $\nu$ (MHz) | $\tau_{\rm d,\ scaled}$ (ns) | $\Delta\nu_{\rm d,\ scaled}$ (MHz) | $\Delta t_{\rm d,\ scaled}$ (min) | $\nu_{\rm original}$ (MHz) | Reference |
| J0340+4130 | >33 ± 17 | <3.3 ± 1.3 | — | 1500 | 43 ± 2 | 3.7 ± 0.2 | 16 ± 1 | 1500 | Shapiro-Albert et al. (2020) |
| J0613−0200 | 16 ± 11 | 4 ± 3 | 10 ± 4 | 1500 | 61 | 3 | 26 | 1369 | Coles et al. (2010) |
| ‖ | ‖ | ‖ | ‖ | ‖ | 97* | 2* | 75* | 1500* | Keith et al. (2013) |
| ‖ | ‖ | ‖ | ‖ | ‖ | 21 ± 1 | 7.7 ± 0.5 | 11 ± 1 | 1500 | Shapiro-Albert et al. (2020) |
| ‖ | ‖ | ‖ | ‖ | ‖ | 50−200† | 0.8−3.2 † | — | 1350† | Main et al. (2020)† |
| J1024−0717 | 10 ± 3 | 11 ± 4 | 17 ± 4 | 820 | 5 | 33 | 56 | 685 | Coles et al. (2010) |
| ‖ | 4.4 ± 0.3 | 36 ± 3 | >30 | 1500 | 0.59* | 268* | 70* | 1500* | Keith et al. (2013) |
| J1614−2230 | 16 ± 6 | 6± 3 | 9 ± 3 | 1500 | 29 ± 2 | 5.5 ± 0.4 | 12 ± 1 | 1500 | Shapiro-Albert et al. (2020) |
| J1713+0747 | 3 ± 2 | 23 ± 15 | >30 | 1500 | 7* | 24* | 48* | 1500* | Keith et al. (2013) |
| J1744−1144 | 12 ± 4 | 10 ± 3 | — | 820 | 27 | 6.0 | 26 | 660 | Johnston et al. (1998) |
| ‖ | ‖ | ‖ | ‖ | ‖ | 6 | 28 | 58 | 685 | Coles et al. (2010) |
| ‖ | 3.3 ± 1.6 | 33 ± 13 | >30 | 1500 | 3* | 59* | 35* | 1500* | Keith et al. (2013) |
| B1855+09 | 18 ± 6 | 9 ± 3 | — | 820 | 16 | 10 | 21 | 685 | Coles et al. (2010) |
| ‖ | 8 ± 4 | 10 ± 5 | > 30 | 1500 | 13 | 12 | 37 | 1369 | Coles et al. (2010) |
| ‖ | ‖ | ‖ | ‖ | ‖ | 29* | 6* | 24 | 1500* | Keith et al. (2013) |
| J1909−3744 | >21 ± 12 | <4 ± 2 | 6 ± 2 | 820 | 10 | 17 | 41 | 685 | Coles et al. (2010) |
| ‖ | 4 ± 2 | 28 ± 13 | — | 1500 | 2 ± 0.8 | 81 ± 31 | ¿ 82 | 1500 | Shapiro-Albert et al. (2020) |
| ‖ | ‖ | ‖ | ‖ | ‖ | 4* | 37* | 38* | 1500* | Keith et al. (2013) |
| B1937+21 | >76±43 | <1.5 ± 0.8 | 9 ± 3 | 1500 | 48 | 3 | 7 | 1369 | Coles et al. (2010) |
| ‖ | ‖ | ‖ | ‖ | ‖ | 127 | 1 | 8 | 1400 | Cordes et al. (1990) |
| ‖ | ‖ | ‖ | ‖ | ‖ | 130* | 1* | 6* | 1500 | Keith et al. (2013) |

**Table 2.3:** Comparison with Previously Published Scintillation Parameters

| | This work | | | | Previously Published Values | | | | |
|---|---|---|---|---|---|---|---|---|---|
| Pulsar | $\overline{\tau}_{\rm d}$ (ns) | $\overline{\Delta\nu}_{\rm d}$ (MHz) | $\overline{\Delta t}_{\rm d}$ (min) | $\nu$ (MHz) | $\tau_{\rm d,\ scaled}$ (ns) | $\Delta\nu_{\rm d,\ scaled}$ (MHz) | $\Delta t_{\rm d,\ scaled}$ (min) | $\nu_{\rm original}$ (MHz) | Reference |
| J2145−0750 | $9 \pm 5$ | $7 \pm 4$ | >30 | 820 | 6 | 25 | 58 | 685 | Coles et al. (2010) |
| ‖ | $3.3 \pm 0.8$ | $43 \pm 11$ | >30 | 1500 | 0.82* | 194* | 57* | 1500* | Keith et al. (2013) |

**Table 2.3:** Published values were reported at observing frequency $\nu_{\rm original}$ and converted to the values at the frequency closest to that used in our paper using a scaling index of $\xi = -4.4$. For consistency, we only examined scintillation measurements taken at comparable frequencies. Additionally, as is discussed below, we do not find consistent scaling behavior along the LOSs to different pulsars, and as a result of this variability we felt that attempting to scale scintillation measurements taken at largely disjointed frequencies would not make for a sound comparison. Our scintillation timescale averages are lower than many of the previously measured values at similar frequencies, further providing evidence for the possibility of our timescale averages being biased low as a result of our short observation lengths.
*Only values that were already scaled were reported in the original publication.
†No average value was quoted, but scattering delays were found within this range.

### 2.3.2 Scaling Behavior

With a large enough observation bandwidth, it is possible to place constraints on the scaling behavior of scattering delays as a function of frequency. Levin et al. (2016) were able to break up a few unstretched wideband observations at 1500 MHz into four equal subbands of 200 MHz each, determine $\Delta\nu_{\rm d}$ and $\tau_{\rm d}$ in each unstretched subband using the ACF method described in Section 2.3, and perform a weighted linear fit for $\tau_{\rm d}$ in semi-log space of the form $\nu^{\xi}$ to estimate the scaling index $\xi$ for a given epoch. Some examples of these fits can be seen in Figure 2.3.

We applied this method to four of the pulsars and, as discussed in more detail in Section 2.5.2, found similar results to Levin et al. (2016). We also used this method to look at the time dependence of this scaling index. We found it feasible to perform this method only in the 1500 MHz band, as the 800 MHz band has only 200 MHz of bandwidth and we would have an insufficient number of scintles per subband to effectively utilize this approach.

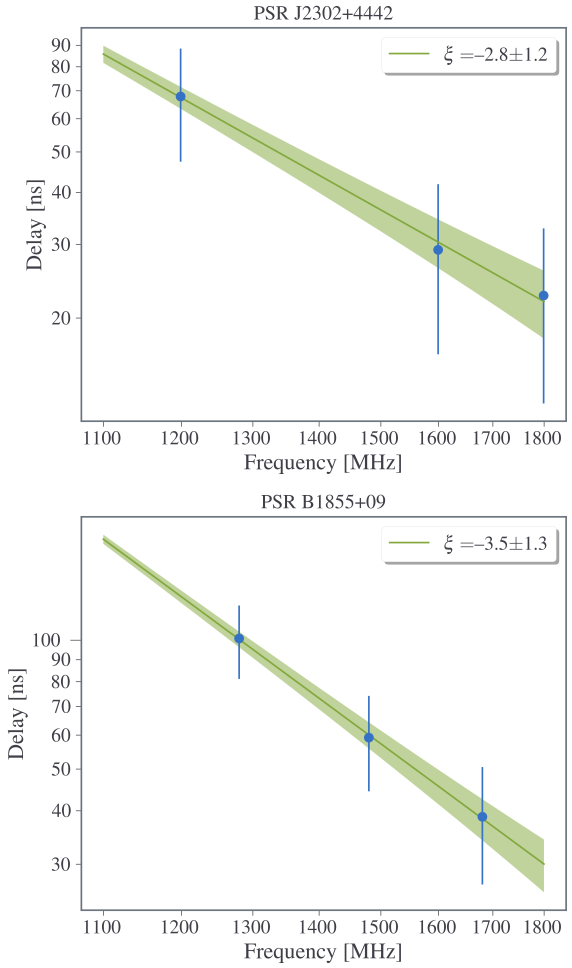


**Figure 2.3:** Top: A subband fit for PSR J2302+4442 at MJD 57921. Bottom: A subband fit for PSR B1855+09 at MJD 57608.

For many of the other pulsars in our data set, we took advantage of our dual frequency measurements to examine scaling indices across a wider frequency range. In this multiband method, we took the weighted averages of scattering delays at 820 and 1500 MHz for pulsars with measurements at both frequencies and performed the same fit described above. An example of one of these fits is shown in Figure 2.4. While this multiband method examines scaling indices differently than Levin et al. (2016), our ability to utilize multiple frequency bands augments

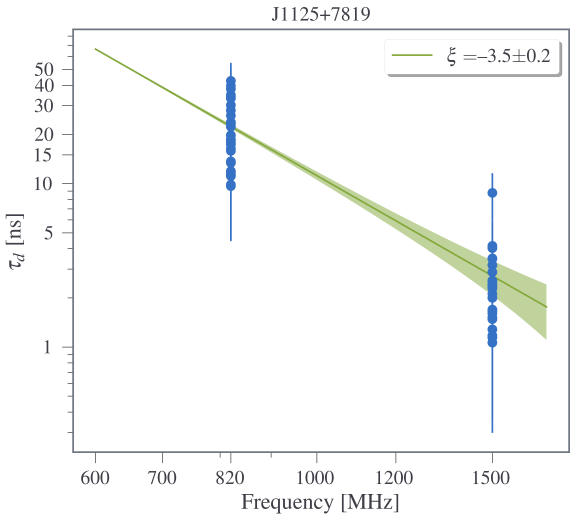


**Figure 2.4:** Example fit in semi-log space of the scaling index $\xi$ over the 820 and 1500 MHz bands for PSR J1125+7819. Each point indicates a measured epoch of scattering delay in a given frequency band with its corresponding $1\sigma$ error.

Levin et al. (2016), who only used 1500 MHz band data. Examining time variability was not possible using the multiband method, since we rarely, if ever, had epochs (observations within a span of about a week) in which we had detectable measurements for two frequencies.

In addition to our multiband method, we were able to utilize the original scaling analysis from Levin et al. (2016) on four pulsars to determine the variation in scaling index over time, as well as PSRs B1855+09 and J2302+4442 to compare the results of the two analyses.

It is important to note that these weighted averages from the multiband analysis are determined using measurements from dynamic spectra that have already been stretched by $\nu^{4.4}$ to account for the wide bandwidth. This will result in some errors on the calculated scaling index. Note that, however, a true $\nu^{-4.4}$ scaling would still yield $\xi = -4.4$.

In the future, new developments such as wideband receivers should allow us to achieve the signal-to-noise ration (S/N) and frequency range necessary to determine the scaling index of an epoch by looking at unstretched spectra and maximizing the S/N of that epoch's frequency ACF (Lam et al., 2017).

### 2.3.3 Transverse Velocities

After recovering interstellar scattering parameters, we estimated transverse velocities for pulsars with measured scintillation timescales. Transverse velocities for many NANOGrav pulsars have already been inferred from proper motions, defined as

$$V_{\rm pm} = 4.74 \mu D_{\rm kpc}, \tag{2.4}$$

where $V_{\rm pm}$ is in units of km s$^{-1}$, $\mu$ is proper motion in units of mas yr$^{-1}$, and $D_{\rm kpc}$ is the distance to the pulsar in kiloparsecs, but they can also be estimated from scintillation behavior, assuming the surrounding ISM can be interpreted as stationary relative to the pulsar in question.

Merging the expressions for transverse velocity from Gupta et al. (1994) and Cordes & Rickett (1998) for greater generality, we have

$$V_{\rm ISS} = A_{\rm ISS} \frac{\sqrt{\Delta\nu_{\rm d,MHz} D_{\rm kpc} x}}{\nu_{\rm GHz} \Delta t_{\rm d,s}}, \tag{2.5}$$

where $\Delta\nu_{\rm d,MHz}$ is the scintillation bandwidth in MHz, $\Delta t_{\rm d,s}$ is the scintillation timescale in seconds, $D_{\rm kpc}$ is the distance to the pulsar in kpc, $\nu_{\rm GHz}$ is the observation frequency in GHz, and $A_{\rm ISS}$ is a factor dependent on assumptions regarding the geometry and uniformity of the medium.

In this analysis, we have assumed a thin screen and a Kolmogorov medium as in Cordes & Rickett (1998), and so $A_{\rm ISS} = 2.53 \times 10^4$ km s$^{-1}$. As used in Gupta et al. (1994), we define $x = D_{\rm o}/D_{\rm p}$, where $D_{\rm o}$ is the distance from the observer to the screen and $D_{\rm p}$ is the distance from the screen to the pulsar. For the calculation of $V_{\rm ISS}$, we assume the screen is halfway between us and the observed pulsars, and so $D_{\rm o} = D_{\rm p}$, meaning $x = 1$. Additionally, we ignore orbital velocities (for binary pulsars) and the Earth's velocity, and assume the screen is isotropic. We encourage our readers to look at Rickett et al. (2014), Reardon et al. (2019), Reardon et al. (2020b), and Main et al. (2020) for examples of significant orbital and annual variations of scintillation timescales, non-zero screen velocities, and non-isotropic scattering. For

the calculation of $V_{\rm pm}$, we used distances determined by parallax measurements if $\sigma_D/D < 0.25$, otherwise we used the DM distance determined by the NE2001 electron density model.

The ability to independently determine transverse velocities from different sets of physical quantities also helps us determine whether the ISM behaves as Kolmogorov with a scattering screen at the halfway point. We expect transverse velocities derived from proper motions to be more accurate, as proper motions are generally measured with much greater precision and with fewer selection effects than scintillation parameters. Consequently, comparisons of those results serve as a strong indicator of the accuracy of ISS-derived transverse velocities. In addition, there are a number of pulsars, in particular, non-recycled, for which we are unable to measure high quality timing-derived proper motions, so it is useful to have alternative ways of measuring transverse velocities.

## 2.4 Results

### 2.4.1 Scintillation Parameters and Variations

Our measurements of interstellar scattering delays, scintillation bandwidths, and scintillation timescales are given in Table 2.1, with barred parameters ($\overline{\tau}_{\rm d}$, $\overline{\Delta\nu}_{\rm d}$, etc.) representing the ensemble weighted averages of the individual observations. We determined values for $\overline{\tau}_{\rm d}$ by calculating $\tau_{\rm d}$ values for individual epochs and then averaging them, rather than directly converting $\overline{\Delta\nu}_{\rm d}$. For comparison, in Tables 2.2 and 2.3, we also list the predicted scintillation parameters from the NE2001 Galactic electron density model (Cordes & Lazio, 2002) and the results from previous studies of these pulsars, respectively. Due to our short observation lengths, our $\overline{\Delta t_{\rm d}}$ values should probably be taken as lower limits in most cases since there were many epochs where scintles were not resolvable in time. An clear exception to this rule is PSR B1937+21, for which all scintles were smaller than our observation length. Other likely exceptions to this rule likely include but are not necessarily limited to PSR J1125+7819 at 820 MHz and PSR J0636+5128. There are a few pulsars where we quote scintillation bandwidths

but neither scintillation timescales nor timescale upper limits; since many epochs from these pulsars contain the beginnings and ends of many scintles but never complete scintles, these pulsars all likely have scintillation timescales within 5−10 minutes of our observation lengths of 30 minutes.

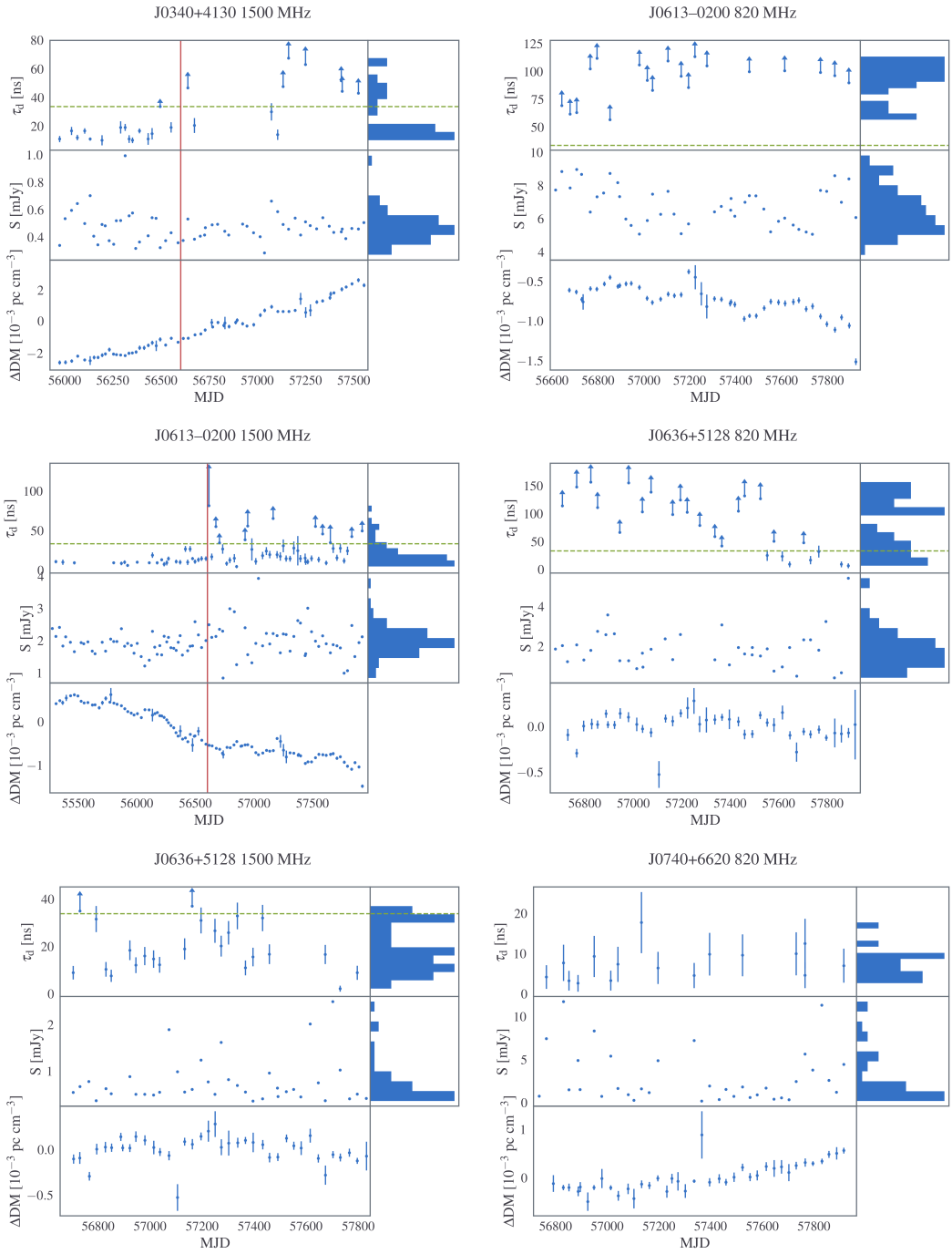
J0340+4130 1500 MHz
J0613–0200 820 MHz
J0613–0200 1500 MHz
J0636+5128 820 MHz
J0636+5128 1500 MHz
J0740+6620 820 MHz
$\tau_d$ [ns]
S [mJy]
$\Delta$DM [$10^{-3}$ pc cm$^{-3}$]
MJD

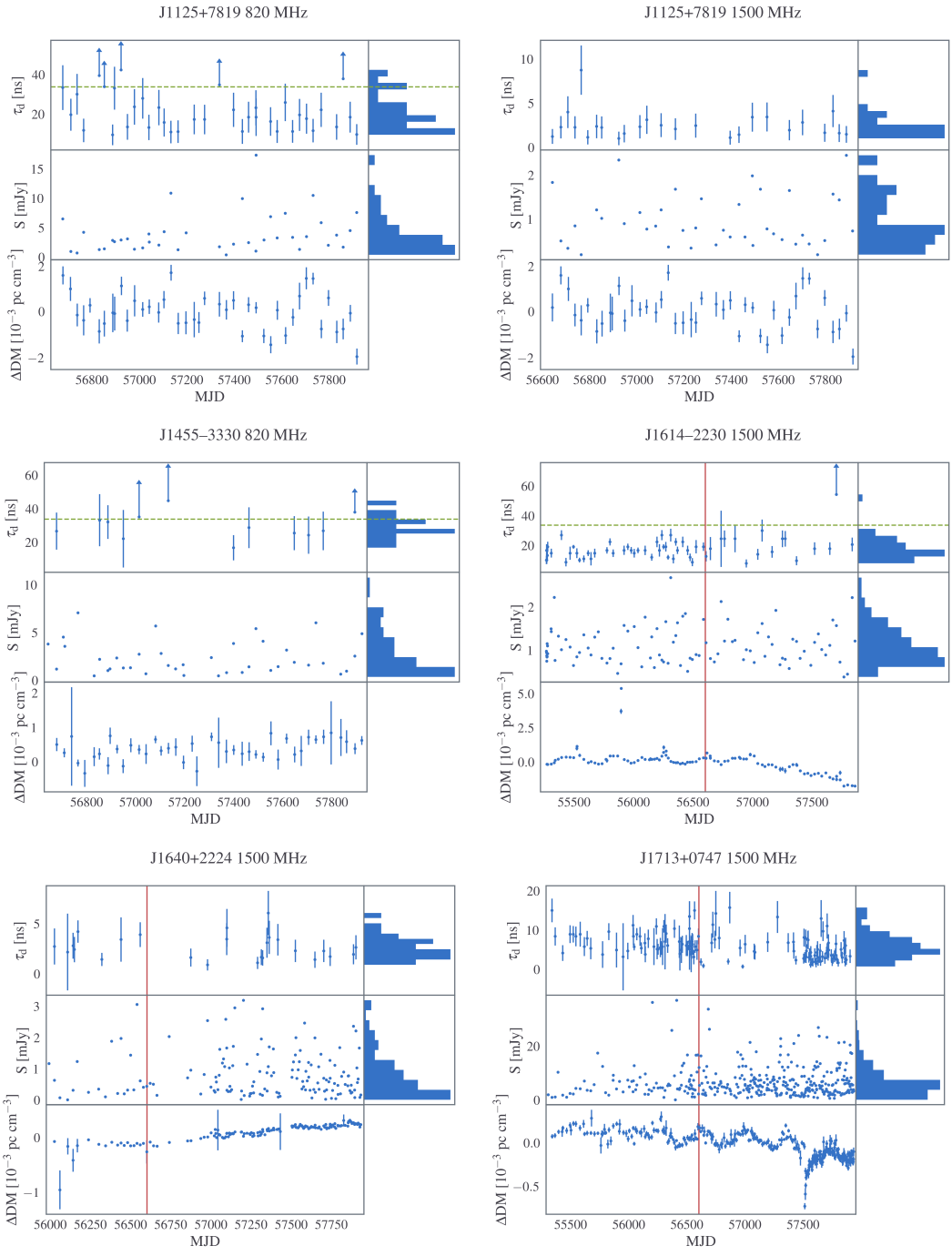
J1125+7819 820 MHz
J1125+7819 1500 MHz
J1455–3330 820 MHz
J1614–2230 1500 MHz
J1640+2224 1500 MHz
J1713+0747 1500 MHz
τd [ns]
S [mJy]
ΔDM [10−3 pc cm−3]
MJD

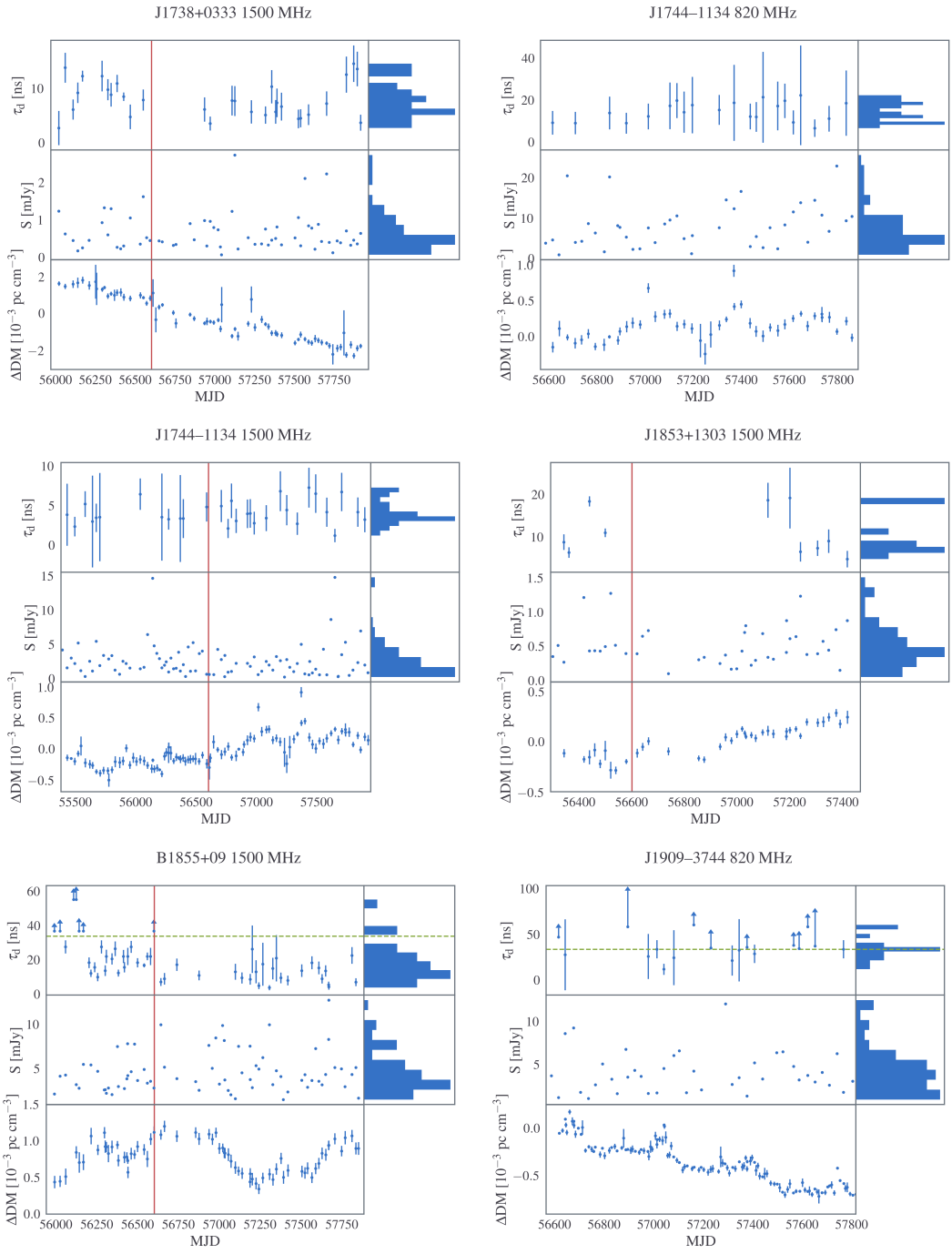
J1738+0333 1500 MHz
J1744–1134 820 MHz
J1744–1134 1500 MHz
J1853+1303 1500 MHz
B1855+09 1500 MHz
J1909–3744 820 MHz
τd [ns]
S [mJy]
ΔDM [10−3 pc cm−3]
MJD

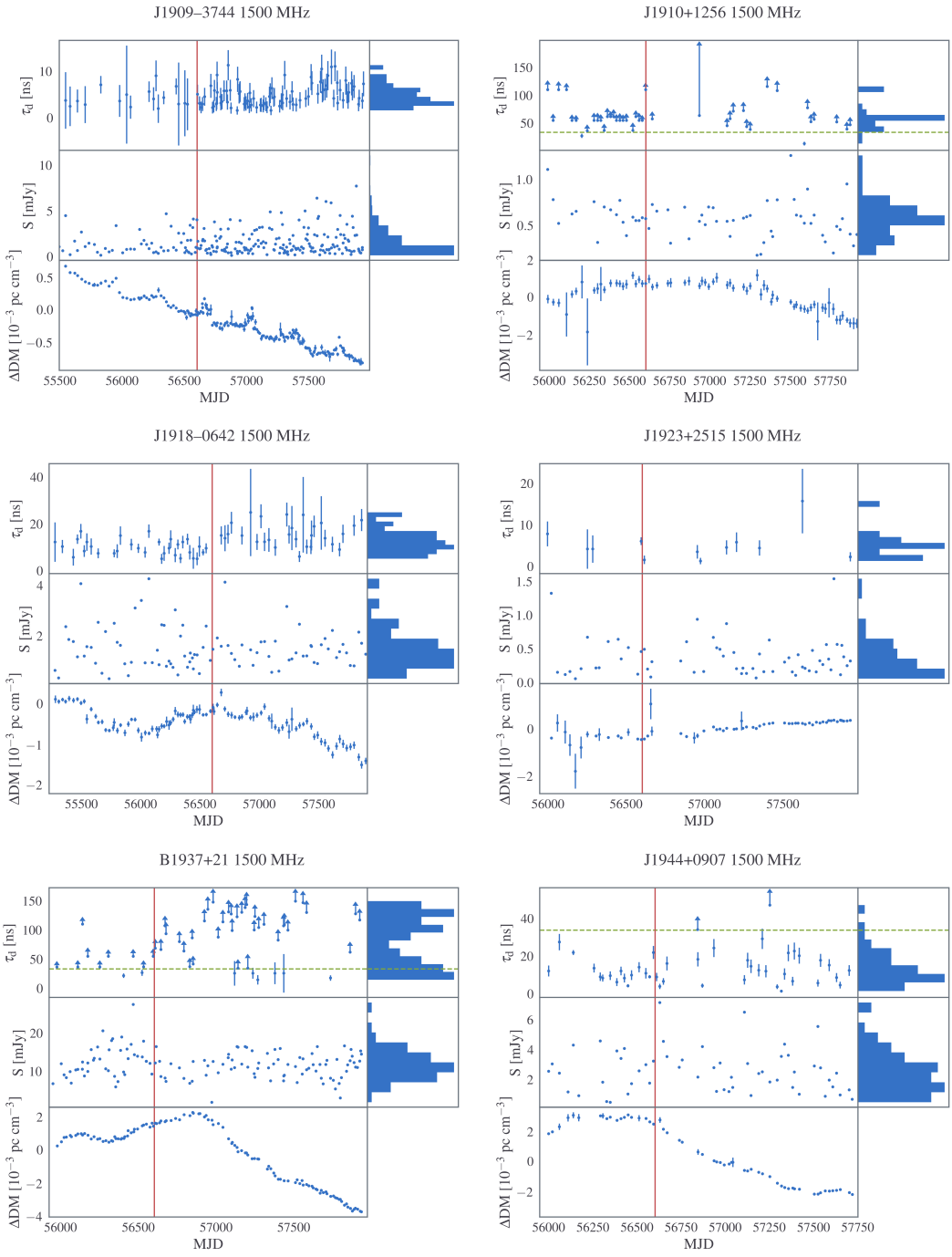
J1909–3744 1500 MHz
J1910+1256 1500 MHz
J1918–0642 1500 MHz
J1923+2515 1500 MHz
B1937+21 1500 MHz
J1944+0907 1500 MHz
$\tau_d$ [ns]
S [mJy]
$\Delta$DM [$10^{-3}$ pc cm$^{-3}$]
MJD

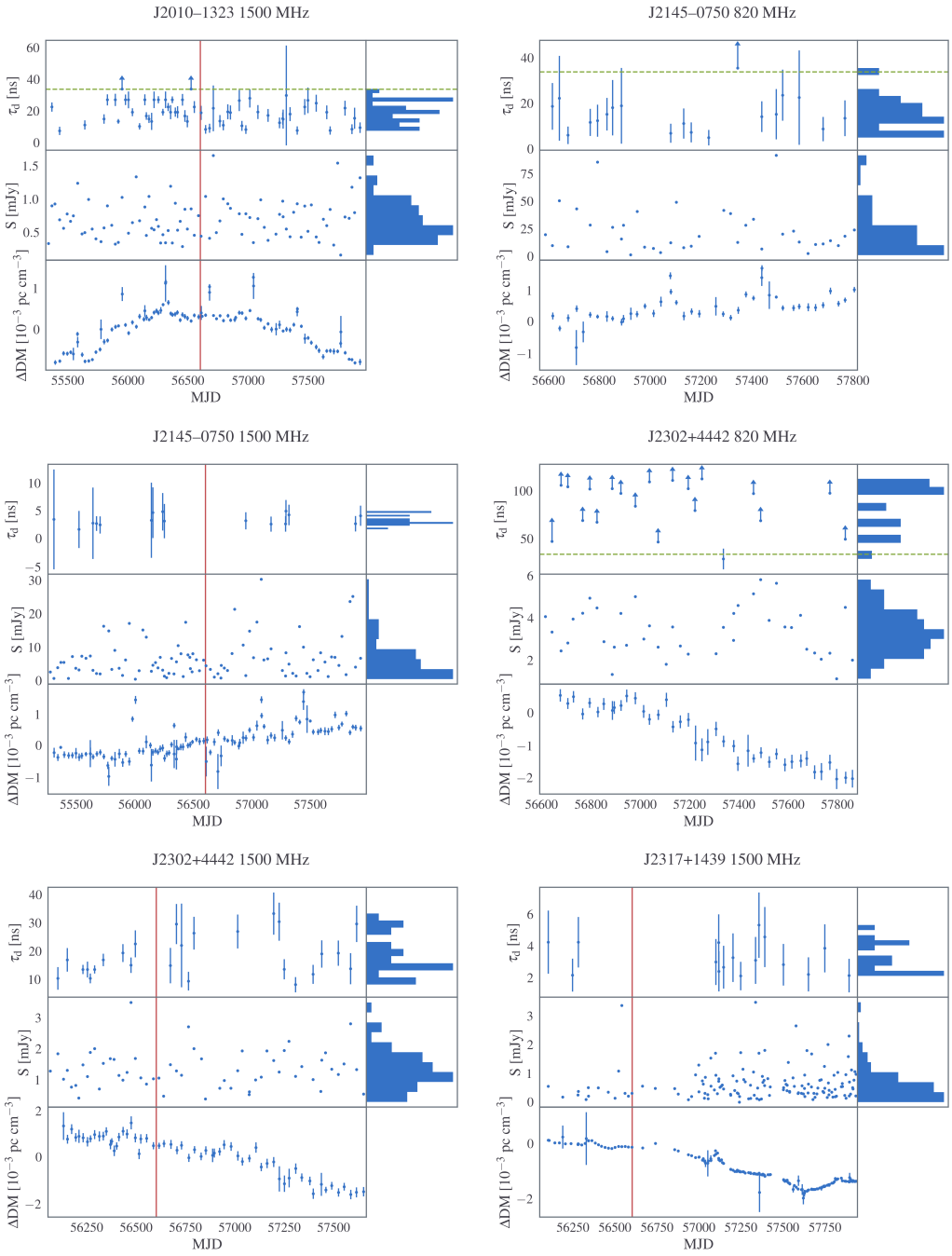


**Figure 2.5:** Variation of $\tau_{\rm d}$ with time from this paper and Levin et al. (2016) at 820 and 1500 MHz along with flux density measurements and $\Delta$DM values that have been mean subtracted and do not account for solar wind effects. Histograms showing the distributions of $\tau_{\rm d}$ and $S$ are shown on the right side of each plot. Errors shown on $\Delta$DM represent the variance. Only pulsars with at least 10 $\tau_{\rm d}$ measurements are shown. Vertical red lines indicate dates separating measurements from Levin et al. (2016) and this paper. Horizontal dashed green lines indicate the maximum scattering delay below which we consider measurements lower limits, taken as the scattering delay corresponding to three channel widths (approximately 30 ns). Fluxes and DMX values were obtained from NANOGrav's wideband timing analysis (Alam et al., 2020c).

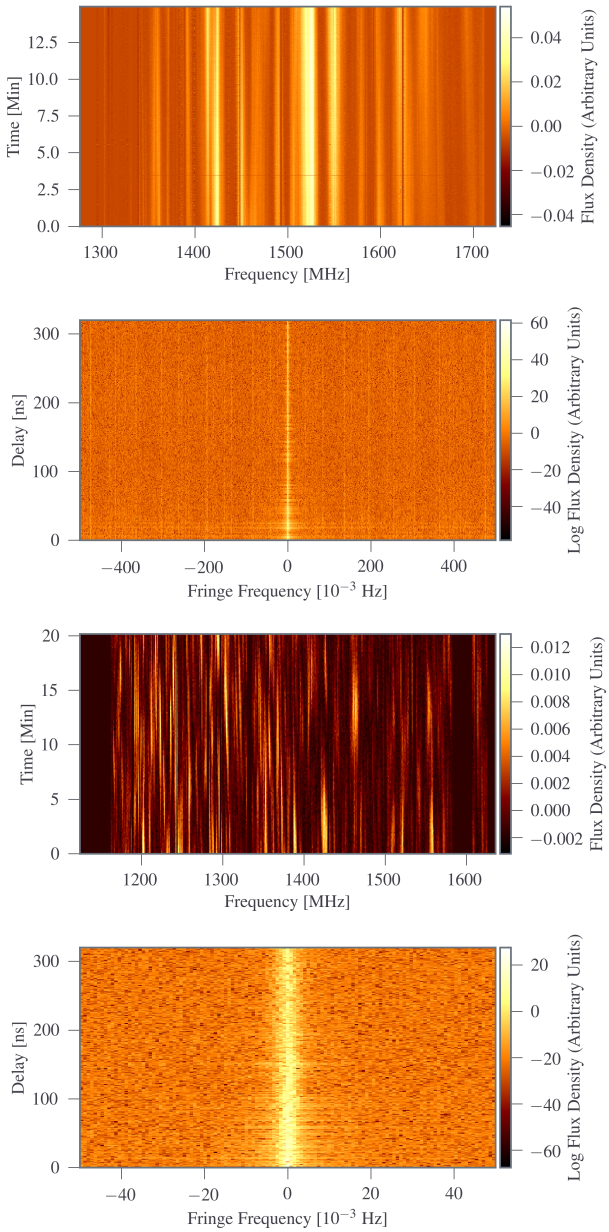


**Figure 2.6:** Dynamic (top) and secondary (second from top) spectra of PSR B1855+09 on MJD 56640 and dynamic (second from bottom) and secondary (bottom) spectra of PSR B1937+21 on MJD 56892. For PSR B1855+09, the intensity in the secondary spectrum drops off at higher delays, indicating we are fully resolving most of its power and properly measuring its scattering delays. For PSR B1937+21, the intensity in the secondary spectrum does not drop off at higher delays, indicating we are not fully resolving its power and are therefore underestimating its scattering delays.

For Table 2.2, the predicted $\Delta t_{\rm d}$ values were calculated using transverse velocities derived from proper motions. Additionally, DM distances were used for calculating transverse velocities if $\sigma_{\rm PX}/{\rm PX} > 0.25$. The values are weighted averages over all measured epochs. Scattering delays over time from this paper and Levin et al. (2016) can be found in Figure 2.5. A more detailed discussion of these plots can be found in Section 2.5.1.

In our new observations we were unable to measure scintillation parameters for five pulsars (PSRs J0023+4130, J1741+1451, B1953+29, J2017+0603, and J2214+3000) that had measureable parameters in Levin et al. (2016). All of these pulsars had 10 or fewer usable observations in that paper and three of them had five or fewer usable measurements. For some of these pulsars, the scintles were too faint, or RFI corrupted too large a portion of each spectrum to obtain scintillation parameters. For example, in quite a few 1.5 GHz observations, the bottom 100–200 MHz of the band was completely corrupted by RFI, and so we either were unable to use many of those epochs or were forced to work with reduced-bandwidth data. In general, the number of measurements obtained on a pulsar-by-pulsar basis in this paper is still largely consistent with Levin et al. (2016) over a similar period of time.

Some of the pulsars in Figure 2.5 show more variability in their scattering delays in our data than in Levin et al. (2016) (see PSR J1614–2230 for a good example of this). One reason for this is our ACF calculation method: Levin et al. (2016) limited their scintillation bandwidth estimates to integer multiples of the channel bandwidths, whereas our fit interpolated between bins, which means we had more possibilities for quoted scintillation bandwidths and therefore a higher likelihood of variation in our values. The errors in some pulsars are also noticeably larger in our data; this can be attributed largely to RFI, which resulted in larger finite scintle errors due to the smaller effective observing bands.

We treat the weighted average scintillation bandwidth measurements for five pulsars at 820 MHz and two pulsars at 1500 MHz as upper limits, as their estimates are less than three times the channel width. For these pulsars, in particular PSRs B1937+21 and J1910+1256, there are typically many epochs on which the bandwidth was unresolved. We can also demonstrate insufficient frequency resolution for some pulsars through the calculation of secondary spectra,

which are the two-dimensional Fourier power spectra of the dynamic spectra. The delay axis in a given secondary spectrum is directly proportional to the relative time delay incurred from scattering (Stinebring et al., 2001b; Hemberger & Stinebring, 2008a). The Fourier relation between the two spectra is also especially useful, as small features such as unresolved scintles in a dynamic spectrum will manifest as large, clearly visible features in a secondary spectrum. As an example, in Figure 2.6, we show dynamic and secondary spectra of PSRs B1855+09 and B1937+21.

In Figure 2.7, we show the average power in the secondary spectrum as a function of delay over the fringe frequency channels in the secondary spectra where power was visible. This corresponds approximately to the middle four channels for PSR B1855+09 and the middle seven channels for PSR B1937+21. We find little dependence on the exact number of channels used for this analysis. PSR B1937+21 displays no decrease in intensity with delay in its secondary spectrum, indicating its scintles are not fully resolved. For this pulsar, we see this effect in all of its secondary spectra, meaning we should interpret all measured delays as lower limits. The flux density in PSR B1855+09's secondary spectra drops off at higher delays, indicating we are resolving more of its scintles, even if narrower ones may not be completely resolved. Some of the remaining power at higher delays could also be due in part to unmitigated RFI.

Overall, we find that power does not dissipate for epochs on which the scintillation bandwidth is less than three channel bandwidths, supporting our decision to treat these measurements as upper limits.

### 2.4.2 Scaling over Multiple Frequency Bands

Since we were unable to resolve scintles at 820 MHz, power-law indices for PSRs B1937+21 and J2010–1323 as shown in Table 2.4 were found exclusively by splitting the 1500 MHz passband into 200 MHz subbands, measuring the scattering in each, and fitting via a power law (as in Levin et al. (2016)). Indices for PSRs B1855+09 and J2302+4442 were found using both this method and extended fits that included the 820 MHz passband. The measured

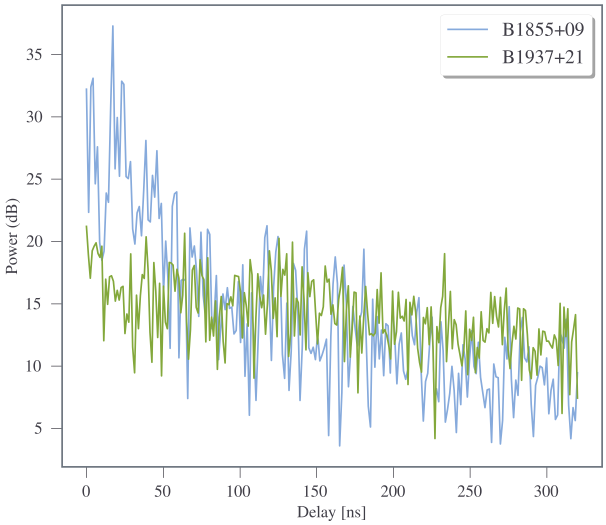


**Figure 2.7:** Power in the secondary spectra of PSRs B1855+09 and B1937+21 as a function of delay, calculated by summing over only the fringe frequencies with visible power. The power of PSR B1937+21 does not decrease at higher delays, indicating that we are underestimating scattering delays. Conversely, the power of PSR B1855+09 falls off with delay, indicating we are more accurately estimating its scattering delays and resolving a greater fraction of its scintles.

indices for all four of these pulsars were shallower than the $-4.4$ expected for a Kolmogorov medium, with only PSR B1937+21 yielding an index steeper than $-3$ while the other three pulsars clustered around $-2.5$.

We were also able to obtain first-order estimates of the scaling index for 15 pulsars using the method described in Section 2.3.2. These results, along with the results described above, are shown in Table 2.4. As in Levin et al. (2016), all of our measured scaling indices are shallower than the value of $-4.4$ that is expected for a Kolmogorov medium under the simplest assumptions, with only two of these indices being steeper than $-3$. There was also considerable range in the indices measured, with values spanning from $-0.7$ to $-3.5$. We quote upper limits on indices where the majority of 820 MHz scattering delays are lower limits.

Levin et al. (2016) found noticeably different scaling indices from multiple measurements of various pulsars, indicting that a pulsar's scaling index may vary with time as it moves through

the ISM. As mentioned earlier, examining time variability was not possible using the multiband method, since we rarely, if ever, had detectable measurements for two frequencies within about a week of each other. A large part of this was because RFI contamination was much more prominent at the 1500 MHz band than in the 820 MHz band, so it was generally easier to get consistent measurements only at lower frequencies. This RFI contamination also made it difficult to get many epochs that were useable for the subband analysis. Overall, since our multiband method can tell whether a scaling index is shallower or steeper than $-4.4$, even if it is not as precise due to the frequency scaling, and both methods found shallower indices, we can conclude that these two methods agree with each other.

### 2.4.3 Transverse Velocity Measurements

A comparison between transverse velocities derived from scintillation parameters and those derived from proper motions is shown in Table 2.5 and below in Figure 2.8. Because we expect that $V_{\rm ISS}$ and $V_{\rm pm}$ should be equal under the assumptions made in Section 2.3.3 and based on surveys such as Nicastro et al. (2001), we use the Pearson correlation coefficient,

$$r_p = \frac{\sigma^2_{x,y}}{\sqrt{\sigma^2_x \sigma^2_y}}, \tag{2.6}$$

where $\sigma^2_{x,y}$ is the covariance between some parameters $x$ and $y$ and $\sigma_x$ and $\sigma_y$ are the variances of $x$ and $y$, respectively. Relative screen distances calculated by assuming that $V_{\rm ISS}$ is equal to $V_{\rm pm}$ are also shown. All $V_{\rm pm}$ values were calculated using proper motions found in Alam et al. (2020a). We are not sensitive to epoch-to-epoch variations in $V_{\rm ISS}$ because our scintles are not always resolved in time for every epoch that they are resolved in frequency. Because of this, all $V_{\rm ISS}$ values were calculated by using the weighted averages of scintillation bandwidth and timescale from Table 2.1 in Equation 2.5 for pulsars with at least two epochs for which $\Delta\nu_{\rm d}$ was measured.

For pulsars where we could not resolve scintles in time, we have assigned $\Delta t_{\rm d}$ lower limits of 30 minutes, resulting in upper limits on transverse velocity. We used parallax distances

for calculating $V_{\rm ISS}$ and $V_{\rm pm}$ if the distance error was $< 25\%$; otherwise we used distances determined by DM from NE2001 and assumed a 20% uncertainty (Cordes & Lazio, 2002).

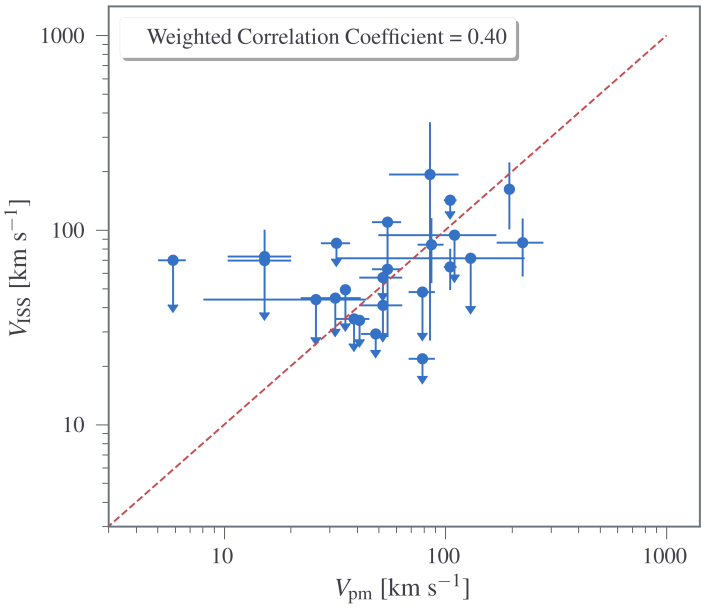


**Figure 2.8:** Transverse velocities derived from proper motion vs those determined through scintillation. Downward-facing arrows indicate upper limits. The modest correlation suggests that our assumption of a screen at the midpoint between us and the pulsar is roughly correct.

**Table 2.4:** Estimated Scattering Delay Scaling Indices

| Pulsar | $\xi$ |
|---|---|
| J0613−0200 | $< -1.8 \pm 0.8$ |
| J0636+5128 | $< -2.5 \pm 0.1$ |
| J0740+6620 | $-2.4 \pm 0.6$ |
| J1024−0719 | $-1.5 \pm 0.6$ |

**Table 2.4:** Estimated Scattering Delay Scaling Indices

| Pulsar | $\xi$ |
|---|---|
| J1125+7819 | $-3.5 \pm 0.2$ |
| J1455−3330 | $-3.5 \pm 0.4$ |
| J1614−2230 | $< -1.3 \pm 0.9$ |
| J1744−1134 | $-1.8 \pm 0.3$ |
| B1855+09 | $-0.7 \pm 0.5$ |
| B1855+09 | $-2.4 \pm 0.3^{\dagger}$ |
| J1909−3744 | $< -2.9 \pm 0.3$ |
| J1910+1256 | $< -1.0 \pm 0.3$ |
| B1937+21 | $-3.6 \pm 0.1^{\dagger}$ |
| J1944+0907 | $-1.0 \pm 0.3$ |
| J2010−1323 | $-2.5 \pm 0.4^{\dagger}$ |
| J2145−0750 | $-2.1 \pm 0.4$ |
| J2302+4442 | $< -1.3 \pm 0.4$ |
| J2302+4442 | $-2.6 \pm 1.1^{\dagger}$ |
| J2317+1439 | $-2.3 \pm 0.8$ |

**Table 2.4:** Measurements with a dagger were calculated using non-stretched subbands, and others used measurements at two frequencies based on stretched spectra. Uncertainties on values with daggers represent the weighted error of all measured indices, while uncertainties on values without daggers represent the $1\sigma$ errors on $\xi$ in the model fits. We quote upper limits on indices where the majority of 820 MHz scattering delays are lower limits.

**Table 2.5:** Pulsar Transverse Velocities Inferred from Interstellar Scattering and Proper Motions

| Pulsar | Frequency (MHz) | $V_{\rm ISS}$ (km s$^{-1}$) | $V_{\rm pm}$ (km s$^{-1}$) | $D_{\rm o}/D_{\rm p}$ |
|---|---|---|---|---|
| J0613−0200 | 820 | 110 ± 45 | 55 ± 8 | 0.3 ± 0.2 |
| J0613−0200 | 1500 | 63 ± 35 | 55 ± 8 | 0.8 ± 0.8 |
| J0636+5128 | 820 | <75 ± 43 | 15 ± 5 | 0.04 ± 0.05 |
| J0636+5128 | 1500 | 70 ± 32 | 15 ± 5 | 0.05 ± 0.04 |
| J0931−1902 | 1500 | <44 ± 16 | 26 ± 18 | >0.4 ± 0.3 |
| J1024−0719 | 820 | 86± 12 | 220 ± 90 | 6.7 ± 4.4 |
| J1125+7819 | 820 | 84 ± 21 | 86 ± 12 | 1.1 ± 0.8 |
| J1614−2230 | 820 | 140 ± 20 | 110 ± 10 | 0.5 ± 0.1 |
| J1614−2230 | 1500 | 65 ± 16 | 110 ± 10 | 2.6 ± 1.3 |
| J1640+2224 | 1500 | <94 ± 35 | 110 ± 60 | >1.4 ± 1.0 |
| J1713+0747 | 1500 | <44 ± 12 | 36 ± 1 | >0.7 ± 0.3 |
| J1738+0333 | 1500 | <72 ± 31 | 130 ± 100 | >3.3 ± 2.9 |
| J1744−1134 | 1500 | <34 ± 7 | 41 ± 1 | 1.4 ± 0.6 |
| J1853+1303 | 1500 | <45 ± 14 | 32 ± 10 | >0.5 ± 0.3 |
| B1855+09 | 1500 | <35 ± 9 | 39 ± 7 | >1.2 ± 0.6 |
| J1909−3744 | 820 | <160 ± 60 | 190 ± 4 | >1.4 ± 1.1 |
| J1910+1256 | 820 | <48 ± 19 | 79 ± 11 | >2.7 ± 2.1 |
| J1910+1256 | 1500 | <22 ± 4 | 79 ± 11 | > 12.9 ± 4.9 |
| J1918−0642 | 1500 | <29 ± 5 | 48 ± 7 | >2.7 ± 0.9 |

**Table 2.5:** Pulsar Transverse Velocities Inferred from Interstellar Scattering and Proper Motions

| Pulsar | Frequency (MHz) | $V_{\rm ISS}$ (km s$^{-1}$) | $V_{\rm pm}$ (km s$^{-1}$) | $D_{\rm o}/D_{\rm p}$ |
|---|---|---|---|---|
| B1937+21 | 1500 | $< 70 \pm 29$ | $6 \pm 1$ | $> 0.01 \pm 0.01$ |
| J2010−1323 | 1500 | $190 \pm 170$ | $85 \pm 29$ | $0.2 \pm 0.3$ |
| J2145−0750 | 820 | $<41 \pm 12$ | $52 \pm 11$ | $>1.6 \pm 0.9$ |
| J2145−0750 | 1500 | $<57 \pm 9$ | $52 \pm 11$ | $>0.8 \pm 0.3$ |
| J2317+1439 | 1500 | $<86 \pm 14$ | $32 \pm 5$ | $>0.1 \pm 0.1$ |

**Table 2.5:** $V_{\rm ISS}$ values were calculated using the weighted averages of $\Delta\nu_{\rm d}$ and $\Delta t_{\rm d}$ found in Table 2.1 and the assumption that the scattering screen is equidistant from the pulsar and Earth. Uncertainties are calculated by propagating the weighted errors on the scintillation measurements with the uncertainties on pulsar distance and proper motion. Many of the $V_{\rm ISS}$ estimations are upper limits, since scintillation timescale lower limits were used. We calculated $D_{\rm o}/D_{\rm p}$ by assuming that $V_{\rm pm}$ is correct, setting it equal to $V_{\rm ISS}$, and solving for $D_{\rm o}/D_{\rm p}$. Some measurements are also upper limits due to resolution limits on scintillation bandwidths. Due to the large uncertainty in both PSRs J1125+7819 and J1910+1256's parallax measurements, their distance was determined by DM via NE2001. All measurements and errors have been rounded to the last significant digit shown.

## 2.5 Discussion

### 2.5.1 Scattering Variability and Correlations with Dispersion Measure & Flux Density Variations

We have searched for correlations between scattering delays and DM variations and scattering delay and flux density for pulsars with at least 10 scattering measurements. These coefficients were determined using only epochs where both scattering delay and $\Delta$DM or flux

data were available. The data and their corresponding correlations with ΔDM and flux density are shown in Figure 2.5 and Table 2.6, respectively. Here, we only examine the linear Pearson correlation (Equation 2.6) since theoretical predictions in the literature show support for this type of correlation. DMs and flux densities were obtained from NANOGrav's wideband timing analysis (Alam et al., 2020c). DMX determines DM variations by treating DM($t$) as a piecewise constant and fitting for a new DM at up to six day intervals along with the rest of the parameters in our timing model.

In order to examine the variability of the flux density in each pulsar as a function of time, we performed a reduced $\chi^2$ analysis using a model consisting of the weighted average of the combined flux densities. For a given time series with measurements of a parameter, $x$, we define our reduced $\chi^2$ as

$$\chi_r^2 = \frac{1}{N-1} \sum \frac{(x(t) - \overline{x})^2}{\sigma^2(t)}, \tag{2.7}$$

where $N$ is the number of measurements, $\overline{x}$ is the weighted average of the measurements, $x(t)$ is the measurement at time $t$, and $\sigma^2(t)$ is the measurement variance at time $t$. In the case of the fluxes, $x(t)$ and $\overline{x}$ in Equation 2.7 represent the flux density as a function of time and the weighted average of the flux density, respectively. We list these values in Table 2.6.

While there may visually be correlations between scattering delay and DM or flux, these correlations do not appear linear. For this reason, in addition to examining linear correlations using the Pearson correlation coefficient (Equation 2.6), we examine general correlations using the Spearman correlation coefficient,

$$r_s = 1 - \frac{6 \sum_{i=1}^{N} [\mathrm{rg}(y_i) - \mathrm{rg}(x_i)]^2}{N(N^2 - 1)}, \tag{2.8}$$

where $\mathrm{rg}(y_i)$ and $\mathrm{rg}(x_i)$ are the ranks of the $i^{\mathrm{th}}$ values of $y$ and $x$, respectively, and $N$ is the number of data points being used. The rank of a value is defined by its size relative to other quantities in a shared data set, with the smallest value having a rank of one, the second smallest value having a rank of two, and so on.

We also examined the variability of scattering delays as a function of time by performing a reduced $\chi^2$ analysis using the combined scattering delays from this paper and Levin et al. (2016), with $x(t)$ and $\overline{x}$ in Equation 2.7 representing the scattering delays as a function of time and the weighted average of the scattering delays, respectively. The results are shown in Table 2.6.

Finally, we explored the variability of scattering delays by examining the scintillation bandwidth modulation index, defined as

$$m_{\rm b} = \frac{1}{\langle \Delta\nu_{\rm d} \rangle} \left( \frac{1}{N_{\rm obs} - 1} \sum_{i=1}^{N_{\rm obs}} \left( \Delta\nu_{\rm d,i} - \langle \Delta\nu_{\rm d} \rangle \right)^2 \right)^{1/2}, \tag{2.9}$$

where $\langle \Delta\nu_{\rm d} \rangle$ is the average scintillation bandwidth, $N_{\rm obs}$ is the number of observations, and $\Delta\nu_{{\rm d},i}$ is the scintillation bandwidth at the $i^{\rm th}$ epoch (Bhat et al., 1999a). We correct these indices for the estimation error following Bhat et al. (1999a),

$$m^2_{\rm b;corrected} = m^2_{\rm b;measured} - m^2_{\rm b;error}, \tag{2.10}$$

where $m_{\rm b;measured}$ and $m_{\rm b;error}$ are the modulation indices found from using the scintillation bandwidth measurements and errors, respectively, in Equation 2.9. The estimation error-corrected modulation indices for pulsars with more than 10 measurements can be found in Table 2.6. Some low-DM pulsars had negative $m_{\rm b;corrected}$ values due to the finite scintle effect; we do not list modulation indices in these cases. There are also likely some instances where the scintles are not fully resolved, such as PSR B1937+21. In cases like this, the $m^2_{\rm b;error}$ may be overestimated.

We can also compare these results with the theoretic prediction, assuming a Kolmogorov medium with a thin screen halfway between us and the pulsar, as in Romani et al. (1986):

$$m_{\rm b;Kolmogorov} \approx 0.202 (C^2_{\rm n})^{-1/5} \nu^{3/5}_{\rm obs} D^{-2/5}, \tag{2.11}$$

where $\nu_{\rm obs}$ is the observing frequency in GHz, $D$ is the distance to the pulsar in kpc, and $C_{\rm n}^2$ describes the strength of scattering effects in units of $10^{-4}$ m$^{-20/3}$ (Bhat et al., 1999a), and is given by

$$C_{\rm n}^2 = 0.002 \Delta\nu_{\rm d}^{-5/6} D^{-11/6} \nu_{\rm obs}^{11/3} {\rm m}^{-20/3} \tag{2.12}$$

for a Kolmogorov medium, with $\Delta\nu_{\rm d}$ in MHz (Cordes, 1986a). We calculated $m_{\rm b;Kolmogorov}$ for each pulsar with at least 10 measurements. The results are shown in Table 2.6.

As mentioned in Section 2.1, dispersion is the largest source of delay from the ISM and is usually the only ISM effect that is corrected for by PTAs. Since both dispersion and scattering are ISM effects originating from the same structures along the LOS, it would be reasonable to expect a correlation between the two quantities on an epoch-to-epoch basis. Rankin & Counselman (1973) examined correlations between dispersion and scattering for the Crab pulsar during a period of activity from late 1969 to late 1970. It appears that there may be an approximately one-month lag between changes in dispersion and scattering, although it is difficult to say these events are actually correlated. McKee et al. (2018) looked at around six years of observations of the Crab pulsar and claimed evidence of correlations between $\tau_{\rm d}$ and DM. However, the strength of these correlations is mild, with a correlation coefficient of only 0.56±0.01. Kuzmin, A. et al. (2008) also made observations of the Crab pulsar over a 200 day period coinciding with a large ISM event due to an ionized cloud or filament crossing the LOS, over which time both $\tau_{\rm d}$ and DM followed very similar time signatures. Correlations between these two parameters have also been explored in MSPs in many contexts. Coles et al. (2015) examined case of extreme scattering events and found sharp increases in DM are seen to clearly mirror sharp increases in scattering delay in by-eye examinations of the data. In simulated data, Lentati et al. (2017) found scattering delays to be correlated in a non-linear way with both the pulse TOA and DM. McKee et al. (2019) looked at giant pulses from PSR B1937+21 and found no correlation between scattering and DM despite earlier studies finding such correlations using giant pulses in the Crab pulsar (McKee et al., 2018). Main et al. (2020) examined the scintillation arcs of PSR J0613–0200 and found that the arc curvature followed the annual variation

seen in DM. It is possible that in our data the scattering delays are partially absorbed into DMX fits, decreasing any measured correlation, as suggested by Shapiro-Albert et al. (2021).

It is well known that RISS affects flux densities. Stinebring et al. (2000b) found that pulsars with larger DMs had more stable flux densities, suggesting that flux density variations in nearby pulsars were due to propagation effects such as RISS. Romani et al. (1986) found that scintillation bandwidth and flux should be strongly anticorrelated, given a thin-screen ISM model. In addition, both Stinebring et al. (1996) and Bhat et al. (1999b) observed these same correlations, though weaker than those predicted by Romani et al. (1986), in different samples of pulsars. RISS and DISS are related through flux density, and therefore we might also expect DISS properties to be correlated with flux.

Despite these predictions and earlier work, we do not find any meaningful correlations between $\tau_{\rm d}$ and flux or $\tau_{\rm d}$ and DM in our data. Some also show anti-correlations, although this is likely just due to the small sample of delay measurements relative to $\Delta$DM measurements (e.g., PSRs J2317+1439 and J1614−2230).

While the evidence for linear correlations between the flux density variability and both $\tau_{\rm d}$ and DM is rather weak, with Pearson coefficients of $-0.18$ and $-0.35$, respectively, there was moderate evidence for general correlations, with Spearman coefficients of $-0.64$ and $-0.54$, respectively. These results are shown in the top and middle panels of Figure 2.9. This indicates that flux density variability decreases as $\tau_{\rm d}$ and DM increase, likely due to the higher number of scintles at larger DMs.

We expect that the flux density distributions in Figure 2.5 should be exponential at low DMs and small scattering delays and Gaussian at higher DMs and scattering delays (Scheuer, 1968; Hesse & Wielebinski, 1974) as we transition from small to large numbers of scintles. Indeed, most of the pulsars analyzed have low DMs and show exponential flux distributions. Pulsars with high DM and high scattering, such as PSRs J0340+4130, J0613–0200, and B1937+21, all exhibit Gaussian flux density distributions.

**Table 2.6:** Scattering Delay Trends & Correlations

| Pulsar | Freq | $\chi^2_r(\tau_{\rm d})$ | $\chi^2_r(S)$ | r($\tau_{\rm d}$, S) | $\overline{S}$(mJy) | r($\tau_{\rm d}$, DM) | $m_{\rm b;corrected}$ | $m_{\rm b;Kolmogorov}$ |
|---|---|---|---|---|---|---|---|---|
| J0340+4130 | 1500 | 10.1 | 0.1 | -0.2 ± 0.2 | 0.5 ± 0.00 | 0.7 ± 0.1 | — | 0.13 ± 0.01 |
| J0613−0200 | 820 | 21 | 0.1 | -0.5 ± 0.2 | 6.7 ± 0.00 | -0.1 ± 0.2 | — | 0.12 ± 0.00 |
| J0613−0200 | 1500 | 9.2 | 0.1 | 0.2 ± 0.1 | 1.9 ± 0.00 | -0.4 ± 0.1 | — | 0.13 ± 0.01 |
| J0636+5128 | 820 | 13.1 | 0.9 | -0.2 ± 0.2 | 1.9 ± 0.00 | 0.1 ± 0.2 | — | 0.12 ± 0.01 |
| J0636+5128 | 1500 | 7.7 | 0.2 | -0.4 ± 0.2 | 0.7 ± 0.00 | 0.3 ± 0.2 | — | 0.15 ± 0.01 |
| J0740+6620 | 820 | 0.7 | 10.5 | -0.1 ± 0.2 | 2.7 ± 0.00 | 0.2 ± 0.2 | — | 0.20 ± 0.02 |
| J1024−0719 | 1500 | 0.7 | 3.8 | -0.1 ± 0.4 | 1.7 ± 0.00 | -0.5 ± 0.3 | 0.30 | 0.19 ± 0.00 |
| J1125+7819 | 820 | 1.0 | 3.1 | -0.4 ± 0.2 | 4.1 ± 0.00 | 0.2 ± 0.2 | — | 0.20 ± 0.02 |
| J1125+7819 | 1500 | 0.7 | 1.1 | -0.3 ± 0.2 | 0.9 ± 0.00 | 0.2 ± 0.2 | — | 0.16 ± 0.01 |
| J1455−3330 | 820 | 0.5 | 3.2 | -0.1 ± 0.3 | 2.9 ± 0.00 | 0.1 ± 0.3 | — | 0.15 ± 0.01 |
| J1614−2230 | 1500 | 3.0 | 0.2 | 0.3 ± 0.1 | 1.1 ± 0.00 | -0.5 ± 0.2 | — | 0.14 ± 0.01 |
| J1640+2224 | 1500 | 1.0 | 1.1 | -0.4 ± 0.2 | 0.1 ± 0.00 | -0.03 ± 0.2 | — | 0.20 ± 0.02 |
| J1713+0747 | 1500 | 3.0 | 2.2 | -0.4 ± 0.1 | 4.7 ± 0.00 | 0.5 ± 0.1 | — | 0.18 ± 0.02 |
| J1738+0333 | 1500 | 2.8 | 2.2 | -0.3 ± 0.2 | 0.70 ± 0.00 | 0.1 ± 0.2 | 0.44 | 0.16 ± 0.01 |
| J1744−1134 | 820 | 0.3 | 1.7 | 0.1 ± 0.2 | 7.2 ± 0.00 | 0.1 ± 0.2 | 0.13 | 0.17 ± 0.01 |
| J1744−1134 | 1500 | 0.8 | 4.4 | -0.4 ± 0.2 | 2.6 ± 0.00 | -0.04 ± 0.19 | — | 0.19 ± 0.01 |
| J1853+1303 | 1500 | 8.5 | 0.5 | -0.4 ± 0.3 | 0.3 ± 0.00 | -0.3 ± 0.3 | 0.24 | 0.15 ± 0.01 |
| B1855+09 | 1500 | 13 | 0.4 | -0.3 ± 0.1 | 4.6 ± 0.00 | -0.06 ± 0.15 | — | 0.15±0.01 |
| J1909−3744 | 820 | 0.4 | 1.1 | -0.2 ± 0.2 | 4.5 ± 0.00 | -0.7 ± 0.2 | 0.18 | 0.14 ± 0.01 |
| J1909−3744 | 1500 | 1.0 | 3.0 | -0.1 ± 0.1 | 1.60 ± 0.00 | -0.4 ± 0.2 | — | 0.18 ± 0.01 |
| J1910+1256 | 1500 | 18 | 0.3 | 0.3 ± 0.2 | 0.6 ± 0.00 | -0.1 ± 0.2 | — | 0.12 ± 0.01 |
| J1918−0642 | 1500 | 1.7 | 0.8 | 0.02 ± 0.13 | 1.5 ± 0.00 | -0.2 ± 0.1 | — | 0.15 ± 0.01 |
| J1923+2515 | 1500 | 2.4 | 1.4 | -0.4 ± 0.3 | 0.4 ± 0.00 | 0.3 ± 0.3 | — | 0.17 ± 0.02 |
| B1937+21 | 1500 | 22 | 0.4 | 0.1 ± 0.1 | 12.3 ± 0.0 | -0.2 ± 0.2 | — | 0.11 ± 0.01 |
| J1944+0907 | 1500 | 11 | 1.2 | -0.2 ± 0.2 | 2.6 ± 0.00 | -0.1 ± 0.2 | — | 0.14 ± 0.02 |
| J2010−1323 | 1500 | 4.3 | 0.3 | -0.2 ± 0.1 | 0.7 ± 0.00 | 0.3 ± 0.1 | — | 0.14 ± 0.01 |
| J2145−0750 | 820 | 0.5 | 13.0 | 0.03 ± 0.24 | 23.2 ± 0.00 | -0.2 ± 0.3 | 0.16 | 0.16 ± 0.01 |

**Table 2.6:** Scattering Delay Trends & Correlations

| Pulsar | Freq | $\chi^2_r(\tau_{\rm d})$ | $\chi^2_r(S)$ | r($\tau_{\rm d}$, S) | $\overline{S}$(mJy) | r($\tau_{\rm d}$, DM) | $m_{\rm b;corrected}$ | $m_{\rm b;Kolmogorov}$ |
|---|---|---|---|---|---|---|---|---|
| J2145−0750 | 1500 | 0.2 | 5.0 | 0.3 ± 0.2 | 6.4 ± 0.00 | 0.2 ± 0.3 | — | 0.20 ± 0.01 |
| J2302+4442 | 820 | 0.1 | 0.2 | -0.2 ± 0.2 | 3.30 ± 0.00 | 0.3 ± 0.2 | — | 0.12 ± 0.00 |
| J2302+4442 | 1500 | 2.3 | 0.7 | -0.3 ± 0.2 | 1.3 ± 0.0 | -0.2 ± 0.2 | — | 0.14 ± 0.01 |
| J2317+1439 | 1500 | 0.4 | 5.0 | -0.1 ± 0.3 | 0.04 ± 0.00 | -0.9 ± 0.1 | 0.23 | 0.20 ± 0.01 |

**Table 2.6:** Reduced $\chi^2$ measurements, flux density and $\Delta$DM correlations, and measured and predicted modulation indices for all pulsars with at least 10 scattering delay measurements. We find that no strong correlations between scattering delays and flux density and scattering delays and $\Delta$DM. The unusually strong correlation coefficient seen in PSR J2317+1439 is likely not physical, as the scattering delay data is very sparsely sampled relative to $\Delta$DM estimates. A similar argument can be made for PSR J1614−2230 for correlations between flux and scattering delay. For most, if not all, of the pulsars shown above, the difference in sample rates between scattering delay and flux density and $\Delta$DM are too different to draw any meaningful conclusions on correlations. All correlations in this table use the Pearson correlation coefficient. We have not reported modulation indices in cases of negative $m^2_{\rm b;corrected}$.

Of the 24 pulsars we analyzed for scattering delay variability at 1500 MHz, seven showed no variation ($\chi^2_r \leq 1$), 11 had moderate variations ($1 < \chi^2_r \leq 10$), and six had significant variations ($\chi^2_r > 10$), indicating that scattering delays can be variable among MSPs and are highly dependent on the LOS to each pulsar. We also performed the same analysis on the nine pulsars with more than 10 $\tau_{\rm d}$ measurements at 820 MHz. Seven of the nine pulsars showed no variation, while the other two showed significant variations. Pulsars with at least 10 measurements at both frequencies generally had a similar degrees of variation at both frequencies, although it is unclear if this independence would hold if the observing frequencies were much farther apart. The exception to this was PSR J0613–0200, although the level of variability was still high at both frequencies.

Both the Pearson and Spearman coefficients also indicate greater scattering delay variability for pulsars with higher DMs (see the bottom of Figure 2.9). Note that all of the $\chi^2_r(\tau_{\rm d})$

values are slightly underestimated due to the finite scintle approximation we made in Equation 5.4 in Section 2.3.

Predicted modulation indices range from around $0.1 \lesssim m_{\mathrm{b;Kolmogorov}} \lesssim 0.2$, which is in agreement with most of our $m_{\mathrm{b;corrected}}$ values. As expected, those that disagree with theoretical predictions tend to be biased high, likely either due to excess refraction or an overly simplistic thin screen model.

### 2.5.2 Measuring Scaling Indices

We have determined the scaling of scattering delays with frequency by splitting each frequency band into subbands for four pulsars and by using an average delay measurement at each frequency for 15 pulsars.

Every scaling index we found using our multiband method was significantly shallower than $-4.4$, with a weighted average of $-2.6 \pm 0.1$. We find that our results agree with those of (Levin et al., 2016), who found an index weighted average of $-3.1 \pm 0.1$ for 10 pulsars over 26 epochs, with the vast majority of measured scaling indices being shallower than $-4.4$. This also agrees with the $-3.4 \pm 0.1$ weighted average we found for scaling indices determined using the subband method. In the two pulsars for which we were able to use both scaling analyses, the index measured using the multiband analysis was at least twice as shallow ($-2.4 \pm 0.3$ compared with $-0.7 \pm 0.5$ for PSR B1855+09 and $-2.6 \pm 1.1$ compared with $-1.3 \pm 0.4$ for PSR J2302+4442). This could indicate that the index of $-4.4$ used for stretching may not be properly scaling the scintles in each band, with the stretching index being too shallow in these two cases. However, this could partially be the result of the large discrepancy in the number of measurements used at 820 and 1500 MHz for the multiband analysis, as is discussed below.

There are several reasons why these indices may not agree with the $-4.4$ expected for a Kolmogorov medium. The thin screen approximation which is commonly used assumes an infinite scattering screen. However, many of the pulsars have lower DMs, which means they could be subject to finite or truncated scattering screens (Cordes & Lazio, 2001). Scaling indices

shallower than $-4.4$ (as low as $-4.0$) have been found to be better fits to the data for assuming the existence of these finite screens for a given inner scale cutoff (Rickett et al., 2009).

While using a wider frequency range for this analysis is an improvement over Levin et al. (2016), they were able to measure scaling indices for individual days, whereas, as mentioned earlier, we rarely, if ever, had days in which we had detectable measurements for two frequencies in a given epoch.

We may also be biased by the ratio of our measurable observations from both frequencies. For five of the 15 pulsars we analyzed, only one to three measurements at 820 MHz were obtained, and so these fits are much more constrained at higher frequencies. We were able to make at least six measurements for the other pulsars at both frequencies, although for two of them there are more than twice as many 820 MHz measurements. As mentioned earlier, for PSR B1855+09, for which we have many more measurements at 1500 MHz, the subband method returns a much steeper scaling index at each frequency than the multiband method. This implies that similar effects may impact the measurements for other pulsars, for which we were unable to apply the subband measurements.

Finally, as we discussed in Section 2.3.1 and the beginning of Section 2.5, our limited bandwidths and frequency resolution may cause underestimations on high scintillation bandwidths and overestimations on low ones. Because scintillation bandwidths are smaller at lower frequencies, there will be more underestimations of scattering delay at lower frequencies and more overestimations at higher frequencies. With wider bandwidths and better resolution, our scaling indices would likely be closer to $-4.4$.

The trend of shallow scaling indices has been found in multiple studies in addition to this paper and Levin et al. (2016). Bansal et al. (2019) performed observations on seven pulsars and found five of them to have shallower indices than $-4.4$. While the other two were close to $-4.4$ when considering their weighted averages, there were deviations on an epoch-to-epoch basis. Bhat et al. (2004) observed several pulsars at at least two frequencies and determined scaling indices with a pulse broadening function that assumed a thin screen between the Earth and the pulsars. While a few of their pulsars were consistent with a $-4.4$ scaling index, the

average index for their sample was $-3.12 \pm 0.13$. Using a pulse broadening function that assumed scattering material uniformly distributed along the LOS, they found an average index of $3.83 \pm 0.19$. The latter was in better agreement with the global fit to their data, which resulted in an index of $-3.86 \pm 0.16$, which they found via a parabolic fit of $\tau_{\rm d}$ vs DM using a variation of the model from Cordes & Lazio (2003). They determined that such trends could still be expected for a Kolmogorov medium if the spectrum of turbulence had an inner cutoff between around 300–800 km. Other studies show higher DM pulsars seem to exhibit indices that are shallower than expected for a Kolmogorov medium (Löhmer et al., 2002) (although this can be explained by a truncation of the scattering region), while lower DM pulsars tend to have indices much more in line with a Kolmogorov medium (Cordes et al., 1985). New techniques such as cyclic spectroscopy will allow for more accurate single-epoch scaling index measurements than are currently obtainable by ACF analyses (Demorest et al., 2012).

A benefit of the subband method is that we can look for variability in the scaling index of a given pulsar over time, which was not possible with our multiband method due to limited epochs having frequency-resolvable, same-day measurements. As briefly mentioned in Section 2.4.2, and clearly visible by eye in both Figures 2.10 and 2.11, for pulsars with fully resolved scintles there appears to be a low degree of variation in the scaling index from epoch to epoch, which is further evidenced by both pulsars having $\chi^2_r \leq 1.0$. This consistency implies that scaling indices are intrinsically stable, as expected. Conversely, for a pulsar like PSR B1937+21, which likely has many epochs with unresolved scintles, we found a much larger degree of variation, with $\chi^2_r = 7.7$. However, it is likely this variation would decrease significantly once sufficient resolution was achieved.

We have also computed Pearson correlation coefficients between average scaling index and $\overline{\Delta\nu_{\rm d}}$ and average scaling index and DM for both the subband and multiband methods. We find no current evidence of correlations for any of these quantities for either approach.

### 2.5.3 Transverse Velocity Measurements

Transverse velocity measurements listed in Table 2.5 are shown in Figure 2.8. We find, under the assumption of an equidistant scattering screen between us and a given pulsar, poor agreement between velocities derived from both methods, as indicated by the low correlation coefficient. As mentioned earlier, we are likely biased low on most of our average scintillation timescales due to our short observation lengths, and as a result more of our $V_{\rm ISS}$ values may be upper limits than our averages would indicate. The exception to this is PSR B1937+21, for which we are confident in our measurement of its scintillation timescale, as all of its epochs had scintles that were clearly resolved in time. However, as mentioned before, we are likely overestimating its scintillation bandwidth, which will also lead to an overestimation of its $V_{\rm ISS}$.

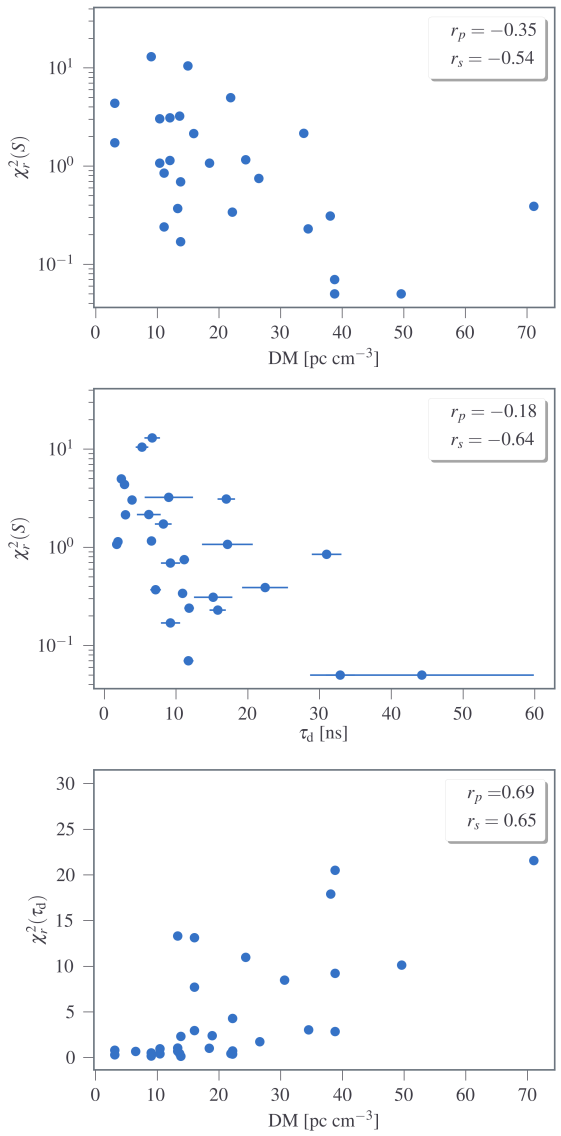


**Figure 2.9:** Top: A semi−log comparison of a pulsar's average scattering delay and the $\chi^2_r$ variability in its flux density. The Spearman correlation coefficient shows moderate evidence of an inverse correlation, indicating flux densities are less variable for more distant pulsars. Middle: A semi−log comparison of a pulsar's DM and the $\chi^2_r$ variability in its flux density. The Spearman correlation coefficient shows moderate evidence an inverse correlation, indicating flux densities are less variable for more highly scattered pulsars. We are able to examine DM variations at scales of $10^{-4}$ pc cm$^{-3}$ using DMX, and so the errors on DM in this plot are too small to see. Bottom: The DM vs the $\chi^2_r$ variability in the scattering delay. The Pearson correlation coefficient shows moderate evidence for linear correlations, indicating that pulsars at higher DMs ($\gtrsim$ 20 pc cm$^{-3}$) experience greater variability in their scattering delays, and the Spearman correlation coefficient also shows moderate evidence of general increasing correlations. We are able to examine DM variations at scales of $10^{-4}$ pc cm$^{-3}$ using DMX, and so the errors on DM in this plot are too small to see.

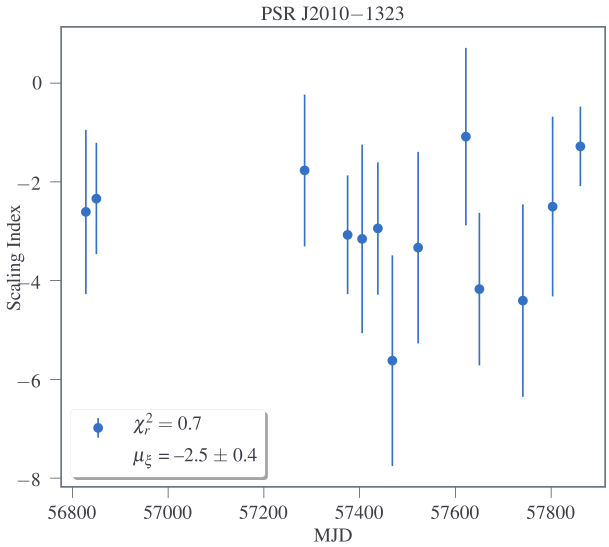


**Figure 2.10:** Measured scaling indices from individual epochs of PSR J2010–1323. The level of variation from epoch to epoch is low and the weighted average scaling index is much shallower than −4.4.

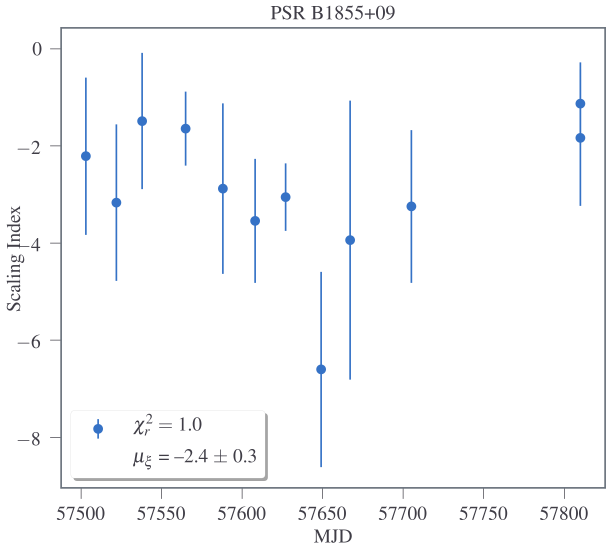


**Figure 2.11:** Measured scaling indices from individual epochs of PSR B1855+09. The level of variation from epoch to epoch is low and the weighted average scaling index is much shallower than −4.4.

Additionally, the discrepancy between $V_{\rm ISS}$ and $V_{\rm pm}$ also demonstrates that knowledge of the scattering screen distance is crucial to accurately determine transverse velocities in this manner, provided other assumptions about the geometry and electron density of the ISM are correct. Many of the $V_{\rm ISS}$ upper limits are consistent with their corresponding $V_{\rm pm}$ values.

We used weighted averages of the scintillation parameters to estimate $V_{\rm ISS}$. However, even though scintillation variability seen on shorter timescales in many pulsars is comparatively small (see Figure 2.5 for many examples of this), these changes can have drastic effects on the calculated transverse velocity. For example, McLaughlin et al. (2002) measured scintillation parameters for the pulsar PSR J1740+1000 at seven epochs that spanned over 700 days and found the changes in scintillation behavior led in the most extreme cases to factor-of-two variations in transverse velocity estimations. While some of this fluctuation was due to measurement uncertainties, they also partially attributed it to ISM effects, particularly modulations in RISS. There are also quite a few pulsars in Figure 2.5 where we can see at least factor-of-two variations in the scattering delay, which would either imply significant changes in $V_{\rm ISS}$ or significant changes in the screen location from epoch to epoch. As a result, the average of $V_{\rm ISS}$ is a better measure of velocity than the measurement at a single epoch. We do not expect $V_{\rm ISS}$ and $V_{\rm pm}$ to fully agree without accounting for the screen distance. However, Reardon et al. (2020b) were able to use 16 years of scintillation measurements for PSR J0437–4715 to determine orbital parameters with higher precision than through timing, indicating that similar levels of precision and accuracy may be obtainable for scintillation-derived transverse velocities. Among pulsars for which both $V_{\rm pm}$ and $V_{\rm ISS}$ measurements were possible, proper motion provided higher precision for the majority of the pulsars. However, there are still benefits to using $V_{\rm ISS}$, as discrepancies between $V_{\rm ISS}$ and $V_{\rm pm}$ could imply a significant motion of the ISM along a LOS or whether a uniform medium or thin screen structure is more accurate for a LOS (Reardon et al., 2019).

Calculated scattering screen fractional distances are also shown in Table 2.5, with values greater than one indicating a screen closer to the Earth, and less than one indicating a screen closer to the pulsar. Of the pulsars with measurements that are not upper limits, two pulsars at 820 MHz and three at 1500 MHz require screens that are closer to Earth, three pulsars at 820

MHz require screens that are equidistant, and one pulsar at 1500 MHz and one at 820 MHz had a screen closer to the pulsar. If we look at pulsars with upper limits, two pulsars at 820 MHz and three pulsars at 1500 MHz require a screen closer to the pulsar, while it could be argued that four of the pulsars at 1500 MHz and one pulsar at 820 MHz likely have screens that are equidistant.

We assume that velocities from the ISM provide negligible contributions to a given pulsar's transverse velocity. Additionally, contributions to the ISM velocity from the transverse component of differential Galactic rotation (DGR), even if the latter's velocity is large, can be ignored for nearby pulsars for which the ISM will co-rotate with the LOS. As most of the pulsars we analyzed are no more than 1.5 kpc away, and only one is more than two kpc away, we are unable to probe the regime where contributions from Galactic rotation become significant and whether our assumptions about a uniform Kolmogorov medium break down at these distances.

### 2.5.4 Scaling of Scattering Delay with DM

The most commonly used model for mapping electron densities in the Milky Way is NE2001 (Cordes & Lazio, 2002). This model uses a pulsar's DM and position in the Galaxy to estimate its distance, as well as scintillation parameters such as scintillation bandwidth and timescale. We have plotted the predicted scattering delay vs. the measured weighted means for all pulsars in Figure 2.12. As indicated by the high correlation coefficient, we find reasonably strong agreement between our measured delays and those predicted by NE2001. Improved frequency resolution and/or wider observing bandwidths are necessary in order to probe the relationship between NE2001 predictions and our measurements at high and low delays. Other models, such as those of Bhat et al. (2004), Yao et al. (2017), and Krishnakumar et al. (2015) use an empirical fit to scattering delays versus DM for prediction.

In Figure 2.13, we plot average scattering delay as a function of DM. Bhat et al. (2004) surveyed over 100 pulsars and fit a parabolic relation of the form

$$\log \tau_{\mathrm{d},\mu\mathrm{s}} = a + b(\log \mathrm{DM}) + c(\log \mathrm{DM})^2 - \alpha \log \nu_{\mathrm{GHz}}, \tag{2.13}$$

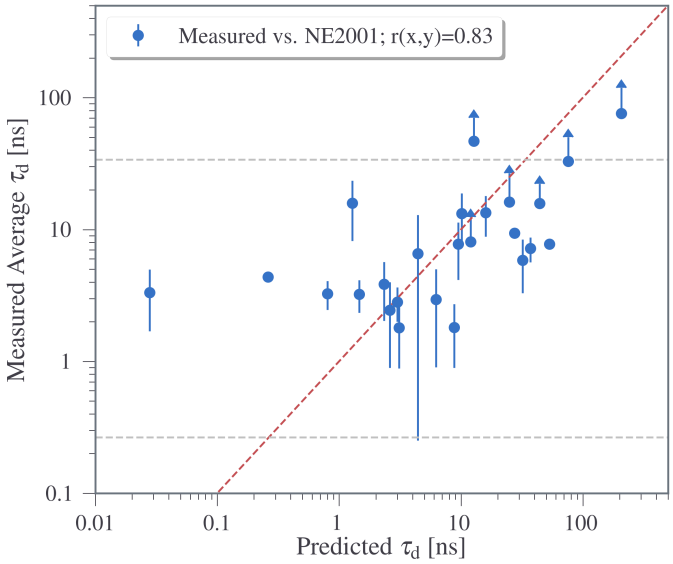


**Figure 2.12:** Average scattering delay measured at 1500 MHz from this paper compared with the predicted delays by the NE2001 model. The dotted red line indicates a trend with a Pearson correlation coefficient of one, the gray dotted lines indicate the largest and smallest scattering delays we can resolve, corresponding with three channel widths and our effective bandwidth at 1500 MHz, respectively, and the points with arrows indicate delay averages that are lower limits. Generally, values above 0.7−0.8 indicate a fairly strong correlation, depending on how precisely it is expected a given model will agree with data.

where $a$, $b$, and $c$ are dimensionless scaling coefficients and $\alpha$ is the scaling index of the medium. In their fit, they found $a$, $b$, and $c$ to be 6.46, 0.154, and 1.07, respectively, with a resulting scaling index of $\alpha = 3.86 \pm 0.16$. While this index is slightly shallower than the fiducial Kolmogorov index of 4.4, they provide a number of detailed explanations for this discrepancy, including a finite wavenumber cutoff based on the inner scale for a Kolmogorov medium and abrupt changes in the medium transverse to the LOS.

Krishnakumar et al. (2015) used the relation from Ramachandran et al. (1997), fitting an exponential equation of the form

$$\tau_{\mathrm{d,s}} = a\mathrm{DM}^{\gamma}(1 + b\mathrm{DM}^{\zeta})\nu^{-\alpha}, \tag{2.14}$$

where $a$, $b$, $\gamma$, and $\zeta$ are dimensionless coefficients and $\alpha$ is again the scaling index of the medium. They set $\gamma = 2.2$, as expected for a Kolmogorov medium.

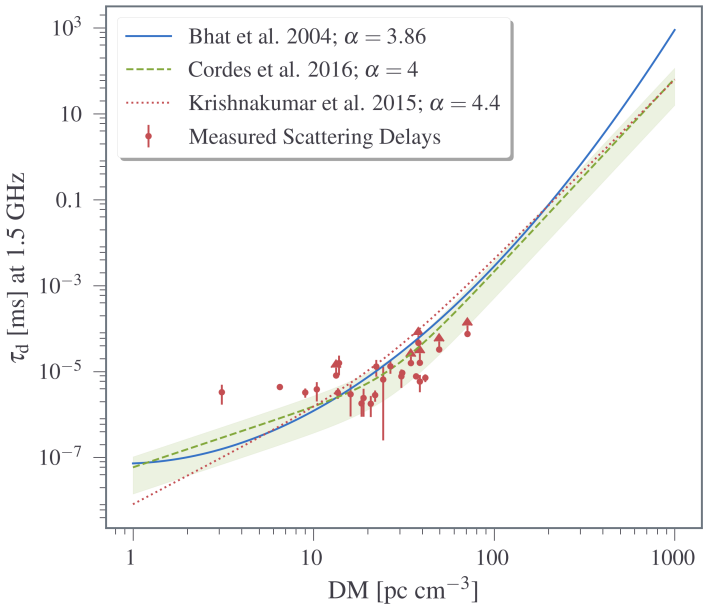


**Figure 2.13:** Comparison between measured scattering delays at 1500 MHz and fits made by Bhat et al. (2004), Cordes et al. (2016), and Krishnakumar et al. (2015), along with the $1\sigma$ errors from Cordes et al. (2016), shaded in green. The scales shown in the plot were chosen based on the spread of data over which the fits were initially determined.

Krishnakumar et al. (2015) then set $\alpha = 4.4$ and fit for $a$, $b$, and $\zeta$ using scattering data from 358 pulsars, finding values of $4.11\times10^{-11}$, $1.94\times10^{-3}$, and 2.0, respectively. However, unlike our approach, in which we set $C_1 = 1$, scattering delays used in this fit were calculated with $C_1 = 1.16$. It should be noted that since these three fits are not direction dependent, they can only serve as first-order approximations for how DM correlates with $\tau_{\mathrm{d}}$ within our galaxy.

Cordes et al. (2016) set $\alpha = 4$ and fit for all remaining parameters using 531 lines of sight from pulsars, magnetars, and FRBs and found $a = 2.98 \times 10^{-7}$, $b = 3.55 \times 10^{-5}$, $\gamma = 1.4$, and $\zeta = 3.1$.

We compared these three fits with our measured scattering delays in Figure 2.13, with the $1\sigma$ errors from Cordes et al. (2016). The scales shown were chosen based on the scales over which the initial models were fit. The delays we measure are comparable to those predicted by all of these models, but we do not have data over a wide enough DM range to discriminate among them. Also note that the delays we measure for the lowest DM pulsars are much higher than model predictions, indicating the LOS dependence of scattering at these low DMs.

## 2.6 Conclusions

We used dynamic spectra made from observations with the GUPPI and PUPPI spectrometers to obtain scintillation parameters of pulsars in the NANOGrav 12.5-year data set.

We looked for correlations between scattering delays and both DM and flux density as a function of time. We did not find any significant correlations, and any instances of high correlation could be attributed to the scale of our scattering delays and their limited sample size. Additional contributions to flux density may also be masking existing correlations with DISS, and a lack of change in the electron density structure of the ISM along our LOSs may be further limiting correlations with DMX.

We then examined the variability of our scattering delay measurements via a reduced $\chi^2$ analysis on 24 of the pulsars. We also found that, for most pulsars where at least 10 measurements of $\tau_{\rm d}$ were available at both 820 and 1500 MHz, the degree of variation was virtually the same at both frequencies, meaning that scattering variation might be independent of observing frequency.

We measured scaling indices for 17 pulsars and found that all of the pulsars exhibited a shallower than $\nu^{-4.4}$ scaling. We concluded that, although the ISM along these LOSs might

follow shallower scaling laws than expected, biases introduced by uneven sampling of our two frequencies and resolution issues provide plausible explanations for this.

We were able to use scintillation parameters to estimate transverse velocities. We also calculated the location of the scattering screen, assuming that $V_{\rm ISS}$ and $V_{\rm pm}$ are equal. Much of the disagreement is likely the result of our scintillation timescale averages being biased low as the result of our short observation length.

We were also able to determine scattering screen fractional distances using our measured scintillation parameters and $V_{\rm pm}$ values.

Finally, we examined how scattering delays compare with electron density models as well as scale with DM and plotted our results against empirical fits of scattering delay vs DM (Cordes et al., 2016; Bhat et al., 2004; Krishnakumar et al., 2015). We find that, on the DM scales these fits consider, both the spread of and trends in our data agree with all three fits above a DM of around 10 pc cm $^{-3}$, below which the models begin to follow a steeper trend than our measurements. We also found our results largely agree with predictions made by NE2001 for pulsars where scintles were resolvable.

As we continue to observe PTAs with higher precision and get closer to gravitational wave detection, additional sources of TOA residual uncertainty will become significant enough that they cannot be ignored by our timing models. We have already reached that stage with scattering delays in some pulsars, as we have shown that they exhibit average delays comparable in magnitude to the 10 ns precision believed to be necessary for gravitational wave detection. Additionally, pulsars such as PSR B1937+21 already have scattering delays comparable to or greater than their median TOA uncertainty at certain frequencies (Arzoumanian et al., 2018). Many more pulsars are on track to reach these levels of precision in TOA uncertainty within the next few years, at which point it will be increasingly detrimental to ignore effects from scattering. It is crucial to incorporate methods to mitigate these delays in our timing pipelines as soon as possible.

Our analysis illustrates the need for finer frequency resolution in our standard timing observations. New techniques like cyclic spectroscopy allow for the determination of ISM-related

delays and unscattered pulse profiles from single observations, making it much more efficient to mitigate these delays than the current method of ACF fitting (Demorest, 2011; Palliyaguru et al., 2015). This technique, which will allow us to obtain much better scattering estimations for highly scattered and high-S/N pulsars (Dolch et al., 2020) has already been used with fine frequency resolutions (Archibald et al., 2014). Efforts are ongoing to implement real-time cyclic spectroscopy pipelines into NANOGrav's existing observing pipelines, with the goal of removing scattering effects before any further timing analysis has taken place.

*Acknowledgements*: The NANOGrav project receives support from National Science Foundation (NSF) Physics Frontier Center award number 1430284. TD and MTL acknowledge NSF AAG award number 2009468. NANOGrav research at UBC is supported by an NSERC Discovery Grant and Discovery Accelerator Supplement and by the Canadian Institute for Advanced Research. Data for this project were collected using the facilities of the Green Bank Observatory and the Arecibo Observatory. The Green Bank Observatory is a facility of the National Science Foundation operated under cooperative agreement by Associated Universities, Inc. The Arecibo Observatory is a facility of the National Science Foundation operated under cooperative agreement by the University of Central Florida in alliance with Yang Enterprises, Inc. and Universidad Metropolitana. The National Radio Astronomy Observatory is a facility of the National Science Foundation operated under cooperative agreement by Associated Universities, Inc.

Part of this research was carried out at the Jet Propulsion Laboratory, California Institute of Technology, under a contract with the National Aeronautics and Space Administration.

The majority of data processing for this work took place on the Bowser computing cluster at West Virginia University.

We would like to thank Dick Manchester for a useful discussion on the relations between scattering delay and DM. We would also like to thank Lina Levin for providing most of the initial groundwork for this paper and for the scripts we used to process and analyze dynamic spectra.

*Author contributions*: JET undertook all of the data analysis, wrote most of the pipelines and supplementary scripts, and wrote the paper. MAM provided mentorship and suggestions regarding the analysis and writing of the paper. JMC provided valuable suggestions on data interpretation and analyses to run, as well as discussions on ISM structure and behavior. BJS provided useful discussion on transverse velocities, scintillation behavior and analysis techniques, and software development. MTL provided useful discussion on software development and suggesting the inclusion of certain analyses. DRS provided important discussion regarding underestimations of scattering delays in our data. SC and TJWL provided useful discussion on the structure of the ISM and the nature of scattering delays. ZA, HB, PRB, HTC, PBD, MED, TD, JAE, RDF, ECF, EF, NGD, PAG, DCG, MLJ, MTL, DRL, RSL, MAM, CN, DJN, TTP, SMR, RS, IHS, KS, JKS, and WWZ developed the 12.5-year data set.

*Software*: PSRCHIVE Hotan et al. (2004), TEMPO Hobbs et al. (2006), SCIPY Virtanen et al. (2020), NUMPY van der Walt et al. (2011), and MATPLOTLIB Hunter (2007).

# Chapter 3. A Simultaneous Dual-Frequency Scintillation Arc Survey of Six Bright Canonical Pulsars Using the Upgraded Giant Metrewave Radio Telescope

## 3.1 Introduction

The scintillation of pulsar emission occurs as the result its propagation through non-uniform distributions of free electrons in the ionized interstellar medium (ISM). This interaction results in frequency-dependent and time-evolving variations in the flux density of the pulsar signal as measured at a detector. When these variations are examined across observing frequency and time in so-called dynamic spectra, representations of the change in the pulsar signal's intensity across frequency and time, for a given observation, they can provide valuable insight into the structure of these electron density variations along our line of sight (LOS) to a given pulsar. Information can be gained about the ISM structure along the LOS by examining the parabolic arcs, known as scintillation arcs, that can emerge by examining the power spectrum of the dynamic spectrum, generally known as the secondary spectrum (Stinebring et al., 2001c). Successful analysis requires sufficient resolution in time and frequency of the scintles, or bright patches in the dynamic spectrum, due to constructive interference between different ray paths through the IISM. Refractive shifts due to, e.g., wedge-like plasma structures cause scintillation drift patterns that cause asymmetries in the scintillation arc intensity distribution and an offset of the parabola origin (Cordes et al., 2006b). Some current hypotheses on the physical origins

Submitted to ApJ as J. E. Turner et al. 2023

of these arcs postulate that they originate from compressed plasma along the boundaries of 50−100 pc size bubbles in the ISM (Stinebring et al., 2022).

Scintillation arc studies require high S/N to obtain quality data. As a consequence, large surveys of scintillation arcs have typically focused on canonical (i.e., non-recycled) pulsars with high flux densities and low dispersion measures (Stinebring et al., 2022) or observations at low observing frequencies where pulsars are typically brightest (Wu et al., 2022). Some recent large surveys have used newer, more sensitive instruments and observing configurations, in some cases detecting scintillation arcs in over 100 pulsars across a wide range of dispersion measures (Main et al., 2023a) and in others performing large scintillation arc surveys using generally lower flux density millisecond pulsars (Main et al., 2023b). Pulsar scintillometry, which uses observations of scintillation arcs over many years, has allowed for high precision estimations on the localization of scattering screens along a given LOS (Sprenger et al., 2022; McKee et al., 2022). Thanks to long term campaigns to detect low frequency gravitational waves using arrays of millisecond pulsars (Agazie et al., 2023c; Antoniadis et al., 2023; Zic et al., 2023; Tarafdar et al., 2022), measurements of annual arc variations via high precision scintillometry have also recently been accomplished using a few millisecond pulsars (Main et al., 2020, Reardon et al., 2020., Mall et al., 2022).

Traditional measurements of scintillation arcs have typically been limited to either one observing band over all epochs (e.g., Trang & Rickett (2007)), or alternated between observing bands from epoch to epoch (e.g., Stinebring et al. (2019)). While generally sufficient for most analyses, this band limit results in a bottleneck for examining the evolution of various frequency-dependent effects over shorter timescales, including scintillation arc curvature, structures within individual arcs, and asymmetries in both arc brightness and power as a function of differential time delay. By making use of the subarray capabilities of the upgraded Giant Metrewave Radio Telescope (uGMRT) (Gupta et al., 2017), we can effectively create an ultra wideband receiver by setting multiple groups of dishes to simultaneously observe at different frequencies. This work is primarily data-focused and aims to highlight the results of some multi-frequency analyses performed on a small survey of six strong canonical pulsars **, all known to exhibit**

**scintillation arcs in at least one of the frequency bands,** using this approach. In Section 3.2 we discuss the data taken as part of our survey. Section 3.3 describes the analyses performed and the physical parameters extracted. Section 3.4 details the results of these analyses. Finally, Section 3.5 summarizes our results and discusses possible next steps.

## 3.2 Data

Our data were taken across eight epochs spanning MJD 58987−59497 using 22 dishes split into subarrays for simultaneous multi-frequency observations at uGMRT's Band 3 and Band 4, centered at 400 MHz and 650 MHz, respectively, each with 200 MHz of bandwidth. This simultaneous low-frequency accessibility is comparable to instruments like CHIME that can observe continuously between 400−800 MHz (Collaboration et al., 2022) and better than instruments such as the Green Bank Telescope, which, while having a wide range of low frequency coverage, can only observe below 1 GHz with at most 240 MHz of bandwidth at frequencies close to 1 GHz and less than 200 MHz of bandwidth in lower frequency ranges (Staff, 2017). Observations were also made at Band 5 centered at 1360 MHz, although due to a combination of RFI and low signal-to-noise (S/N) no scintles were detectable in the dynamic spectra. The observing bands were split into 4096 (49 kHz wide) frequency channels and observed with 10 second subintegrations. These data were flux calibrated using observations of either 3C147 or 3C286 taken at the beginning of every observing session, and every pulsar was phase calibrated with a nearby source for five minutes once every 40 minutes of observing time on the pulsar. Two to three pulsars were observed at each epoch for 40 minutes, except for MJD 59497, where three pulsars were observed for 155 minutes each. As a result of the phase calibration, each of those observations comprised three 40 minute scans plus an additional 20 minute scan. A summary of the observations made can be found in Table 3.1.

**Table 3.1:** Pulsars Observed

| Pulsar | $N_{\rm obs}$ | Frequencies |
|---|---|---|

| J2000 | Epoch | B1950 | Epoch | | (MHz) |
|---|---|---|---|---|---|
| J0630−2834 | | B0628−28 | | 1 | 300−500, 550−750 |
| J1136+1551 | | B1133+16 | | 4 | 300−500, 550−750 |
| J1509+5531 | | B1508+55 | | 4 | 550−750 |
| J1645−0317 | | B1642−03 | | 1 | 550−750 |
| J1932+1059 | | B1929+10 | | 3 | 300−500, 550−750 |
| J2048−1616 | | B2045−16 | | 1 | 300−500, 550−750 |

**Table 3.1:** Summary of pulsar observations.

The raw data were reduced using the publically available pipeline for uGMRT data reduction, PINTA (Susobhanan et al., 2021). Here, first radio frequency interference (RFI) was excised from the raw data using RFIclean (Maan et al., 2021). Then, the data were folded with the full frequency resolution using a pulsar ephemeris obtained from the ATNF pulsar catalog (Manchester et al., 2005a) to obtain partially folded sub-banded profiles in PSRFITS format (Hotan et al., 2004). All the subsequent analysis used these reduced PSRFITS files.

## 3.3 Analysis

All observations were processed to extract their dynamic spectra by calculating the intensity, $S$, of the pulsar's signal at each observing frequency, $\nu$, and time, $t$, via

$$S(\nu, t) = \frac{P_{\rm on}(\nu, t) - P_{\rm off}(\nu, t)}{P_{\rm bandpass}(\nu, t)}, \tag{3.1}$$

where $P_{\rm bandpass}$ is the total power of the observation as a function of observing frequency and time, and $P_{\rm on}$ and $P_{\rm off}$ are the power in all on- and off-pulse components, respectively, as a function of frequency and time. In this process, we smoothed from 512 pulse profile bins to 64, and defined the on-pulse region as the bins in the summed profile with an intensity >5%

of the maximum in a continuous window. Each dynamic spectrum was then broken up into four 50 MHz spectra to allow for more in-depth frequency-dependent analyses and manually zapped of interference by examining dynamic spectra data arrays and removing pixels that were brighter than the brightest scintle maxima. Secondary spectra were then created by taking the squared modulus of the two-dimensional Fourier transform (i.e., the power spectrum) of the corresponding 50 MHz dynamic spectrum and displaying it logarithmically (dB). While this is certainly one of the more commonly used methods for obtaining the secondary spectrum, alternative approaches have recently been explored (Osłowski & Walker, 2023).

To determine the arc curvature in the primary (brightest) scintillation arc on both the positive and negative side of each secondary spectrum's fringe frequency axis, we followed the approach described in Stinebring et al. (2022) in which we divided each secondary spectrum along the center of its fringe frequency axis and further divided the secondary spectrum into horizontal slices up the delay axis until we reached the approximate end of a given arm. Searching only in the region of the spectrum surrounding a given arc, we determined the maximum in each delay slice and fit the resulting trends using $f_\nu = \eta f_t^2$ fits, where $f_\nu$ is the differential time delay, $\eta$ is the arc curvature, and $f_t$ is the fringe frequency.

Normalized secondary spectrum power profiles were acquired using the SCINTOOLS package (Reardon et al., 2020), which creates these profiles from normalized secondary spectra, which are secondary spectra that have been manipulated such that their scintillation arcs are fully vertical. This package utilizes a Hough transform approach for fitting arcs, in which a range of possible $\eta$ values is explored by calculating the summed power along each corresponding fit, with the resulting curvature of the observation being the one with the greatest summed power.

We also determined scintillation parameters by fitting Gaussians and Loren- tzians to frequency slices of a given observations's two-dimensional autocorrelation function (ACF) to determine their scintillation bandwidth, $\Delta\nu_\mathrm{d}$, defined as the half-width at half-maximum (HWHM) of the frequency ACF at lag 0, Gaussians to the time slices of the same ACF to determine their scintillation timescale, $\Delta t_\mathrm{d}$, defined as the half-width at $e^{-1}$ of the time ACF lag 0, and scintillation drift rate, $\mathrm{d}\nu/\mathrm{d}t$, defined as the rotation of the 2D Gaussian fit to the 2D ACF

in the plane of the frequency and time lags. The decision to measure scintillation bandwidths using both Gaussian and Lorentzian fits serves as a compromise between literature consistency and mathematical rigor; virtually all studies that use an ACF analysis to determine scintillation parameters do so using Gaussian fits. However, given that the ISM's impulse response function, a time domain function, is characterized by a one-sided decaying exponential, it makes more mathematical sense to fit the corresponding frequency domain ACF using a Lorentzian, as the two functions are a Fourier pair.

These scintillation parameter fits were accomplished using code that was heavily based on PYPULSE (Lam, 2017), but modified to allow for more user flexibility regarding data ranges over which fits took place, as well as the inclusion of algorithms that allowed for Lorentzian fits.

## 3.4 Results & Discussion

### 3.4.1 Scintillation Arc Curvature Scaling Behavior

As mentioned earlier, Hill et al. (2003b) demonstrated through both theoretical and observational means that the arc curvature $\eta$ should follow a $\nu^{-2}$ dependence, following the same power law as the angular deflection of the pulsar signal. While over 2 GHz of bandwidth was used in those observations (10-12.5 MHz of bandwidth centered at 430 MHz and either 50 or 100 MHz of bandwidth centered at 1175 MHz, 1400 MHz, and 2250 MHz), the frequency coverage was discontinuous and all $\eta$ measurements used in their corresponding fits were from different epochs. Generally the latter point should not be an issue as long as the observations were taken within a period shorter than the pulsar's refractive timescale and the measured effective velocity has changed minimally. Indeed, for the data used in their fits, their measured arc curvatures at a given frequency did not vary significantly on day or week timescales, making them suitable for this type of analysis. However, the ideal situation would be to obtain many measurements at many frequencies during the same observation, preferably at the same time for optimal consistency. With our high resolution and sufficient observing time, we have the ability

to make up to eight concurrent arc measurements over 450 MHz of bandwidth at low frequency and can consequentially provide a more definitive examination of the theory. Additionally, since all of our measurements for a given scaling fit are taken on the same day, they all have the same effective velocity.

Following the methodology of Hill et al. (2003b), for a scaling index $\alpha$, we performed a weighted linear least-squares fit of the form

$$\log_{10} \eta = \alpha \log_{10} \nu + \beta \tag{3.2}$$

on the curvatures for each pulsar with at least three measurements at a given MJD, weighted by the squared inverses of the arc curvature uncertainties. Example fits can be seen in Figure 3.1, with all measured indices listed in Table 5.2. We find that, overall, our scaling indices are consistent with a theoretical index of $-2$, with PSRs J1136+1551 and J1932+1059 being especially consistent. Interestingly, a weighted average of all curvature fits across all pulsars shows that our left arm fits are overall more consistent with an index of $-2$ than our right arms, with a weighted average of $-1.99 \pm 0.03$ across all left arm fits compared with $-1.69 \pm 0.02$ across all right arm fits, indicating that refraction may play a role in how closely arc curvature scales as expected with frequency. However, we strongly emphasize that there is significant variation in curvature indices across pulsars and epochs, and that this is only an average.

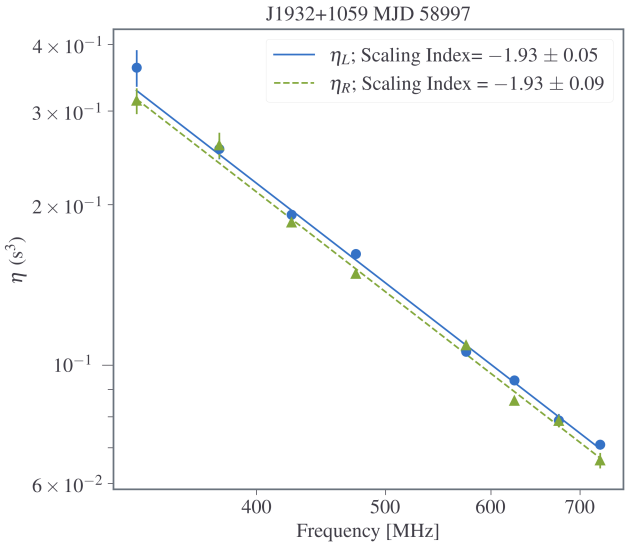


**(a)** Arc curvature scaling index fit for both left (solid blue with dots) and right (dashed green with triangles) for PSR J1932+1059 on MJD 58997

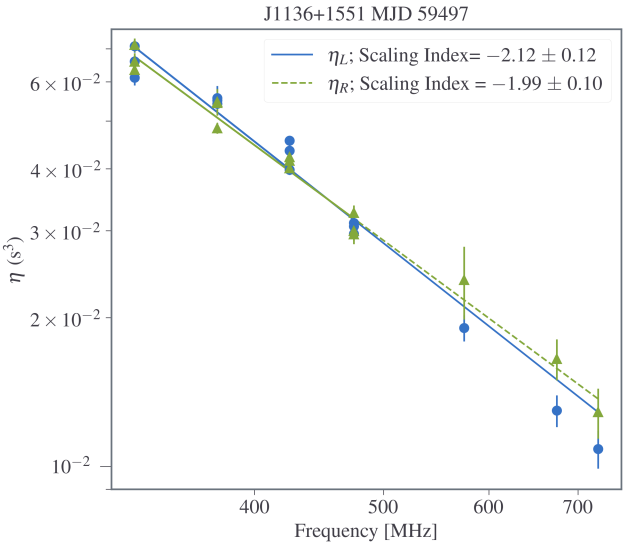


**(b)** Arc curvature scaling index fit both left (solid blue with dots) and right (dashed green with triangles) for PSR J1136+1551 on MJD 58997. The inclusion of multiple points at certain frequencies is the result of this epoch containing a 155 minute observation instead of the 40 minutes of the other observations, and so a new $\eta$ was measured after every 40 minutes.

**Figure 3.1:** Example fits for the arc curvature scaling index

**Table 3.2:** Fitted Pulsar Scintillation Arc Curvature Scaling Indices

| Pulsar | MJD | Scaling Index Left Arc | Scaling Index Error Left Arc | $N_\eta$ | Scaling Index Right Arc | Scaling Index Error Right Arc | $N_\eta$ |
|---|---|---|---|---|---|---|---|
| J0630−2834 | 58987 | — | — | — | −2.48 | 0.31 | 8 |
| J1136+1551 | 58987 | −1.79 | 0.11 | 7 | −1.89 | 0.12 | 7 |
| J1136+1551 | 58991 | −1.65 | 0.12 | 8 | −1.94 | 0.08 | 8 |
| J1136+1551 | 59115 | −1.36 | 0.13 | 8 | −1.52 | 0.15 | 8 |
| J1136+1551 | 59497 | −2.12 | 0.12 | 15 | −1.99 | 0.10 | 15 |
| J1509+5531 | 58987 | −1.49 | 0.83 | 3 | −1.34 | 0.55 | 3 |
| J1509+5531 | 59064 | −1.62 | 0.26 | 4 | −1.41 | 0.22 | 4 |
| J1509+5531 | 59115 | −0.93 | 0.21 | 4 | −2.31 | 0.18 | 4 |
| J1509+5531 | 59497 | −2.01 | 0.87 | 9 | −1.34 | 0.21 | 9 |
| J1645−0317 | 59074 | −2.09 | 0.26 | 4 | — | — | — |
| J1932+1059 | 58997 | −1.93 | 0.05 | 8 | −1.93 | 0.09 | 8 |
| J1932+1059 | 59062 | −2.08 | 0.07 | 8 | −1.75 | 0.07 | 8 |
| J1932+1059 | 59497 | −1.77 | 0.09 | 8 | −1.53 | 0.04 | 8 |
| J2048−1616 | 59062 | −2.52 | 0.07 | 6 | −1.68 | 0.05 | 6 |

**Table 3.2:** Fitted arc curvature scaling indices for both left and right primary arcs. $N_\eta$ indicates the number of arc curvature measurements used in each fit. Measurements on MJD 59497 may have $N_\eta > 8$ due to this epoch being 155 minutes rather than the 40 minutes of the other observations, and so a new $\eta$ was measured after every 40 minutes, although arcs may not have been sufficiently resolved/detected in each 40 minute segment.

### 3.4.2 Scintillation Bandwidth & Scintillation Timescale Scaling Behavior

Our wide frequency coverage also allowed us to examine the scaling index of scintillation bandwidths and scintillation timescales. Under the assumption that ISM fluctuations follow behaviors consistent with a Kolmogorov medium and that the subinertial part of the wavenumber spectrum dominates, we should expect that scintillation bandwidths scale with frequency as $\Delta\nu_{\rm d} \propto \nu^{4.4}$ and $\Delta t_{\rm d} \propto \nu^{1.2}$ (Romani et al., 1986; Cordes & Rickett, 1998). Previous studies examining the scattering indices of various pulsars have done so using a number of methods, including multi-frequency measurements within one week (Krishnakumar et al., 2017), simultaneous multi-frequency measurements (Bhat et al., 2004; Bansal et al., 2019) (although the former primarily used two, and occasionally three, measurements and the latter was at frequencies less than 100 MHz), splitting up measurements from a single frequency band into multiple subbands (Levin et al., 2016; Krishnakumar et al., 2019; Chapter, 2), and using measurements from many epochs taken at two observing bands non-simultaneously (Chapter, 2). Since more measurements and more frequency coverage in a single epoch is ideal, the method used in Bhat et al. (2004) and Bansal et al. (2019) is the most preferred of the three. The method in this chapter utilizes a combination of this approach and the subband approach to maximize the number of delay measurements per epoch, which can be done thanks to our high frequency resolution and sensitivity in both observing bands. Not as many studies exist that examine scintillation timescale frequency scaling, in part due to the longer observing times required to measure these timescales in most pulsars. Most studies that do explore this behavior use measurements taken from disparate observations (Lewandowski et al., 2011), with those that have made measurements simultaneously at multiple frequencies being limited to ranges at much lower frequencies (Bhat et al., 2018).

Similar to Equation 5.5 that is used to determine the arc curvature scaling index, our scintillation bandwidth and scintillation timescale scaling indices $\xi$ at each epoch were

determined by performing a weighted linear least-squares fit of the form

$$\log_{10} \Delta\nu_{\rm d} = \xi \log_{10} \nu + b \tag{3.3}$$

and

$$\log_{10} \Delta t_{\rm d} = \xi \log_{10} \nu + b \tag{3.4}$$

for pulsars with at least four measurements at a given MJD. Example fits can be seen in Figure 3.2, with all measured indices listed in Table 5.1. We find that the majority of our scintillation bandwidth indices fit with Gaussians are consistent with scaling shallower than characteristic of a Kolmogorov medium, while half of our scintillation bandwidth indices fit with Lorentzians are consistent with scaling for a Kolmogorov medium. We also find half of our scintillation timescale indices to be consistent with a Kolmogorov medium and half to be consistent with a shallower spectrum. This behavior agrees well with general trends seen in previous studies, as both Bhat et al. (2004) and Bansal et al. (2019) found indices either consistent with a Kolmogorov medium or a shallower index than a Kolmogorov medium using delays measured by fitting pulse broadening functions, while Levin et al. (2016) and Chapter (2) only found indices that were shallower than a Kolmogorov medium using Gaussian fits to frequency ACFs. Krishnakumar et al. (2017) measured delays in 47 pulsars over a range of frequencies by fitting pulse broadening functions to pulse profiles and found almost 65% of those pulsars to exhibit scaling indices shallower than $-4.4$. Additionally, while Gaussians have been used to fit frequency ACFs in many scintillation studies, which is why we include them in our analyses, it is more mathematically appropriate to use Lorenztians given the Fourier relationship between the Lorentzian distribution and the one-sided exponential function that is assumed to characterize the impulse response function of the ISM. As such, our scintillation bandwidth indices obtained using Lorentzian-derived scintillation bandwidths likely provide a more accurate reflection of the turbulence of the ISM than our Gaussian measurements.

Many explanations have been given for why shallower-than-Kolmogorov medium behavior has been observed so frequently. Physical arguments have called into question the validity

of the simple infinite, thin screen model, demonstrating that shallower scaling indices are more consistent with finite, thin screens (Rickett et al., 2009). This is expected to be much more common among low DM pulsars (Cordes & Lazio, 2001), which agrees with our results, as all of the pulsars have dispersion measures below 40 pc $cm^{-3}$. Shallower indices have also been attributed to the existence of multiple finite screens along the LOS (Lewandowski et al., 2013b). This hypothesis agrees well with our measured indices for PSR B1133+16, as its indices are consistently shallower than that of a Kolmogorov medium and it is also known to have at least six distinct scattering screens (McKee et al., 2022).

Quality-of-data arguments have also been proposed. Chapter (2) suggested their shallower indices may be at least partially attributable to an imbalance of lower frequency data to higher frequency data for their multiple epoch approach as well as a lack of sufficient frequency resolution in their lower frequency band in some epochs. However, neither of these issues should affect our results, as our observations have a consistently even balance of low and high frequency measurements at all epochs and all of our measurements are well-resolved in frequency.

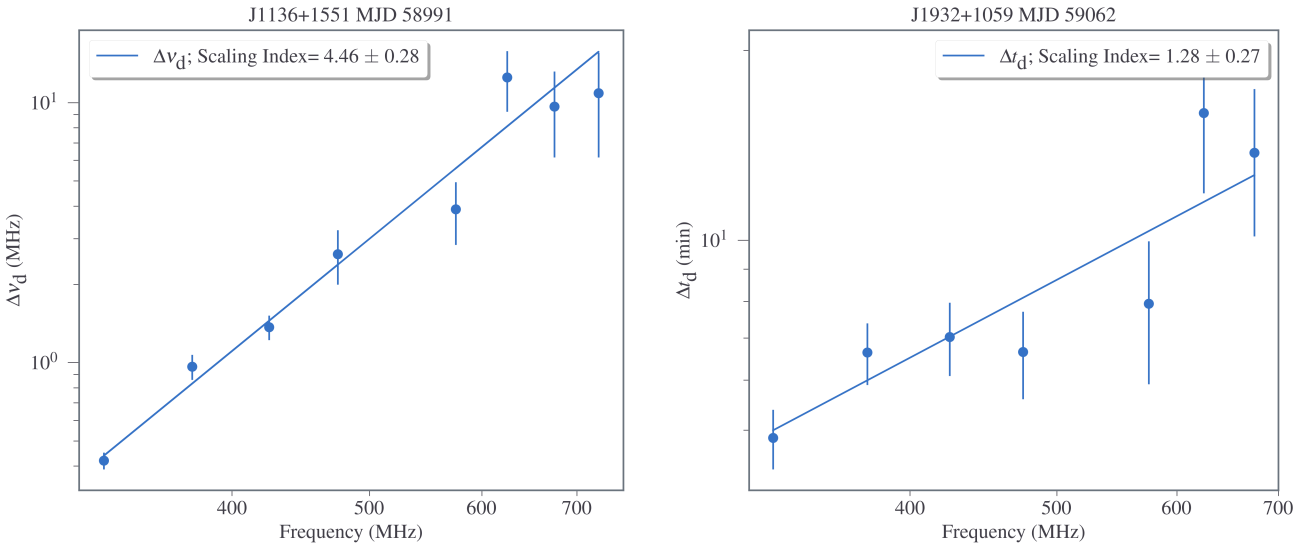


**(a)** Scintillation bandwidth scaling index fit for PSR J1136+1551 on MJD 58991

**(b)** Scintillation timescale scaling index fit for PSR J1932+1059 on MJD 59062.

**Figure 3.2:** Example scaling index fits

**Table 3.3:** Fitted Pulsar Scintillation Bandwidth & Scintillation Timescale Scaling Indices

| Pulsar | MJD | $\Delta\nu_{\rm d}$ Gaussian | $\Delta\nu_{\rm d}$ Gaussian Error | $\Delta\nu_{\rm d}$ Lorentzian | $\Delta\nu_{\rm d}$ Lorentzian Error | $N_{\Delta\nu_{\rm d}}$ | $\Delta t_{\rm d}$ Index | $\Delta t_{\rm d}$ Index Error | $N$ |
|---|---|---|---|---|---|---|---|---|---|
| J0630−2834 | 58987 | 4.85 | 0.66 | 4.85 | 0.65 | 8 | 1.02 | 0.25 | |
| J1136+1551 | 58987 | 2.63 | 0.78 | 3.47 | 1.05 | 7 | 1.51 | 0.21 | |
| J1136+1551 | 58991 | 3.74 | 0.25 | 4.46 | 0.28 | 8 | 0.70 | 0.12 | |
| J1136+1551 | 59115 | 2.72 | 0.35 | 2.87 | 0.37 | 8 | 0.56 | 0.27 | |
| J1136+1551 | 59497 | 3.46 | 0.64 | 4.07 | 0.58 | 14 | 0.71 | 0.16 | 1 |
| J1509+5531 | 59064 | 0.56 | 1.39 | 0.42 | 1.26 | 4 | 0.40 | 0.38 | |
| J1509+5531 | 59115 | 1.87 | 0.81 | 1.09 | 1.53 | 4 | 1.22 | 0.69 | |
| J1509+5531 | 59497 | 0.73 | 0.81 | 0.38 | 1.03 | 9 | −0.58 | 0.48 | |
| J1645−0317 | 59074 | 3.70 | 0.80 | 3.55 | 0.75 | 8 | 0.55 | 0.06 | |
| J1932+1059 | 58997 | 1.89 | 0.46 | 2.47 | 0.48 | 8 | −0.28 | 0.49 | |
| J1932+1059 | 59062 | 2.02 | 0.42 | 2.53 | 0.46 | 8 | 1.28 | 0.27 | |
| J1932+1059 | 59497 | 3.71 | 0.37 | 4.16 | 0.58 | 8 | 0.89 | 0.57 | |
| J2048−1616 | 59062 | 3.75 | 0.33 | 4.21 | 0.44 | 6 | 0.37 | 0.08 | |

**Table 3.3:** Fitted Pulsar Scintillation Bandwidth & Scintillation Timescale Scaling Indices

| Pulsar | MJD | $\Delta\nu_{\rm d}$ Gaussian | $\Delta\nu_{\rm d}$ Gaussian Error | $\Delta\nu_{\rm d}$ Lorentzian | $\Delta\nu_{\rm d}$ Lorentzian Error | $N_{\Delta\nu_{\rm d}}$ | $\Delta t_{\rm d}$ Index | $\Delta t_{\rm d}$ Index Error | $N$ |
|---|---|---|---|---|---|---|---|---|---|

**Table 3.3:** Fitted scintillation bandwidth and scintillation timescale scaling indices, with a minimum of four measurements ($N$) required in a given epoch to obtain a scaling index. Errors are uncertainties from parameter fits. The majority of our scintillation bandwidth indices fit with Gaussians are consistent with scaling shallower than characteristic of Kolmogorov medium, while the majority of our scintillation bandwidth indices fit with Lorentzians are consistent with scaling for a Kolmogorov medium. Measurements on MJD 59497 may have $N > 8$ due to this epoch being 155 minutes rather than the 40 minutes of the other observations, and so a new $\eta$ was measured after every 40 minutes, although arcs may not have been sufficiently resolved/detected in each 40 minute segment.

### 3.4.3 Relation Between Arc Curvature and Scintillation Parameters

Under the assumption that scattering resulting in a given scintillation arc is both one-dimensional and occurring at a thin screen, it becomes possible to relate arc curvature to the scintillation bandwidth and timescale (Cordes et al., 2006b; Stinebring et al., 2022). This relation can be described by the so-called pseudo-curvature, $\eta_{\rm ISS}$, given by

$$\eta_{\rm ISS} = \frac{2\pi\Delta t_{\rm d}^2}{\Delta\nu_{\rm d}}. \tag{3.5}$$

While the relation between $\eta_{\rm ISS}$ and $\eta$ has been strongly demonstrated in large surveys across many pulsars (Stinebring et al., 2022), our wide frequency coverage and high resolution uniquely allow for the exploration of this relation within individual epochs. To accomplish this, in each epoch, for a given pulsar that had at least four measurements of arc curvature in a given arm and four measurements of both scintillation bandwidth and timescale, we determined the weighted linear correlation coefficient in log space between $\eta_{\rm ISS}$ and $\eta$. We also determined the power law relation between $\eta_{\rm ISS}$ and $\eta$ using relations of the same form as Equations 5.6 and 3.4 to determine the degree of one-to-one correspondence, with a scaling index of one and $10^b$ of one indicating perfect equivalence. The results of these analyses can be seen in Table 3.4, while an example can be seen in Figure 3.3.

Overall, we found strong correlations between these two estimates of curvature, with the majority of correlation coefficients being above 0.8, and the majority of fits closely following a one-to-one correspondence, with a weighted average index of $1.16 \pm 0.05$ and weighted average $10^b$ of $0.13 \pm 0.01$, indicating our assumption of one-dimensional, thin-screen scattering is justified across these LOS's. A comparison of the measured $\eta$, $\Delta\nu_{\rm d}$, and $\Delta t_{\rm d}$ power laws in 3D space using the corresponding correlation coefficients as a gauge shows some evidence that these correlation coefficients generally increase the closer all three power laws converge to their expected scaling indices given our various physical assumptions, as shown in Figure 3.4.

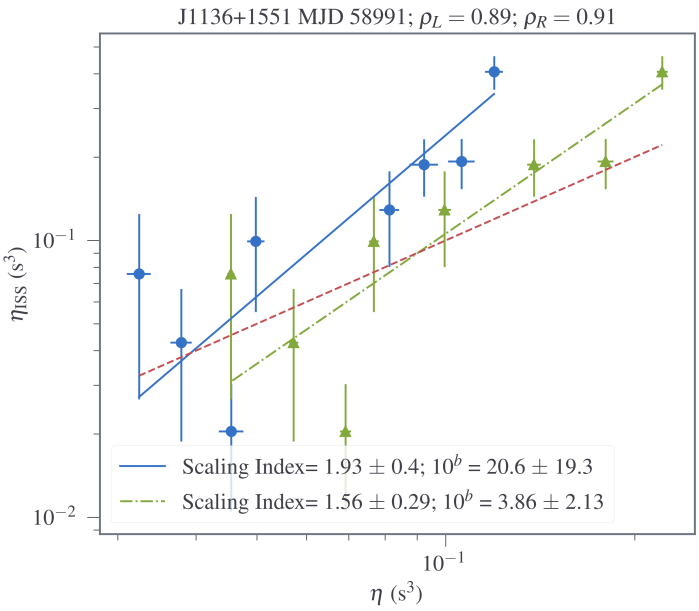


**Figure 3.3:** Example comparison between $\eta_{\rm ISS}$ and $\eta$ for PSR J1136+1551 on MJD 58991 for both the left (solid blue with dots) and right (dotted-dashed green with triangles) arms of the scintillation arc visible in the observation, with corresponding power law fits, and correlation coefficients $\rho_{\rm L}$ and $\rho_{\rm R}$, respectively. The dashed red line indicates a perfect one-to-one correspondence.

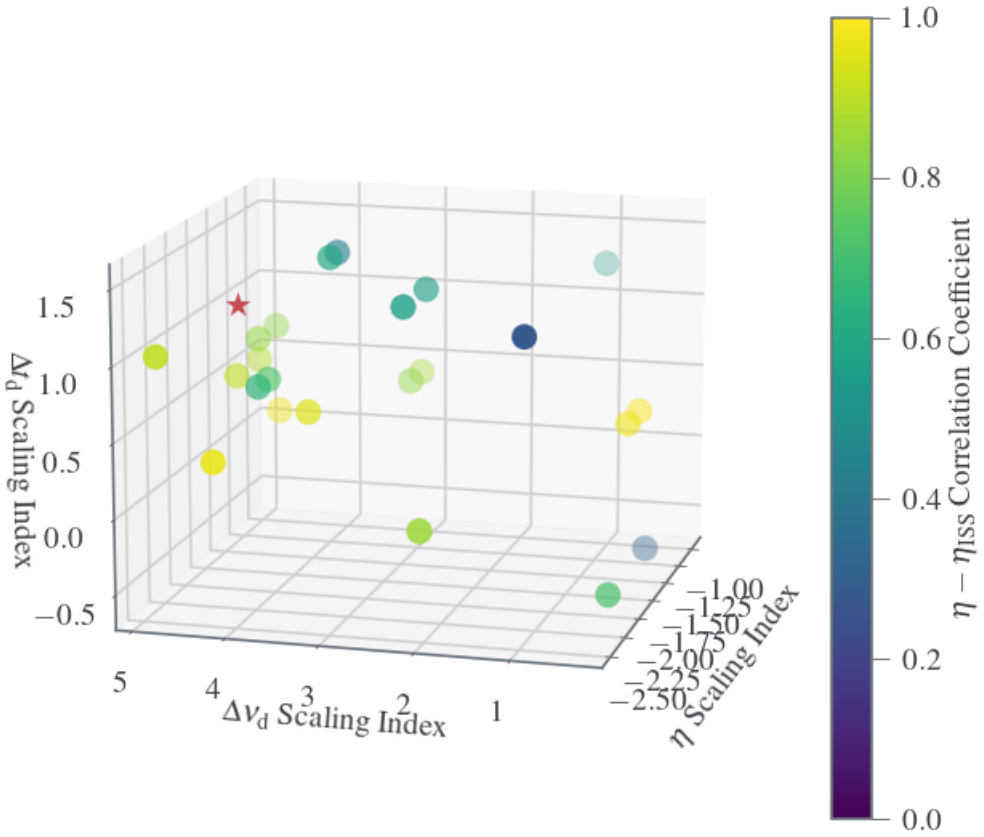


**Figure 3.4:** A comparison of the measured $\eta$, $\Delta\nu_{\mathrm{d}}$, and $\Delta t_{\mathrm{d}}$ power laws with the correlation coefficients of the $\eta - \eta_{\mathrm{ISS}}$ relation (dots), with the red star indicating a power law in $\eta$ of $-2$, a power law in $\Delta\nu_{\mathrm{d}}$ of 4.4, and a power law in $\Delta t_{\mathrm{d}}$ of 1.2. There is minor evidence that, the closer these three quantities get to their expected scaling indices, the closer the correlation coefficient gets to one.

**Table 3.4:** Relation Between $\eta$ and $\eta_{\rm ISS}$

| Pulsar | MJD | $\rho_{\rm L}$ | Left Index | Left $10^b$ | $N_{\eta,{\rm L}}$ | $\rho_{\rm R}$ | Right Index | Right $10^b$ | $N_{\eta,{\rm R}}$ |
|---|---|---|---|---|---|---|---|---|---|
| J0630−2834 | 58987 | — | — | — | — | 0.91 | 1.35 ± 0.26 | 0.72 ± 0.12 | 8 |
| J1136+1551 | 58987 | 0.42 | 0.56 ± 0.60 | 0.38 ± 0.50 | 7 | 0.60 | 0.61 ± 0.41 | 0.36 ± 0.28 | 7 |
| J1136+1551 | 58991 | 0.89 | 1.93 ± 0.40 | 20.6 ± 19.3 | 8 | 0.91 | 1.56 ± 0.29 | 3.89 ± 2.13 | 8 |
| J1136+1551 | 59115 | 0.86 | 1.24 ± 0.30 | 2.70 ± 2.39 | 8 | 0.83 | 1.15 ± 0.31 | 1.64 ± 1.38 | 8 |
| J1136+1551 | 59497 | 0.66 | 1.12 ± 0.37 | 2.77 ± 3.04 | 14 | 0.73 | 1.30 ± 0.36 | 4.80 ± 5.09 | 14 |
| J1509+5531 | 59064 | 0.98 | 1.03 ± 0.14 | 0.13 ± 0.01 | 4 | 0.99 | 1.21 ± 0.15 | 0.14 ± 0.01 | 4 |
| J1509+5531 | 59115 | 0.52 | 0.52 ± 0.61 | 0.10 ± 0.09 | 4 | 0.28 | 0.12 ± 0.29 | 0.06 ± 0.02 | 4 |
| J1509+5531 | 59497 | 0.72 | 0.70 ± 0.25 | 1.23 ± 0.51 | 9 | 0.31 | 0.67 ± 0.78 | 0.96 ± 0.97 | 9 |
| J1645−0317 | 59074 | 0.95 | 1.14 ± 0.26 | 0.95 ± 0.39 | 4 | — | — | — | — |
| J1932+1059 | 58997 | 0.84 | 1.48 ± 0.39 | 6.44 ± 4.62 | 8 | 0.87 | 1.56 ± 0.37 | 8.09 ± 5.65 | 8 |
| J1932+1059 | 59062 | 0.57 | 0.90 ± 0.76 | 1.97 ± 2.25 | 7 | 0.55 | 0.91 ± 0.80 | 2.39 ± 3.23 | 7 |
| J1932+1059 | 59497 | 0.84 | 2.17 ± 0.59 | 52.0 ± 53.9 | 8 | 0.87 | 2.45 ± 0.69 | 128 ± 168 | 8 |
| J2048−1616 | 59062 | 0.97 | 1.36 ± 0.18 | 3.26 ± 1.24 | 6 | 0.98 | 2.01 ± 0.23 | 39.3 ± 23.3 | 6 |

**Table 3.4:** Relation Between $\eta$ and $\eta_{\rm ISS}$

| Pulsar | MJD | $\rho_{\rm L}$ | Left Index | Left $10^b$ | $N_{\eta,{\rm L}}$ | $\rho_{\rm R}$ | Right Index | Right $10^b$ | $N_{\eta,{\rm R}}$ |
|---|---|---|---|---|---|---|---|---|---|

**Table 3.4:** Linear correlation coefficients, $\rho$, and power law fits in log space between measured arc curvature $\eta$ and pseudo-curvature $\eta_{\rm ISS}$ for both left and right arms of scintillation arcs. $N_\eta$ indicates the number of arc curvature measurements used in each fit. Measurements on MJD 59497 may have $N_\eta > 8$ due to this epoch being 155 minutes rather than the 40 minutes of the other observations, and so a new $\eta$ was measured after every 40 minutes, although arcs may not have been sufficiently resolved/detected in each 40 minute segment.

### 3.4.4 155 Minute Observation

The inclusion of a 155 minute observation in our survey on MJD 59497 allowed for an analysis of short-term arc curvature variation in some pulsars, as observations had to be paused every 40 minutes for a five minute phase calibration, resulting in multiple 40 minute scans. For pulsars with at least two arc curvature measurements in a given scintillation arc at a given observing frequency, we examined how a given arc curvature measurement at a given observing frequency, $\eta_{\nu,i}$ varied with respect to the weighted average curvature for that arm and frequency over the entire epoch, $\overline{\eta_\nu}$. The percent difference $\chi$ between these two quantities is then given by

$$\chi = 100 \frac{|\overline{\eta_\nu} - \eta_{\nu,i}|}{\frac{\overline{\eta_\nu} + \eta_{\nu,i}}{2}}. \tag{3.6}$$

For PSR J1136+1551, all observing frequencies centered at or below 475 MHz had three arc curvature measurements (the higher frequency observations only had one arc curvature measurement) in each primary arm (the brightest arm, overwhelmingly often the arm with the highest curvature) at each frequency, with the accumulation of all percent differences yielding a bimodal distribution with peaks around percent differences of 2% (16 arc curvature measurements) and 7% (eight arc curvature measurements). The mean was 3.7% and the median was 2.8%, while largest percent difference away from a weighted mean was 7.9±0.2% and the smallest was 0.14±1.91%, although the majority of all percent differences were below 3%. All of this strongly indicates the ISM underwent very little change along the LOS to this pulsar over the course of a given observation. This result is supported by this pulsar's incredibly low dispersion measure, meaning it does not sample a sizeable portion of the ISM along its LOS relative to many pulsars that are observed (Bilous et al., 2016; Manchester et al., 2005b; Pilkington et al., 1968).

For PSR J1509+5531, all observing frequencies centered at or above 575 MHz had at least two arc curvature measurements in each arm at each frequency (no arcs were sufficiently resolved in the lower frequency band), with the accumulation of all percent differences resulting in a one-sided distribution peaked around 6% (18 arc curvature measurements). The mean was

10.1% and the median was 6.6%, while the smallest percent difference away from a weighted mean was 1.2±2.1%, and the largest was 36.4±0.1%, although the next largest after that was only 21.7±0.1%, meaning this maximum was an extreme outlier. The majority of all percent differences were below 7%. As with the previous pulsar, this also strongly indicates the ISM underwent very little change along the LOS to this pulsar over the course of a given observation, a result again supported by this pulsar's fairly low dispersion measure (Huguenin et al., 1968; Manchester et al., 2005b). The fact that this pulsar shows higher variation compared to PSR J1136+1551 is likely due to PSR J1509+5531 having a dispersion measure four times higher and a transverse velocity 45% larger (Bilous et al., 2016; Huguenin et al., 1968; Manchester et al., 2005b; Pilkington et al., 1968; Stovall et al., 2015), so a significantly larger fraction of the ISM was sampled during its observation, increasing the likelihood of larger scintillation-based variations.

Only one arc curvature measurement in each frequency was obtainable at this MJD for PSR J1932+1059, and so the above analysis was not possible.

The next few subsections highlight the features of a few pulsars in the survey.

### 3.4.5 J0630-2834

In the one epoch for which we were able to resolve a scintillation arc, only the right arm was resolvable across all frequencies, with its relative brightness with respect to the left side of the fringe frequency axis consistently decreasing as frequency increased. An example of this asymmetry can be seen in Figure 3.5. This strong asymmetry is known to be the result of refraction leading to scintillation drifting in the dynamic spectra (Cordes et al., 2006b). Interestingly, although one would expect an increase in scintillation drift to coincide with an increase in the asymmetry, the magnitude of our measured scintillation drift rates seem to mildly favor an increase with frequency whereas the asymmetry appears to decrease with frequency.

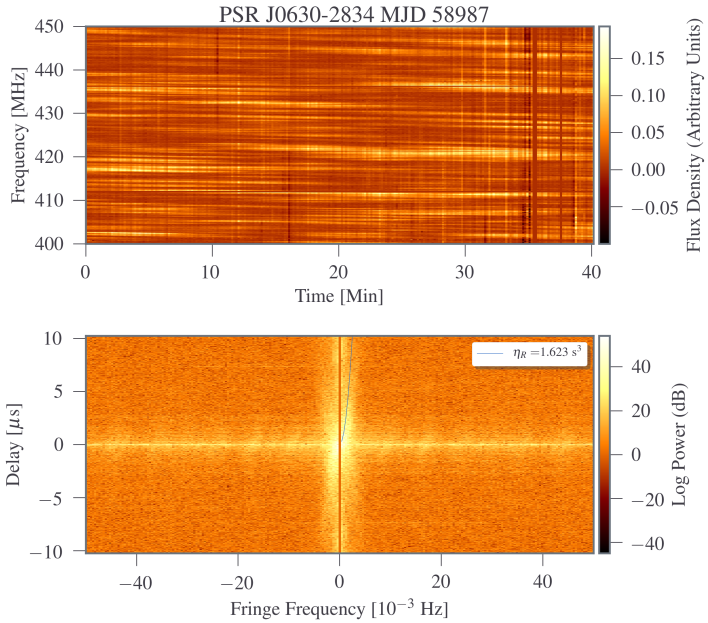


**Figure 3.5:** An example dynamic (top) and secondary (bottom) spectrum from PSR J0630-2834 on MJD 58987 centered at 425 MHz. There is a clear asymmetry in the secondary spectrum, with the right arm being the dominant feature. This is likely the result of refraction along the line of sight. The blue line represents the arc curvature fit.

### 3.4.6 J1136+1551

This pulsar is well known for having the uncommon feature of multiple scintillation arcs, implying multiple scattering screens along its LOS (Hill et al., 2003b; Stinebring et al., 2019). In the literature, six distinct sets of arcs have been found over a ∼34 year span of observations (McKee et al., 2022). In three of the four epochs in which we observed this pulsar, we detected multiple arcs, an example of which can be seen in Figure 3.6.

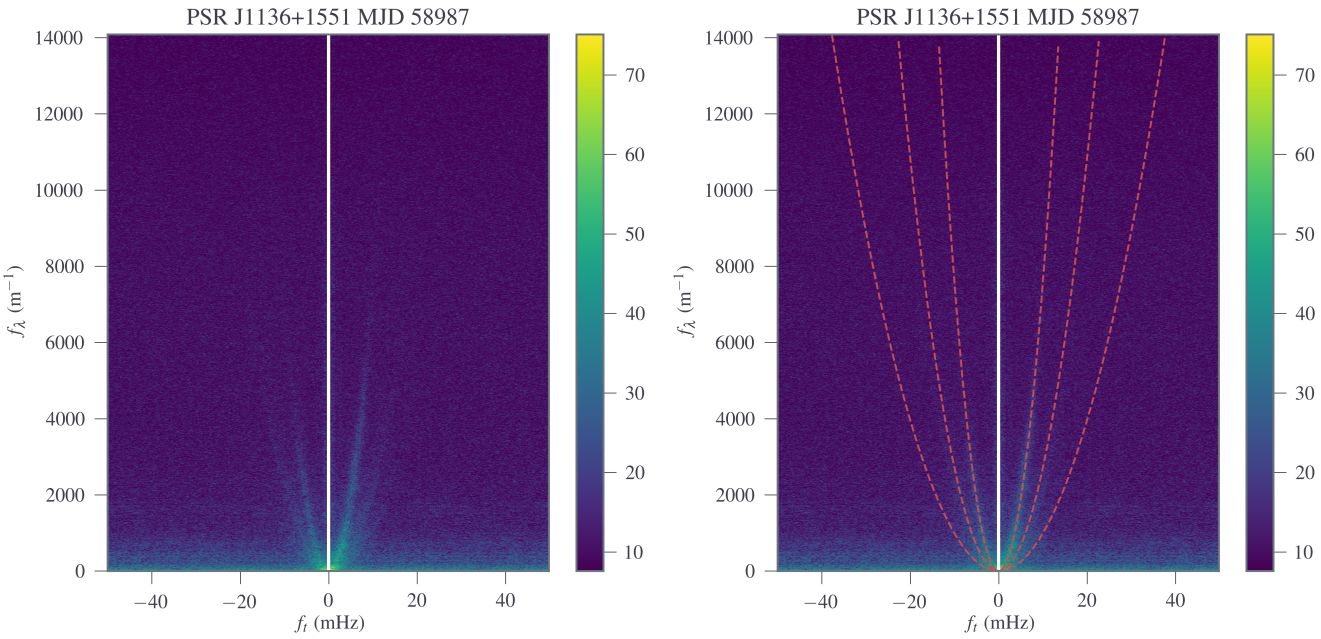


**(a)** Scintillation arcs without overlaid fits **(b)** Scintillation arcs with overlaid fits

**Figure 3.6:** Secondary spectrum of PSR J1136+1551 at 650 MHz on MJD 58987 showing the detection of three distinct scintillation arcs. The dynamic spectrum used to make these figures was resampled to be uniform in wavelength rather frequency in order to better resolve the additional distinct arcs, which were not quite as resolved using the latter sampling approach.

After scaling our measurements to 1400 MHz and using the convention from McKee et al. (2022), we can conclude that we detected arcs B, C, and E on MJDs 58987 and 58991 and arcs C and D on MJD 59115, with arc C being the only detectable arc on MJD 59497.

All multiple-arc detections were made only in the observations using uGMRT's band 4, which was centered at 650 MHz. The fact that the two epochs closest to each other in our survey (MJDs 58987 and 58991) both detected the same sets of arcs may hint at a timescale over which certain screens have a larger influence over the pulsar signal propagation. McKee et al. (2022) demonstrates how for this pulsar anywhere from one to six arcs may be visible in a given observation, with the number of visible arcs possibly changing on approximately week timescales, assuming the ISM along the LOS to this pulsar is consistent modulo one year. This, along with our results showing observations within a four day window to be dominated by the same screen, suggests a fairly short but currently unknown window within which the influence of a given screen will fluctuate, likely on the order of one week.

The existence of multiple screens along the LOS to this pulsar may also help to partially explain discrepancies between our scintillation bandwidth power-law fits and those of Wu et al. (2022), where two of our four Gaussian ACF fit-derived scaling indices are shallower than the index acquired from their observation. While we observed anywhere from one to three arcs in our observations, indicating anywhere from one to three scattering screens having a dominant influence over the pulsar emission's propagation, their observation of this pulsar only had one visible arc and therefore one dominant scattering screen. As discussed earlier, Lewandowski et al. (2013b) mentions that deviations from a single thin screen scattering geometry (e.g., multiple thin screens) can result in scaling indices shallower than $-4$. The observations in Wu et al. (2022) are also taken at significantly lower observing frequencies (148$-$152 MHz), where it is much more likely for only single arcs to be observed. This is a consequence of the ISM looking more like a continuous medium when observed at lower frequencies, whereas at higher frequencies we are more likely to observe single scatterings off of individual screens.

An examination of the power in each of the arms show notable levels of asymmetry along the delay axis, and consequently a notable amount of refraction, in all detectable arms and across all frequencies in the first two epochs, with the right arm having more power and extending further out on the delay axis. This asymmetry clearly decreases over the course of our observations across all frequencies until our final observation, where the arcs have approximately

even levels of power or the left arc starts to dominate in the asymmetry. This trend is generally supported by the measured scintillation drift rates as well, especially for data taken at band 4 (650 MHz), i.e., the same band where the multiple arcs were visible, as measured drifts are generally negative during the first three epochs and then considerably positive during the final epoch.

Perhaps the most interesting finding from our observations of this pulsar is the discovery of a strong correlation between the measured arc curvatures and the arc asymmetry index, $A(f_\nu)$, which is a metric that describes the relative power between the left and right arms and is found by comparing the average power along each arm via

$$A(f_\nu) = \frac{\overline{P_R(f_\nu)} - \overline{P_L(f_\nu)}}{\overline{P_R(f_\nu)} + \overline{P_L(f_\nu)}}, \tag{3.7}$$

with a larger index magnitude indicating greater asymmetry. We believe this correlation has never before been reported and wish to use it as a cautionary tale for those attempting similar analyses in the future, as we suspect this correlation to be a consequence of a bias in the Hough transform approach used to acquire these asymmetry measurements. To test our conjecture, we used the SCREENS package (van Kerkwijk & van Lieshout, 2022) to simulate a one-dimensional phase screen where rays scattered at positive angles were 30% brighter than those scattered at negative angles for a pulsar with the same astrometrical properties as PSR J1136+1551 under the assumption that the pulsar motion dominates the effective velocity and using the same observing setup as our observations. We then repeated the simulation at 50 fractional screen distances between $0.5-0.8$ while using the same image on the sky in each setup. This fractional screen distance range was chosen to allow for significant exploration of the phenomenon along the LOS while limiting the proximity of the screen to Earth so that we could safely ignore the motion of the Earth in our simulation.

An example dynamic and secondary spectrum pair from our non-simulated observations is shown in Figure 3.7, with its corresponding normalized secondary spectrum power profile, which is used to determine the asymmetry index, shown in Figure 3.8, while the scatter plot

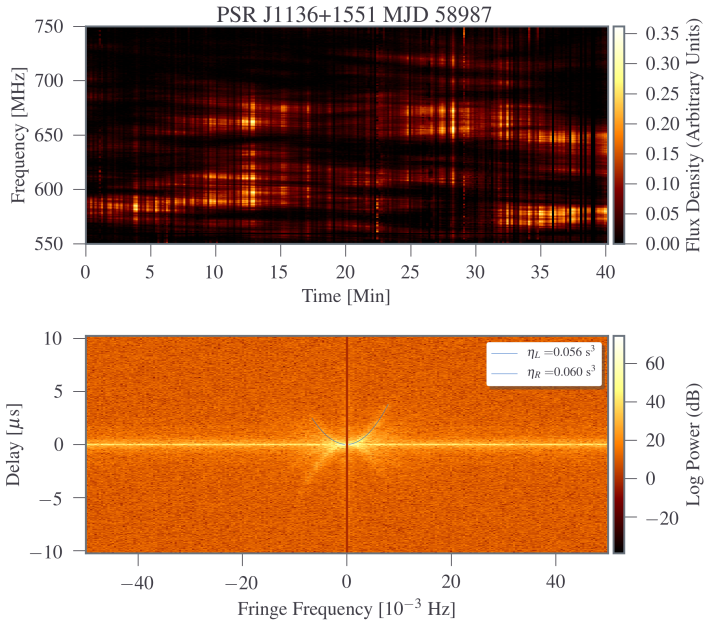


**Figure 3.7:** Dynamic (top) and secondary (bottom) spectra of PSR J1136+1551 centered at 650 MHz on MJD 58987. The top half of the secondary spectrum shows the overlaid arc fits in blue.

showing the relation between measured arc curvature and arc asymmetry index across all measurements taken in the 650 MHz band, along with our simulated data, is shown in Figure 3.9. As seen in Figure 3.9, despite the image on the sky remaining the same in each of our simulations, the asymmetry gets progressively larger as we go to higher curvatures. For this reason we conclude this correlation to be the result of a bias in the Hough transform approach for measuring arc curvatures and the resulting normalized secondary spectra. Of particular note in Figure 3.9 are the three distinct clumps in our measured data, which we believe are the result of our observations being dominated by a different scattering screen at each epoch (two of our observations were taken four days apart, and so are dominated by the same screen). It is likely that this pulsar's at least six known scattering screens are the main reason why we were able to see this correlation in our data in the first place, as individual scattering screens likely do not vary enough in distance over time for this trend to become apparent. Indeed, the limited

number of pulsars with multiple known screens is probably the main reason why this trend has not been reported in earlier studies.

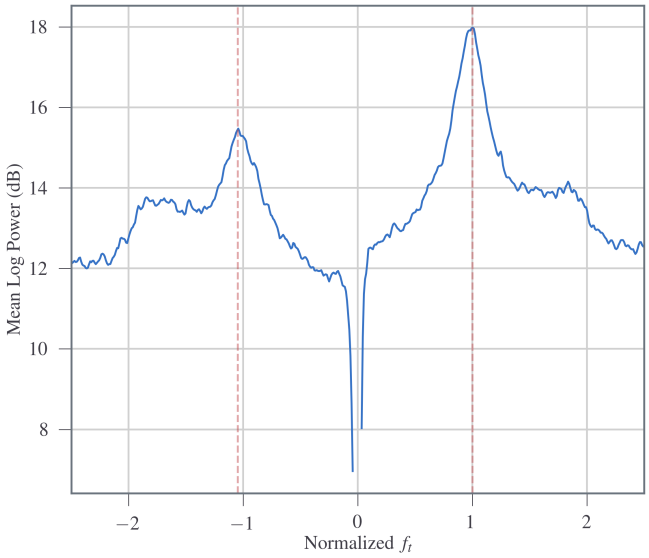


**Figure 3.8:** Normalized secondary spectrum power profile of PSR J1136+1551 centered at 650 MHz on MJD 58987. The vertical dashed lines indicate where the arcs fall on the normalized delay axis.

### 3.4.7 J1509+5531

In the observations of this pulsar in the 650 MHz band, all secondary spectra featured patchy rather than continuous arcs, particularly in the left arm. This patchiness indicates a detection of this pulsar's arclets, which result from substructures in the ISM thought to arise from scattering interference between an inhomogeneously scattered distribution of material and some distinct offset region (Walker & Stinebring, 2005; Cordes et al., 2006b). Under the assumption that these substructures are lens-like, they are expected to be roughly AU in scale (Hill et al., 2005). Unique to these arclets is their distinctly flat nature, which has been attributed to its exceptionally high transverse velocity of $960^{+61}_{-64}$ km s$^{-1}$ (Chatterjee et al.,

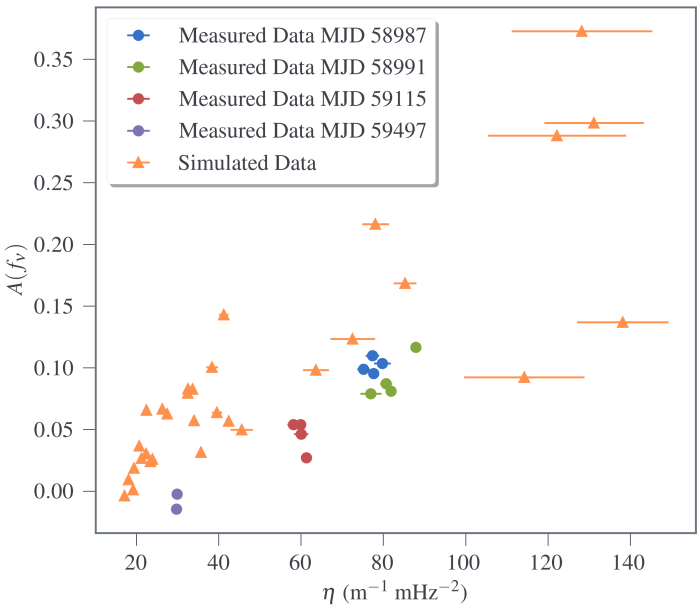


**Figure 3.9:** Scatter plot showing simulated (orange triangles) and measured (dots of various colors) arc curvatures and the corresponding asymmetry indices for all measurements of PSR J1136+1551 taken with Band 4. The three distinct clumps in the measured data are the result of the observations being dominated by three different scattering screens.

2009). Interestingly, the arc curvatures measured in the last two epochs (MJDs 59115 and 59497) are a factor of two to three times smaller than the first two epochs (MJDs 59064 and 58987), possibly indicating a detection of multiple scattering screens along the LOS to this pulsar. This result augments the results of Sprenger et al. (2022), who also found significant variability along the LOS to this pulsar during the same period of time and propose a double screen model as a possible explanation. An example observation from the earlier two epochs is shown in Figure 3.10, while an example from the later two epochs is shown in Figure 3.11.

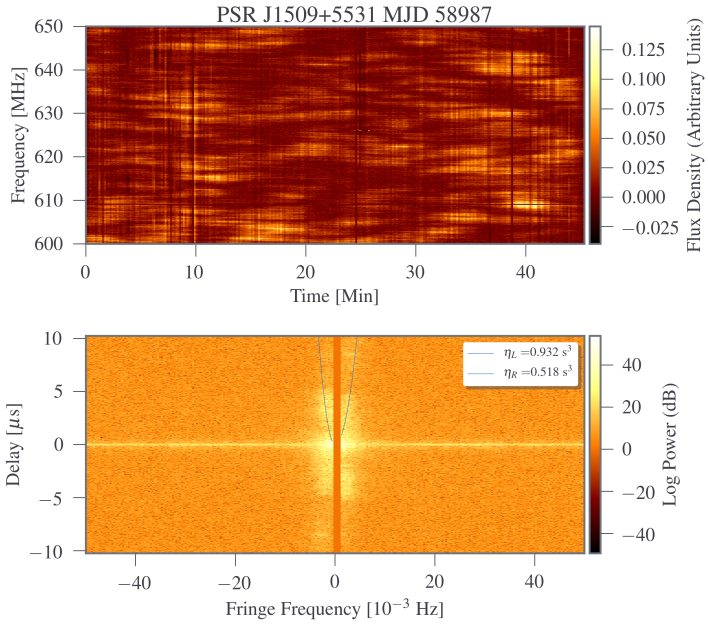


**Figure 3.10:** Dynamic (top) and secondary (bottom) spectra of PSR J1509+5531 centered at 625 MHz on MJD 58987. The top half of the secondary spectrum shows the overlaid arc fits in blue. During this period of observations, visible arcs were considerably narrower than later observations.

### 3.4.8 J1645-0317

In the one epoch for which we were able to resolve a scintillation arc in this pulsar, its power was found to be highly concentrated towards the origin, indicating strong scintillation with the majority of the power in its brightness distribution originating from around $\theta = 0$ (Cordes et al., 2006b). There is also considerably more power on the left side of the fringe frequency axis, indicating strong refraction occurring during this epoch. An example observation is shown in Figure 3.12.

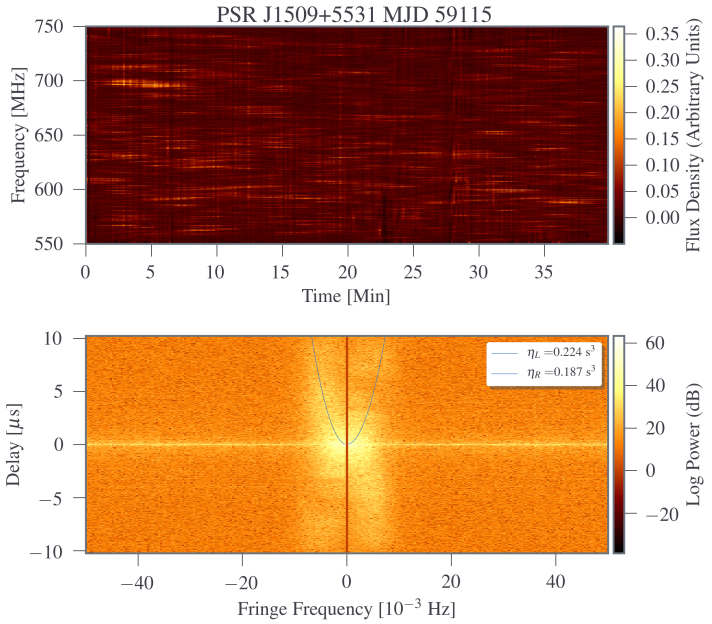


**Figure 3.11:** Dynamic (top) and secondary (bottom) spectra of PSR J1509+5531 centered at 650 MHz on MJD 59115. The top half of the secondary spectrum shows the overlaid arc fits in blue. During this period of observations, visible arcs were considerably wider than earlier observations.

### 3.4.9 J1932+1059

Due to having the lowest DM in our survey, this pulsar showed the least variation in arc curvature from epoch to epoch across all frequencies. Its close proximity to Earth also resulted in wide scintles in frequency, leading to high scintle resolution and very bright, narrow, and well defined arcs. The sharpness of these arcs may also indicate scattering that is highly anisotropic along the LOS (Walker et al., 2004; Cordes et al., 2006b), as well as originating from a discrete, localized source (Stinebring et al., 2001c). Overall this was our most consistent pulsar in all aspects of scintillation.

This consistency lines up with its other astrophysical parameters, as its dispersion measure of 3.18 pc cm$^{-3}$ (Large et al., 1968; Manchester et al., 2005b) was the lowest in our survey and its transverse velocity of 152 km s$^{-1}$ (Bilous et al., 2016; Manchester et al., 2005b)

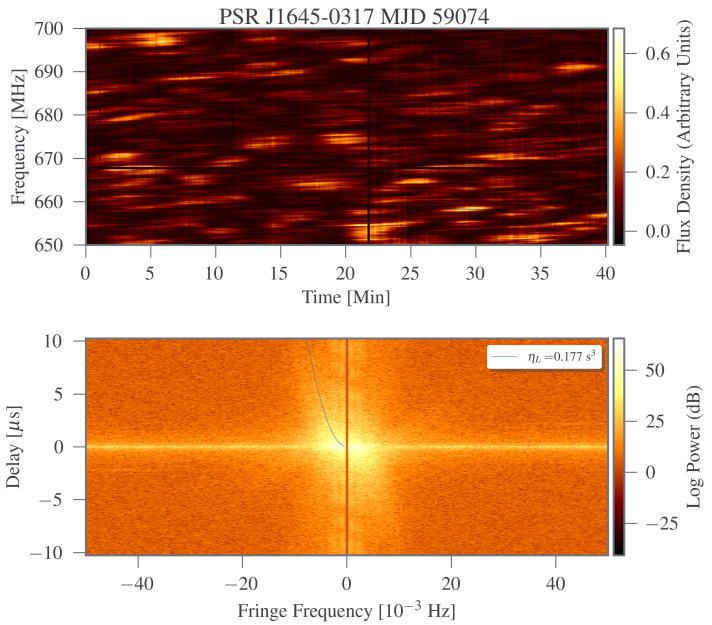


**Figure 3.12:** Dynamic (top) and secondary (bottom) spectra of PSR J1645-0317 centered at 675 MHz on MJD 59074. The top half of the secondary spectrum shows the overlaid arc fits in blue.

was the second lowest. While its transverse velocity is a bit larger than that of PSR J0630−2834 and their distances are almost equivalent, PSR J0630−2834 has a dispersion measure 10 times higher than PSR J1932+1059 (Large et al., 1968, 1969; Manchester et al., 2005b). This means that a much denser ISM was sampled in PSR J0630−2834 than in PSR J1932+1059, meaning that PSR J1932+1059 had decisively the least amount of ISM sampled over our survey, making it the least likely to experience large scintillation-related variations. An example observation is shown in Figure 3.13.

Like in the case of PSR J1136+1551, two of our three Gaussian frequency ACF-derived scintillation bandwidth scaling indices are shallower than the measured index using lower observing frequencies from Wu et al. (2022). In the case of this pulsar, our observations also overlap theirs in time, meaning we would expect similar LOS behavior, although it has been observed that the measured scaling index along the LOS to a given pulsar can vary over time (Levin et al., 2016; Chapter, 2). Interestingly, when comparing the discrepancies between our scaling indices and Wu et al. (2022) using the time of year in which the observations were made, the closer our observing epochs are to theirs as a fraction of a year, the more our measured scaling indices agree. More specifically, looking at the difference between epochs in days relative to a calendar year, they measured a scaling index of $4.00 \pm 0.37$, and we found scaling indices of $1.89 \pm 0.46$, $2.02 \pm 0.42$, and $3.71 \pm 0.37$ with day differences of 151, 149, and 82 from their epoch, respectively. It is known that other ISM-related quantities such arc curvature (Main et al., 2020; McKee et al., 2022) and dispersion measure (Hazboun et al., 2022) have annual variations, and it is expected that scintillation bandwidth should correlate with dispersion measure (Kuzmin, A. et al., 2008; Coles et al., 2015; Lentati et al., 2017; McKee et al., 2018), meaning we might expect some annual trend in scintillation bandwidth measurements as well. However, it seems unlikely that the annual variations in electron density contributions from the solar wind would noticeably affect measured ISM turbulence, much less to the degree seen in our data.

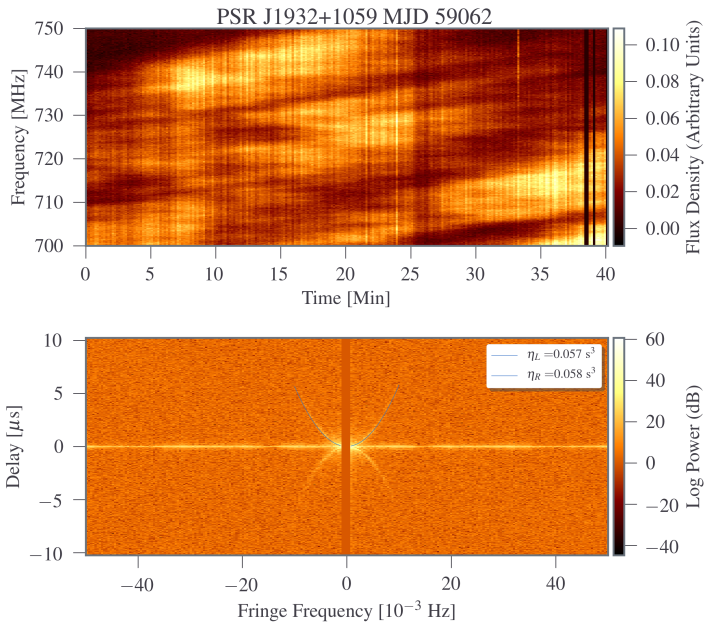


**Figure 3.13:** Dynamic (top) and secondary (bottom) spectra of PSR J1932+1059 centered at 725 MHz on MJD 58987. The top half of the secondary spectrum shows the overlaid arc fits in blue.

### 3.4.10 J2048-1616

This pulsar exhibited strong pulse intensity variability at all observing frequencies, resulting in significant flux density variation within individual scintles. The scintillation arcs for this pulsar exhibit high levels of asymmetry, potentially a consequence of refraction. This strong asymmetry is also accompanied by a highly asymmetric scaling of the arc curvature in both arms (see Table 5.2), with the left and right arms exhibiting noticeably steeper and shallower arc curvature scaling indices, respectively, than would be expected as a consequence of pure plasma refraction. This asymmetry diminishes noticeably with observing frequency, visible both by eye and by looking at $A(f_\nu)$ as a function of frequency, possibly a consequence of weaker refraction at higher observing frequencies. Additionally, the thickness of these arcs also sharply decreases with frequency, being barely visible over the power near the origin at low frequencies and very sharply defined at higher frequencies. Stinebring et al. (2019) examined how the width of scintillation arcs change with frequency in PSR J1136+1151, also observing a decrease in thickness with frequency. They concluded these effects could be explained by a linear, one-dimensional brightness function and an anisotropic brightness distribution, which describe how the brightness of the scattered image changes with the angular deflection of the scattered ray in 1D and 2D, respectively. An example observation is shown in Figure 3.14.

## 3.5 Conclusions & Future Work

We performed simultaneous dual-frequency observations of six bright canonical pulsars using the uGMRT. We extracted scintillation arc, bandwidth, and timescale measurements for each of these pulsars to examine a variety of science. We examined how arc curvature scaled with frequency and found our observations to be consistent with the index predicted by theory and demonstrated in the literature, while at the same time using a more astronomically ideal setup to perform these measurements. We also measured scintillation bandwidth and scintillation timescale scaling indices for five of our six pulsars and found indices consistent with

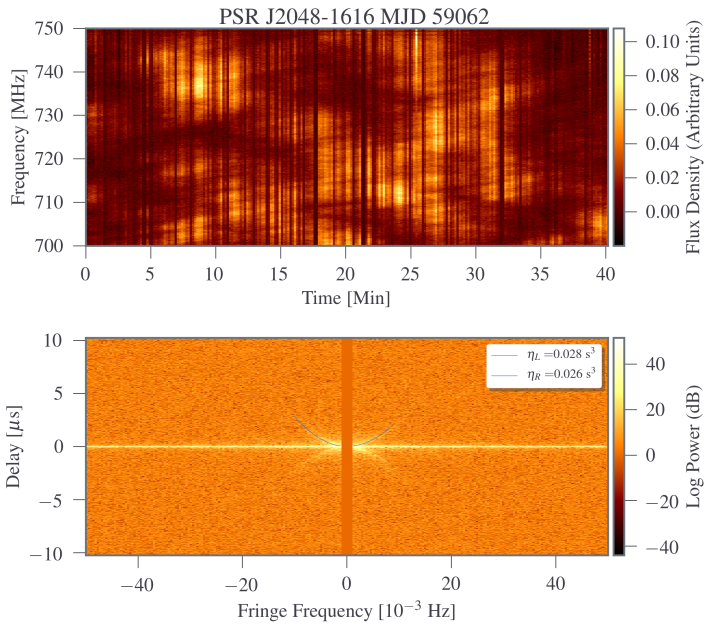


**Figure 3.14:** Dynamic (top) and secondary (bottom) spectra of PSR J2048-1616 centered at 725 MHz on MJD 58987. The top half of the secondary spectrum shows the overlaid arc fits in blue.

or shallower than Kolmogorov turbulence, agreeing with previous literature. We examine the relation between arc curvature and scintillation bandwidth and timescale within epochs and find strong correlation between the measured curvature and pseudo-curvature, indicating our assumptions of one-dimensional, thin screen scattering are justified. Finally, we find an interesting and strong correlation between arc curvature and arc asymmetry in PSR J1136+1551, which we attribute to a bias in the Hough transform method for measuring arc curvatures.

This study demonstrates the value of array-based telescopes such as uGMRT to the pulsar astronomy community, as well as the strengths of simultaneous multiband studies of pulsars and the wide variety of science that can be done with such an approach. This also shows strong promise for the future observations using ultrawideband (UWB) receivers, which are coming online at instruments such as the Green Bank Telescope.

We thank the staff at the uGMRT who have made these observations possible. The uGMRT is run by the National Centre for Radio Astrophysics of the Tata Institute of Fundamental Research. We would also like to thank Daniel Baker, Marten van Kerkwijk, Ue-Li Pen, and the rest of the scintillometry group at University of Toronto for crucial discussions surrounding our scintillation arc asymmetry analyses. We gratefully acknowledge support of this effort from the NSF Physics Frontiers Center grants 1430284 and 2020265 to NANOGrav. Some of the data processing in this work utilized the resources of the Bowser computing cluster at West Virginia University.

*Software*: SCINTOOLS (Reardon et al., 2020), SCREENS (van Kerkwijk & van Lieshout, 2022), PYPULSE (Lam, 2017), SCIPY (Virtanen et al., 2020), NUMPY (van der Walt et al., 2011), and MATPLOTLIB Hunter (2007).

# Chapter 4. Scattering Delay Mitigation in High Accuracy Pulsar Timing: Cyclic Spectroscopy Techniques

## 4.1 Introduction

High-accuracy pulsar timing has been a transformative technique across a wide range of astrophysical fields, including neutron star mass measurements, binary star evolution, exacting tests of general relativity, pulsar astrometry, and studies of the interstellar medium (ISM). Now, in the era of pulsar timing arrays (PTAs), astronomers are poised to explore a gravitational-wave background due to supermassive black hole binaries (SMBHBs) located in galaxies at cosmic distances. Hints at the existence of such a background are already emerging in the data sets of PTAs through the presence of a common red noise process in the times-of-arrival (TOAs) of pulsars observed by the three major world-wide PTA collaborations (Arzoumanian et al., 2020b; Chen et al., 2021; Goncharov et al., 2021; Antoniadis et al., 2022). Such studies require attention to a myriad of details and careful understanding and correction for systematic effects due to a wide variety of sources: Earth rotation irregularities, solar system ephemeris inaccuracies, and even atomic time wander relative to an ensemble of highly accurate pulsar clocks (Alam et al., 2020b). Propagation of radio waves from pulsars to the Earth through the ionized, inhomogeneous ISM is a substantial source of noise, if not modeled properly, because the line of sight (LOS) from pulsar to Earth moves with respect to the medium due to motion of the endpoints and, subdominantly, motion of the medium itself (Alam et al., 2020b; Jones et al., 2017; Levin et al., 2016; Chapter, 2).

Published as J. E. Turner et al. 2023, ApJ, 944, 191

The major contributor to ISM-induced timing delays is due to frequency-dependent ($\nu^{-2}$, where $\nu$ is the observing frequency) cold plasma dispersion along the LOS. This phenomenon has been studied in great detail since the early days of pulsar timing and can largely be corrected for, although important subtleties remain (e.g. Cordes et al. (2016)). However, multi-path propagation through the inhomogeneous ISM, or scattering, results in time-variable perturbations to pulsar TOAs. The resulting delays are expected to be proportional to $\nu^{-4.4}$ for a homogeneous Kolmogorov medium (although power laws ranging from around $-2.5$ to around $-4.5$ have been reported (Bhat et al., 2004; Bansal et al., 2019; Levin et al., 2016; Chapter, 2)), and can be discerned via the delay of and structural broadening in an observed pulse. Effects of scattering, although understood theoretically and observed empirically in many high-accuracy timing programs, are not generally mitigated in major timing programs such as the NANOGrav (North American Nanohertz Observatory for Gravitational Waves) PTA and other global PTA efforts. As PTAs make their first detections and begin characterizing the low-frequency gravitational wave sky, it will be important to mitigate all possible delays. The goal of this chapter and subsequent work that we envision over the next several years is to develop effective mitigation strategies for time-variable scattering delays.

Cyclic spectroscopy (CS; Demorest (2011)) is central to our approach to this problem. CS is a powerful signal-processing technique that is already well-known and frequently used in the engineering community (Gardner, 1987; Roberts et al., 1991; Brown & Loomis, 1993; Antoni, 2007) and applicable to periodic signals such as those from pulsars. In the few studies since its introduction to pulsar timing by Demorest (2011), CS has been successful at producing high-resolution pulsar secondary spectra (Walker et al., 2013), scattering measurements using CS-enabled fine channelization (Archibald et al., 2014), and simulated recovery of the impulse response function (IRF) corresponding to a pulsar signal's passage through the ionized ISM (Palliyaguru et al., 2015). As detailed in Dolch et al. (2021), using CS to fully recover the IRF of the ISM, although a good long-term goal, has requirements, particularly signal to noise ratio (S/N), that are often not met with the current generation of radio telescopes. Here, we present a CS-derived quantity, $\tau_{\rm CS}$, obtained from CS-based recovery of the IRF, which is more highly

correlated with total scattering delay than other commonly utilized estimators. This work serves as proof of concept for the recoverability of scattering-based delays with CS, sometimes in conjunction with an autocorrelation function (ACF) estimator, addressing concerns about the accuracy of ACF-based estimators raised by authors such as Coles et al. (2010).

The organization of this chapter proceeds to a presentation of the basic theoretical framework in §4.2. Following this, we present the methodology and the results of a simulation in which we compare the effectiveness of $\tau_{\rm CS}$ to other estimators of scattering delay, specifically the widely used estimators based on the ACF of the scintillated spectrum in §4.3 and §4.4, respectively. We conclude with a discussion of future possibilities in §4.5.

## 4.2 Theoretical Basics

As is standard practice in pulsar studies, we adopt an amplitude modulated noise (AMN, Rickett (1975)) model for the pulsar signal. The electric field (single polarization) can then be represented as

$$E(t) = [p(t)n(t)] * h(t) + n_{\rm sys}(t), \tag{4.1}$$

where $p(t)$ is the original pulse profile at time $t$ mod $P$, with $P$ being the pulse period, $n(t)$ is the intrinsic modulated pulsar noise, $h(t)$ is the IRF, $n_{\rm sys}(t)$ is the noise from the sky and receiver present in the system, uncorrelated across pulse periods, and we have used the notation of Dolch et al. (2021). We choose to represent the signal as complex-valued, hence $N(t)$, $h(t)$, and $n_{\rm sys}(t)$ are complex. Additionally, we can write this electric field as

$$E(t) = E_0(t) * h(t) + n_{\rm sys}(t), \tag{4.2}$$

where which $E_0(t) = p(t)n(t)$. The corresponding frequency domain signal model is

$$\begin{aligned} E(\nu) &= [p(\nu) * N(\nu)]H(\nu) + N_{\rm sys}(\nu) && (4.3)\\ &= E_0(\nu)H(\nu) + N_{\rm sys}(\nu), && (4.4) \end{aligned}$$

where we use $E_0(\nu)$ instead of $p(\nu) * N(\nu)$ because the convolution occurs upon emission at the pulsar. $H(\nu)$, which is the Fourier transform of $h(t)$, is the transfer function (TF) of the ISM.

The resulting cyclic spectrum of $E(t)$ is

$$S_E(\nu, \alpha_k) = \langle E(\nu + \alpha_k/2)E^*(\nu - \alpha_k/2)\rangle, \tag{4.5}$$

where $\nu$ is the bandpass frequency at which the signal is measured and $\alpha_k = k/P$ is the cyclic frequency, also known as the modulation frequency, and the average is over an integer number of pulses. The cyclic spectrum is a complex-valued function with amplitude and phase for each $(\nu, \alpha_k)$ pair, and is undefined for non-periodic signals. It is important to keep in mind that, in practice, Equation 4.5 is averaged over a period of time over which the transfer function must remain unchanged, which must be less than the diffractive timescale of the ISM along a particular LOS.

If we make the assumption that a scattering delay can be seen in a pulse profile as a translation in the time domain, then as a consequence of the shift theorem of Fourier Transforms this results in a phase slope in the frequency domain. For this reason, it can be useful to examine the CS phase slope, $\phi_{\rm cyc}(\nu, \alpha_k)$, which is found via

$$\phi_{\rm cyc}(\nu, \alpha_k) = \tan^{-1}\left(\frac{\mathrm{Im}\{S_E(\nu, \alpha_k)\}}{\mathrm{Re}\{S_E(\nu, \alpha_k)\}}\right). \tag{4.6}$$

It can also be found by examining $\phi_H$, the phase of the transfer function

$$\begin{aligned}\phi_{\rm cyc}(\nu, \alpha_k) &= \phi_H(\nu + \alpha_k/2) - \phi_H(\nu - \alpha_k/2) \\ &= \alpha_k \frac{\phi_H(\nu + \alpha_k/2) - \phi_H(\nu - \alpha_k/2)}{\alpha_k}.\end{aligned} \tag{4.7}$$

Under the assumption that the cyclic frequency $\alpha_k$ is much less than the diffractive bandwidth, $\Delta\nu_{\rm d}$, we can make the approximation

$$\phi_{\rm cyc}(\nu, \alpha_k) \approx \alpha_k \frac{d\phi_H}{d\nu} = \frac{k}{P}\frac{d\phi_H}{d\nu}. \tag{4.8}$$

When the S/N is large enough, the transfer function phase can be recovered by simply integrating the CS phase,

$$\phi_H(\nu, \alpha_k) = \int \frac{\phi_{\rm cyc}(\nu, \alpha_k)}{\alpha_k} d\nu. \tag{4.9}$$

At lower S/N ratios this is not possible and more sophisticated recovery algorithms are required (Demorest, 2011; Walker et al., 2013). The transfer function amplitude for a given $\alpha_k$ can then approximated as the square root of the CS amplitude for that $\alpha_k$. Finally, the reconstructed transfer function can then be inverse Fourier transformed back into a reconstructed IRF, and the recovered scattering delay can be found by calculating the centroid of the intensity IRF,

$$\tau_{\rm CS}(\alpha_k) = \frac{\int t\ |h_{\rm CS}(t, \alpha_k)|^2 dt}{\int |h_{\rm CS}(t, \alpha_k)|^2 dt}. \tag{4.10}$$

## 4.3 Simulation Methodology

Our simulations began by creating real and imaginary components of white noise, which we call $n(t)$, and multiplying them by a complex, one-sided decaying exponential to form our IRF,

$$h(t) = {\rm Re}\{n(t)\}e^{-t/2\tau} + {\rm Im}\{n(t)\}ie^{-t/2\tau}, \tag{4.11}$$

where the length $t$ is the value in time at which the one-sided exponential is sampled. The inclusion of this amplitude-modulated white noise, which varies from realization to realization, serves to mimic how the ISM changes over the course of many observations by emulating the time-varying effects of scintillation (Narayan & Goodman, 1989). Each realization corresponds to a pattern of scintles, meaning $h(t)$ can be considered constant on scales shorter than the scintillation time. The injected value of the scattering delay for a given realization is given by

the centroid of the resulting pulsar signal, $\tau_{\rm cent}$, which can be found via

$$\tau_{\rm cent} = \frac{\int t\ |h(t)|^2 dt}{\int |h(t)|^2 dt}. \tag{4.12}$$

It is worth noting that, in real observations, scattering variations are in fact correlated with each other, since scintillation is often dominated by compact structures at a fixed or close-to-fixed angular position that moves between observations, primarily as a consequence of a pulsar's proper motion (Hill et al., 2005).

For simplicity we treat the pulse profile $p(t)$ as a delta function of height unity. This model acts as a best-case scenario pulse, removing all other factors that might interfere with our aim of solely comparing the effectiveness of various estimators at recovering a delay imparted by the ISM on radio signals of varying strengths. We appreciate that this technique would not be necessary for a true delta-like pulse, as if $p(t)$ is truly delta-like, then the IRF can also be obtained directly, as was shown using narrow pulses from PSR B1957+20, where consistent delay values have been obtained from fitting a recovered IRF and from scintillation bandwidth measurements (Main et al., 2017).

We then follow Equations 4.1-4.5, deviating only in that our noise is added only once we are in the frequency domain, to get the cyclic spectrum, an example of which can be seen Figure 4.1. Next, the cyclic spectrum phase is calculated using Equation 4.6. An example cyclic phase plot can be seen in Figure 4.2. We then calculate $\tau_{\rm CS}$ by following the methodology described after Equation 4.7 and up to Equation 4.10. An example injected and recovered IRF intensity can be seen in Figure 4.3. It is important to note that, in our simulations, $p(t)$ and $h(t)$ are identical for each pulse, while $n(t)$ and $n_{\rm sys}(t)$ are randomized. If there were significant variations of $p(t)$ beyond AMN, we suspect our method would still be accurate, although CS in general becomes decreasingly effective as $p(t)$ gets wider and S/N gets lower, which we believe are more significant factors.

In real pulsar data, the Fourier coefficients, $A_k$, of a pulse drop off at higher harmonics, with a non-scattered CS effectively being the Fourier transform of the pulse shape and more

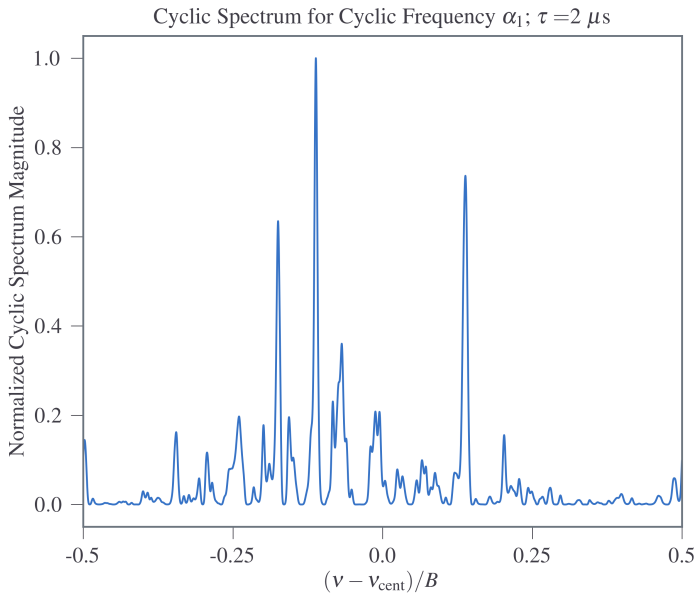


**Figure 4.1:** An example normalized cyclic spectrum as a function of the normalized bandpass taken at the cyclic frequency $\alpha_1$ for a simulated scattering delay of 2 $\mu$s using a spin period of 2 ms and a sampling interval of 100 ns. Here $\nu_{\text{cent}}$ is the center frequency of the observation and $B$ is the observing bandwidth.

or less constant in radio frequency. For this reason, we weight our transfer function at the $k^{\text{th}}$ cyclic frequency by the corresponding $k^{\text{th}}$ Fourier coefficient of a pulse with a reasonable period and width. In this simulation we chose a period of 2 ms and a width of 110 $\mu$s. This pulse width was chosen simply because it is the pulse width of PSR J1713+0747 (Manchester et al., 2013), which has a sharp pulse that can be well-approximated as a Gaussian. Effectively, our simulation is using the Fourier coefficients of a slightly faster rotating PSR J1713+0747.

The precision of the recovered delay estimation improves as we utilize more delays from higher cyclic frequencies, although the number of cyclic frequencies that have usable information depends on a number of factors, including the S/N of the pulsar signal and the pulsar duty cycle. For these simulations we make use of the first 50 cyclic frequencies in the cyclic spectra and, to calculate $\tau_{\text{CS}}$ for a given noise realization, take a weighted average of the recovered delays from these cyclic frequencies, with the weight at the $k^{\text{th}}$ cyclic frequency being the $k^{\text{th}}$ $A_k$ value of the pulsar signal mentioned above.

We then compared this estimator to the more traditional methods of recovering scattering delays, which involve calculating the ACF of a dynamic spectrum, or the intensity of the pulsar signal in both frequency and time. The changes in the intensity of the dynamic spectrum over frequency and time can create patchy features known as scintles, and the corresponding scattering delay associated with a given scintle is inversely proportional to that scintle's width in frequency. An ACF is able to pick up on a dynamic spectrum's scintillation pattern, with the width of the ACF's central peak then being relatable to the typical scintle width in that dynamic spectrum. The dynamic spectrum in the case of our delta-function pulse with unity flux at all frequencies is simply $|E(\nu)|^2$, and has the form of Equation 4.5 for $\alpha = 0$. From there,

the ACF is found by normalizing the mean-subtracted filter function cross-correlated with itself,

$$\begin{aligned}\mathrm{ACF}(\nu) = &\left[\sum_{\nu}\left(|E(\nu)|^2 - \overline{|E(\nu)|^2}\right)\right. \\ &\left.\times\left(|E(\nu+\Delta\nu)|^2 - \overline{|E(\nu+\Delta\nu)|^2}\right)\right] \\ &\div \mathrm{Max}\left[\sum_{\nu}\left(|E(\nu)|^2 - \overline{|E(\nu)|^2}\right)\right. \\ &\left.\times\left(|E(\nu+\Delta\nu)|^2 - \overline{|E(\nu+\Delta\nu)|^2}\right)\right], \end{aligned} \tag{4.13}$$

where the horizontal bar indicates we are taking the average.

The ACFs were then fit with both a Gaussian and Lorentzian distribution, and the scattering delay was found via

$$2\pi\Delta\nu_{\mathrm{d}}\tau = C_1, \tag{4.14}$$

where $\Delta\nu_{\mathrm{d}}$ is the scintillation bandwidth, defined as the half-width at half-maximum of the ACF along the frequency axis, and $C_1$ is a dimensionless quantity ranging from $0.6-1.5$ conditional on the geometry and spectrum of the electron density fluctuations of the medium (Cordes & Rickett, 1998). In this analysis we assume $C_1 = 1$. Mathematically, using the Lorentzian to fit the ACF makes more sense because the Lorentzian distribution is the square of the Fourier transform of the one-sided decaying exponential (Cordes et al., 1985), although Gaussian distributions are close approximations that have been used in a number of scintillation studies (Bhat et al., 1999a; Wang et al., 2005; Levin et al., 2016; Chapter, 2). An example ACF fit with both Lorentzian and Gaussian distributions is shown in Figure 4.4.

## 4.4 Simulation Results

Our main simulation consisted of 1000 random noise draws for a $\tau$ of 2 $\mu$s using 20,000 time samples, $n_{\mathrm{samp}}$, and a sampling interval, $s_{\mathrm{int}}$, of 100 ns, corresponding to $P = 2$ ms. Here,

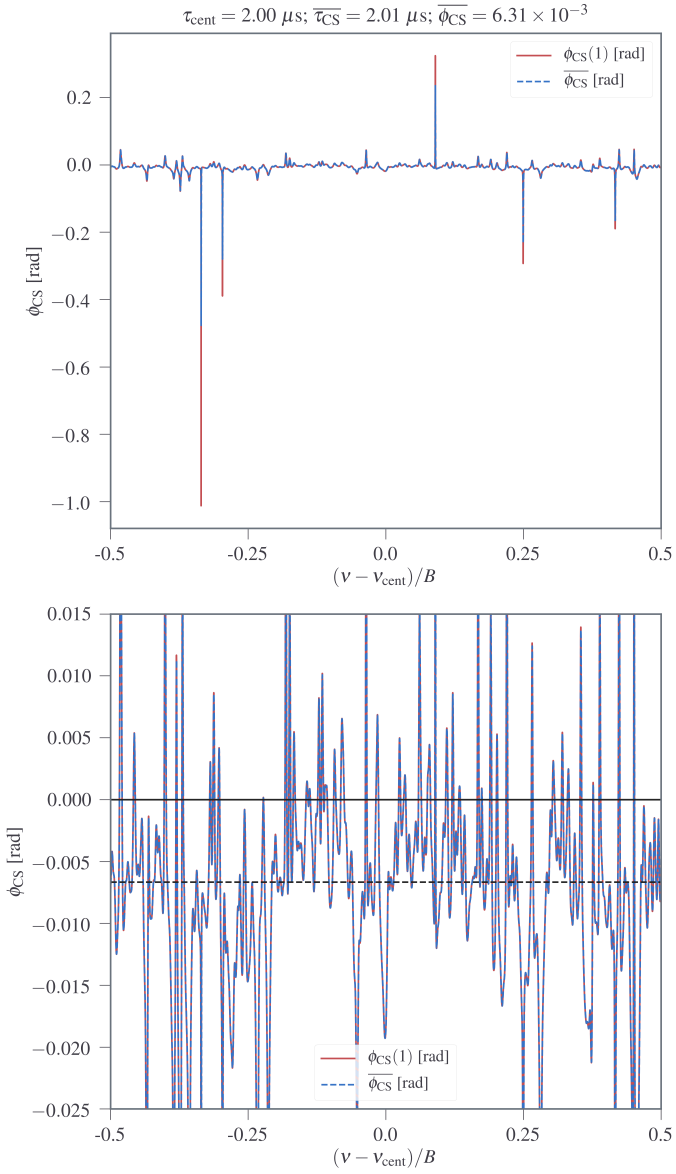


**Figure 4.2:** (Top) An example cyclic phase as a function of the normalized bandpass taken at the cyclic frequency $\alpha_1$ (red) as well as using the weighed average of the first 50 cyclic frequencies (dashed blue) for a simulated scattering delay of 2 $\mu$s using a spin period of 2 ms and a sampling interval of 100 ns, corresponding to $P = 2$ ms. (Bottom) A zoomed in version of the top plot to better visualize structure. The dashed black line indicates the average cyclic spectrum phase, while the solid black line indicates a phase of zero. As seen in the top figure, the phase only utilizing the first cyclic frequency has much more extreme outliers. In fact, over many noise realizations at a S/N of 10, weighted average cyclic phases using 50 cyclic frequencies typically exhibit around 79% smaller standard deviations compared to just the phase at the first cyclic frequency.

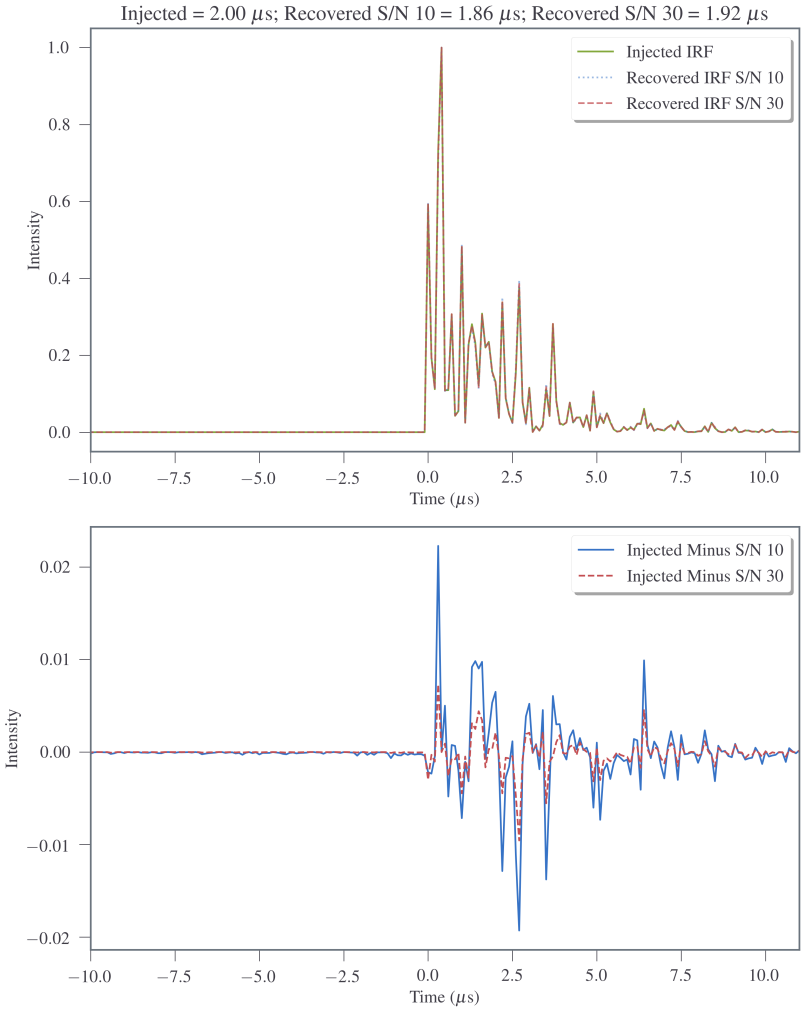


**Figure 4.3:** (Top) An example injected IRF intensity prior to the inclusion of additive noise and the corresponding recovered IRF intensities using information from only the first cyclic frequency using a S/N of 10 and 30. (Bottom) Differences between the noiseless injected IRF intensity and recovered IRF intensities at a S/N of 10 and 30. Despite recovering the IRF quite well at these S/N, small differences between the injected and recovered IRF intensities can lead to noticeable differences in the recovered delay.

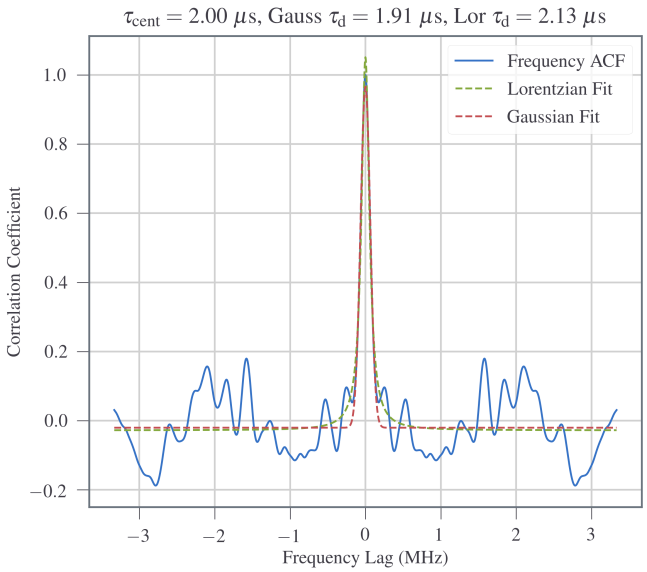


**Figure 4.4:** The frequency ACF (blue) of a dynamic spectrum for a scattering delay of 2 $\mu$s. Green and red dotted lines correspond to fits to the ACF using Lorentzian and Gaussian distributions, respectively. Delays in the title correspond, from left to right, to injected $\tau_{cent}$ delay, the Gaussian ACF estimator, and the Lorentzian ACF estimator.

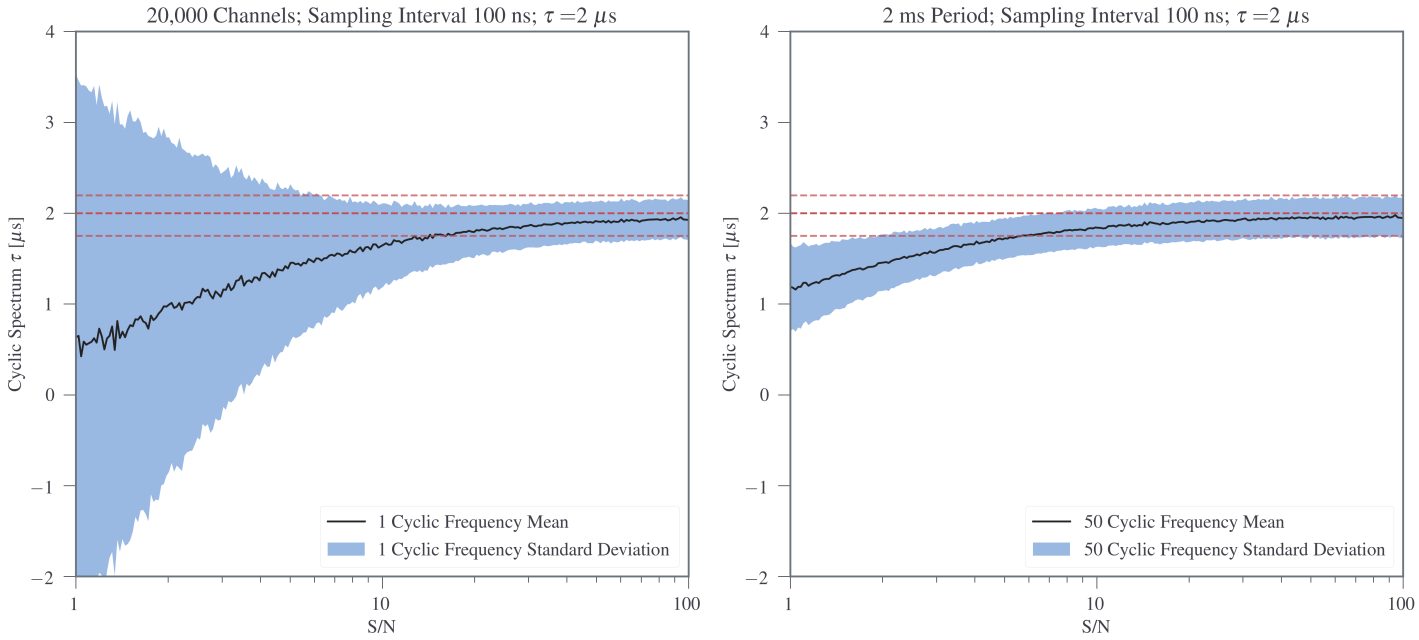


**Figure 4.5:** Cyclic spectrum estimator simulation results for random noise draws for a $\tau$ of 2 $\mu$s for 300 values of S/N using a spin period of 2 ms and a sampling interval of 100 ns using one (left) and 50 (right) cyclic frequencies. The dashed red lines represent the mean plus or minus one standard deviation of the injected $\tau$ at each S/N, with the mean and standard deviation of the recovered values at each epoch shown in black and light blue, respectively.

$n_{\mathrm{samp}}$ refers to phase bins rather than baseband voltage samples. This framework assumes we are using baseband data recording with a bandwidth of 10 MHz. For larger bandwidths on the order of hundreds of MHz, individual scintles get progressively wider at higher frequencies, which other studies have compensated for by "stretching" the entire dynamic spectrum (Levin et al., 2016; Chapter, 2). In these studies, the spectrum is scaled by $\nu^{-\beta}$, with $\beta$ being the scattering scaling index determined for a given pulsar's LOS, relative to the center frequency to give all scintles approximately equal width across the band. This small 10 MHz bandwidth was chosen to avoid the scintle stretching that would be required at larger bandwidths. Additionally, this bandwidth and scattering delay combination results in a similar number of scintles on average across the band as is seen for many NANOGrav pulsars (Chapter, 2), meaning that we have approximately the same amount of data informing our ACFs, and consequently similar precision for a comparable S/N. This series of 1000 random noise draws was repeated over 300 different values of S/N ranging from around 0.3 to 100, with the S/N defined as the square of the inverse of the standard deviation of $N_{\mathrm{sys}}(t)$, since our transfer functions are normalized prior to noise being added.

The results of these simulations using the cyclic spectrum and Lorentzian and Gaussian ACF estimators for the recovery of $\tau$ are shown in Figures 4.5, 4.6, respectively. The cyclic spectrum estimator using 50 cyclic frequencies appears to converge to a stably recovered value of $\tau$ at a S/N around 100, while the two ACF estimators have already converged at the lowest S/N in our simulation, which may imply that, given sufficient frequency resolution, there appears to be a range of lower S/N where these estimators are superior to the cyclic spectrum estimator.

In fact, the lack of improvement in the ACF estimators demonstrates that good frequency resolution, specifically the ratio of the scintillation bandwidth to the overall observing bandwidth, and consequently, the total number of scintles across the observing band, is much more important than S/N for accurate ACF estimator recovery. This effect, known as the finite

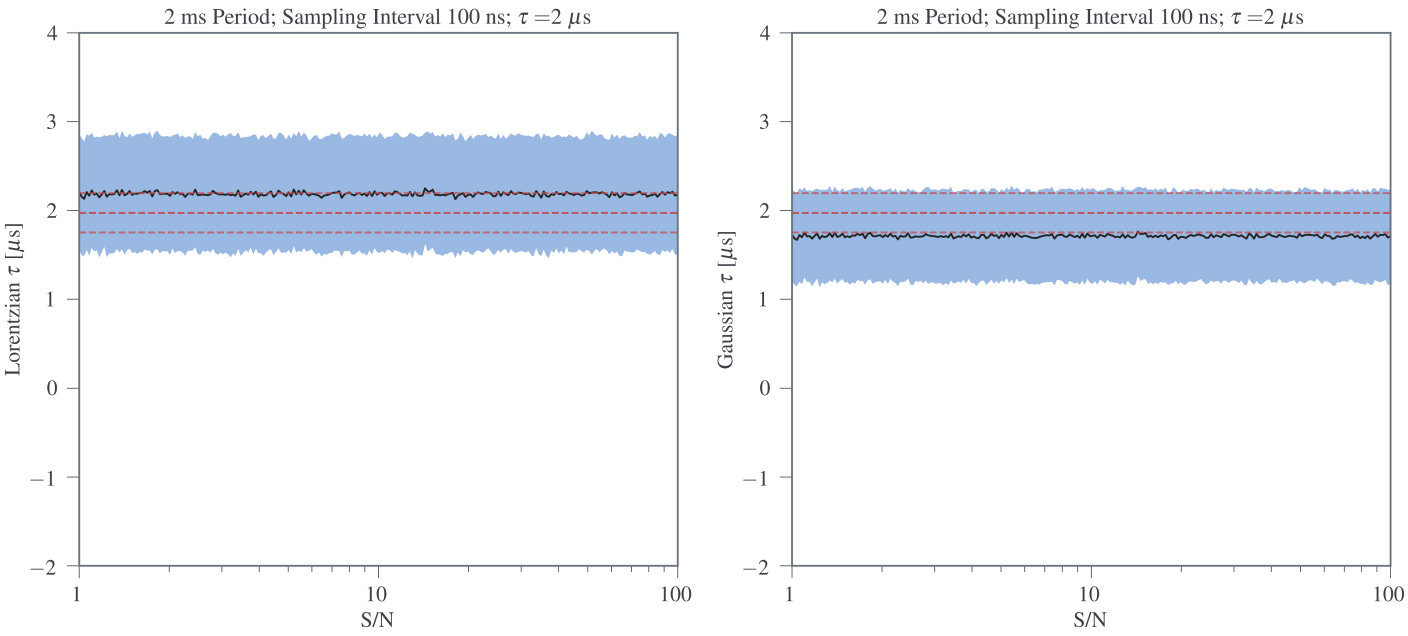


**Figure 4.6:** Lorentzian (left) and Gaussian (right) ACF estimator simulation results for random noise draws for a $\tau$ of 2 $\mu$s for 300 values of S/N using a spin period of 2 ms and a sampling interval of 100 ns. The dashed red lines represent the mean plus or minus one standard deviation of the injected $\tau$ at each S/N, with the mean and standard deviation of the recovered values at each epoch shown in black and light blue, respectively.

scintle error, can be determined via

$$\begin{aligned}\epsilon &\approx \tau_{\rm d} N_{\rm scint}^{-1/2} \\ &\approx \tau_{\rm d}[(1+\eta_{\rm t} T/\Delta t_{\rm d})(1+\eta_\nu B/\Delta\nu_{\rm d})]^{-1/2},\end{aligned} \tag{4.15}$$

where $N_{\rm scint}$ is the number of scintles in the dynamic spectrum, $T$ and $B$ are total integration time and total bandwidth, respectively, $\Delta t_{\rm d}$ is the scintillation timescale, defined as the half-width at $e^{-1}$ of the dynamic spectrum's ACF along the time axis, and $\eta_{\rm t}$ and $\eta_\nu$ are filling factors ranging from 0.1 to 0.3 depending on the definitions of characteristic timescale and scintillation bandwidth, and in our case both set to 0.2 (Cordes, 1986b). Since scattering delays only depend on the scintillation bandwidth, the scintillation timescale is not important for these simulations. As a result, for simplicity, we can assume these simulated observations had observing times much less than the scintillation timescale, and so Equation 5.4 can be reduced to

$$\epsilon \approx \tau_{\rm d}(1+\eta_\nu B/\Delta\nu_{\rm d})^{-1/2}. \tag{4.16}$$

Taking the results of a typical 1000 sample run, we find that the average Lorentzian delay spread is around 0.66 $\mu$s and the average Gaussian delay spread is around 0.52 $\mu$s, while the average Lorentzian finite scintle error is around 0.40 $\mu$s and the average Gaussian finite scintle error is around 0.36 $\mu$s. Further, we did a series of tests in which we varied the sampling interval, hence the bandwidth, of the simulation. These tests verified that the spread of ACF values follows the $B^{-1/2}$ scaling of Equation 4.16 in the many-scintle regime.

This limitation on the effectiveness of estimation ACF-based techniques also means that methods such as those demonstrated by Hemberger & Stinebring (2008b), which estimate scattering delays by integrating along the differential delay axis of the secondary spectrum, will face the same constraints. Other non-CS techniques do exist to reconstruct the IRF, such as interstellar holography demonstrated by Walker et al. (2008), although this particular technique requires a high S/N. Our simulations have shown that an IRF recovery approach based on CS, albeit one that uses a simple, non-iterative phase reconstruction, is quite effective at moderate

S/N. That being said, future work will be required to fully evaluate the relative merits of these different approaches.

Figures 4.5 and 4.6 also show that all three estimators converge to roughly the correct value, although there are slight biases in the mean values for the ACF estimators, whereas none is seen for the cyclic spectrum estimator. Additionally, for an ideal estimator, at sufficiently high S/N the standard deviation in the recovered delays should end up matching the standard deviation in the injected $\tau_{\text{cent}}$ delays, which we see only in the cyclic spectrum estimator. For reasons that will be discussed later, we do not believe that the biases in the ACF estimators are simply an indicator that a different $C_1$ should be used for our choice of impulse response.

A significant difference is also noticeable in the mean and standard deviation at low S/N between using only one cyclic frequency and using 50 cyclic frequencies. While the single cyclic frequency estimator appears to converge at a similar, if not slightly higher, S/N, its standard deviation is still significantly larger than the 50 cyclic frequency estimator at lower S/N. Overall, this presents a strong argument that using many cyclic frequencies is superior.

The extreme variability seen at low S/N in the one cyclic frequency cyclic spectrum estimator, and the trend toward average recovered delays around zero $\mu$s in both cyclic spectrum estimators, is the result of the white noise overwhelming an IRF that has both positive and negative components, resulting in a signal that is on average centered around zero on the time axis. As the IRF becomes more discernible from the additive white noise at higher S/N, a signal that is increasingly centered in a positive region on the time axis is recovered, resulting in positive recovered delay values.

On a related note, if our ACF estimators did not have sufficient frequency resolution at lower S/N, the excess noise would have resulted in scintles appearing narrower and therefore yielding higher measured scattering delays, leading to the ACF estimators being biased high in addition to having large variability. This high bias is also a consequence of ACF fitting always producing a positive definite value, whereas the cyclic spectrum estimator's ability to return both positive and negative values results in more manageable behavior at low S/N.

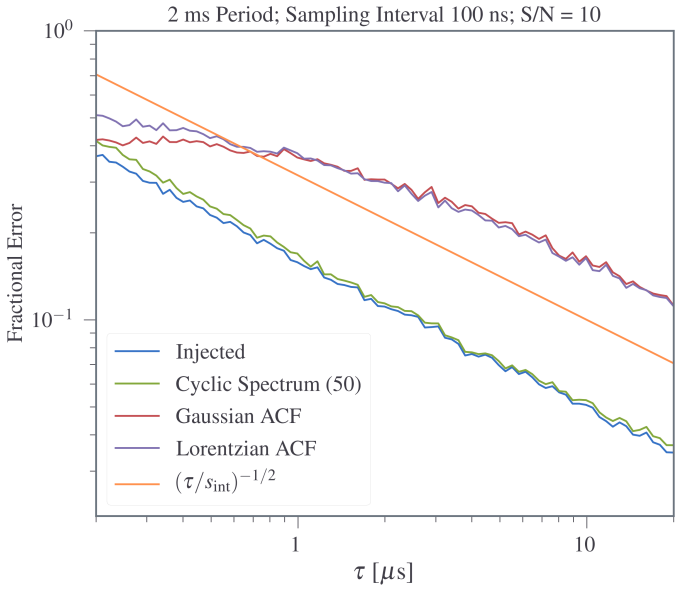


**Figure 4.7:** The fractional error of the recovered delay for 100 values of $\tau$ with a sampling interval $s_{\text{int}}$ of 100 ns using a spin period of 2 ms with 50 cyclic frequencies at a S/N of 10. The fractional error scales as the inverse square root of the number of scintles across the observing band for a typical observation, or, equivalently, the inverse square root of the delay divided by the sampling interval. Throughout much of the abscissa range, the cyclic spectrum estimator has a fractional error approximately 64% smaller than that of the ACF estimators. ACF estimators can be seen to flatten out in the smaller delay-to-sampling interval ratio regime as they are no longer able to detect a signal above the noise. The improvement in precision as the delay gets larger while maintaining this sampling interval demonstrates the benefits of proposed wider bandwidth observing programs.

Supplemental simulations also show that, after reaching a sufficient S/N, additional gains in precision for all estimators are also partially limited by the ratio of the delay to the sampling interval, regardless of the number of time samples in use. This is under the assumption that we are already using a sufficient number of time samples such that accurate scattering estimations are possible. As shown in Figure 4.7, when we run our simulation at a S/N of 10 at various values of delay with a constant sampling interval of 100 ns, we find a significant improvement in our fractional error (or in this case, the standard deviation of the recovered

values divided by delay) as the delay-to-sampling interval ratio increases, following an inverse square root power law for all estimators. This quantity is also equivalent to the inverse square root of the number of scintles across the observing band for a typical observation. Since both the number of scintles across the observing band and the sampling interval are inherently tied to the maximum possible bandwidth we can utilize, i.e., the inverse of the sampling interval, these results provide strong support for the introduction of ultra wideband (UWB) observation programs.

In addition to examining the precision and accuracy over many realizations, we also looked at how this behavior tracked over individual realizations. A typical example of this at a S/N of 10 can seen in Figure 4.8, where we show every 20th realization of the simulation for visual ease. While all three estimators generally follow the injected delays, the cyclic spectrum estimator clearly tracks these injected values much better than the ACF estimators.

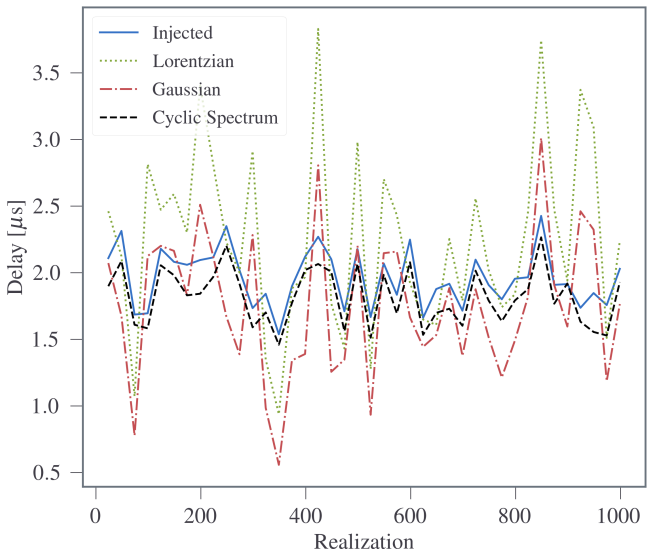


**Figure 4.8:** A sample of realizations for a S/N of 10 for the simulation described above. The accuracy of the different estimators compared to the injected value found by $\tau_{\text{cent}}$ follows the behavior seen in Figures 4.5, and 4.6.

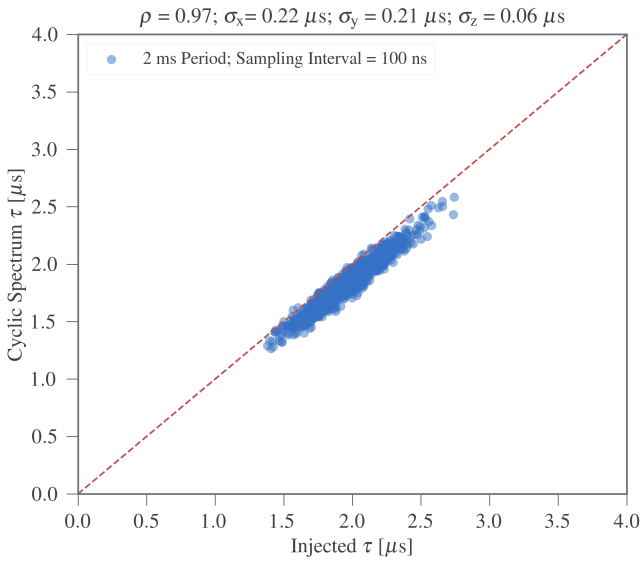


**(a)** Cyclic spectrum estimator using 50 cyclic frequencies. The slight offset from the line of equality is expected at a S/N of 10, as our 50 cyclic frequency CS results in Figure 4.5 were not fully converged at this S/N.

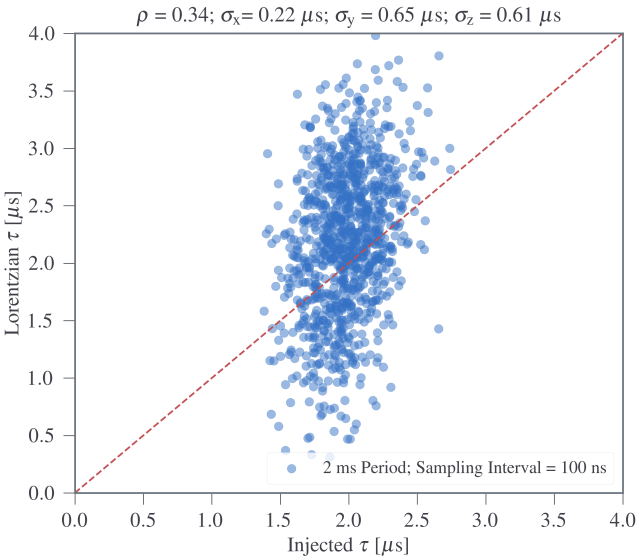


**(b)** Lorentzian ACF estimator

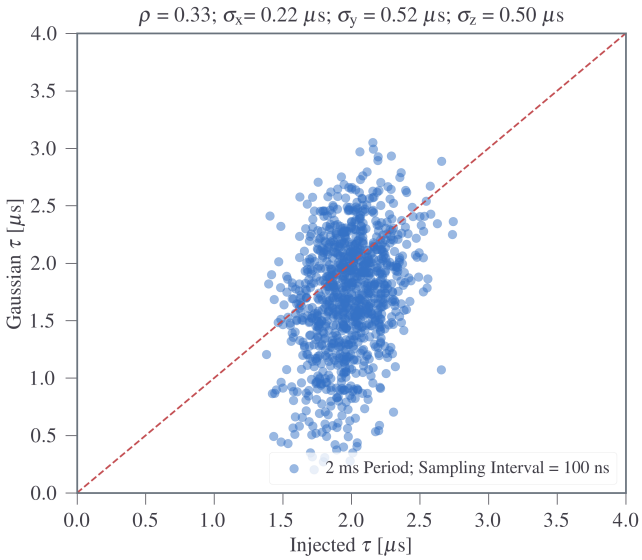


**(c)** Gaussian ACF estimator

**Figure 4.9:** Estimators vs injected delay for 1000 random noise draws for a $\tau$ of 2 $\mu$s using a spin period of 2 ms and a sampling interval of 100 ns at a S/N of 10. $\sigma_x$ is the standard deviation of the data in the $x$ direction, $\sigma_y$ is the spread of the data in the $y$ direction, and $\sigma_z$ is the standard deviation of $z = y - x$. Dashed red lines represent lines of equality between the two axes.

These discrepancies become even clearer when we examine how well individual draws correlate between the injected delay and the various estimators for a given S/N. As shown in Figure 4.9, while there is nearly a one-to-one correspondence between the injected delay and the cyclic spectrum estimator, epoch-to-epoch variations for the ACF estimators are both significantly larger. In these plots $\rho$ represents the correlation coefficient between the two variables, $\sigma_x$ is the standard deviation of the data in the $x$ direction, $\sigma_y$ is the spread of the data in the $y$ direction, and $\sigma_z$ is the standard deviation of $z = y - x$. Additionally, the $\sigma_y$ and $\sigma_z$ values for the ACF estimators are much more similar to each other than to the cyclic spectrum estimator. Larger $\sigma_z$ indicates a larger typical difference between the injected delay and the estimator for a given noise realization.

The lack of correlation seen in the ACF estimator plots in Figure 4.9 also present a strong argument against the ACF estimator biases seen in Figure 4.6 simply being an indication that a different $C_1$ should be used for our choice of impulse response, as just choosing a $C_1$ that removes the bias in Figure 4.6 would not alter the lack of correlation seen in Figure 4.9. The $C_1$ would also have to be different for each ACF approach, since the biases are in opposite directions relative to the injected delay. Additionally, attempting to retroactively find $C_1$ by comparing the ratios of the injected delays and ACF-recovered delays in Figure 4.9 shows significant variation among individual realizations in a recovered purported $C_1$.

We can also compare how these correlation coefficients change as a function of S/N. For each S/N value, we calculated the correlation coefficients for each estimator over the 1000 random draws. The results are shown in Figures 4.10 and 4.11. As with Figures 4.5 and 4.6, we see the cyclic spectrum estimator eventually converge whereas the ACF estimators have already converged. The convergence in the ACF plots, like in Figure 4.6, are the result of already having sufficient frequency resolution and a sufficient number of scintles over our S/N range, as once the scintle structure in the dynamic spectrum has been resolved, further improvements in S/N will not affect an ACF estimator's ability to recover scattering delays. For the cyclic spectrum estimator, the S/N where it plateaus corresponds well with what is seen in Figure 4.5. Significantly, the cyclic spectrum correlation plateaus at a much higher value than the ACF

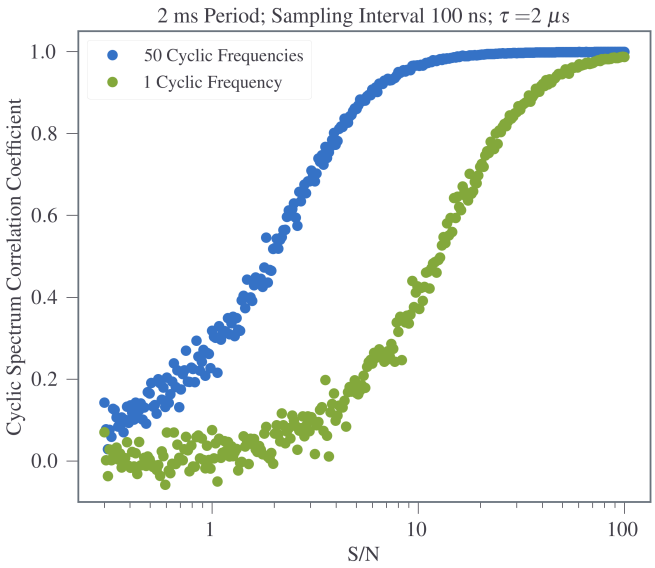


**Figure 4.10:** Cyclic spectrum estimator correlation coefficients for random noise draws for a $\tau$ of 2 $\mu$s for 300 values of S/N using a spin period of 2 ms and a sampling interval of 100 ns.

estimators (around 1.0 compared to around 0.25−0.45). This behavior further indicates the improvement the cyclic spectrum estimator provides over the ACF estimators. Additionally, our 50 cyclic frequency estimator converges at a S/N around an order of magnitude earlier than the single cyclic frequency estimator, further emphasizing the benefits of utilizing multiple cyclic frequencies.

We also examined how much these estimators deviate from $\tau_{\text{cent}}$ as we vary the injected scattering delay. To do this, we repeated the simulation described at the beginning of this section for 45 scattering delays ranging from 0.1−2 $\mu$s spaced apart evenly in log space at a S/N of 10. The delay range was chosen based on the breadth of delays we might expect to see from observing many PTA-quality pulsars. We then compared $|z|$, the differences between the estimators and $\tau_{\text{cent}}$, over each delay in that range. The results are shown in Figure 4.12. While at the lowest delays for this sampling interval the Gaussian estimator has greater accuracy than the Lorentzian estimator, at higher delays both the Lorentzian and cyclic spectrum estimators

are noticeably more accurate than the Gaussian estimator, which is shown to deviate from $\tau_{\rm cent}$ more significantly as the injected delay increases.

## 4.5 Conclusions and Future Developments

We simulated scattering delays from the ISM to test the effectiveness of three delay estimators: fitting Lorentzian and Gaussian distributions to frequency ACFs calculated from pulsar dynamic spectra to recover the scintillation bandwidth and the cyclic spectrum-derived quantity $\tau_{\rm CS}$. We find that, at sufficient S/N, in terms of both precision and accuracy, the cyclic spectrum estimator is superior to both ACF estimators, which are accurate over many realizations, but not as reliable as the cyclic spectrum estimator on an epoch-to-epoch basis. Importantly, for actual pulsar timing with additional sources of timing noise, ACF and CS estimators are necessary to discriminate between ISM-based propagation delays and other sources of delay. We believe the results described in this paper provide significant motivation for further pursuing CS implementation in general, especially through the lens of deconvolution-based IRF recovery.

As PTAs close in on sensitivities sufficient for detecting gravitational waves, understanding and mitigating all non-gravitational wave delays will be critical for accurate gravitational wave characterization. Many pulsars in the NANOGrav PTA are already known to have scattering delays of 10s of nanoseconds, which is a non-negligible fraction of the $\mu$s to sub-$\mu$s residuals we see in many pulsars (Alam et al., 2020b). Many of these estimations, and indeed many estimations of scattering delays in millisecond pulsars, have been performed by fitting Gaussian functions to ACFs, indicating the true effects of scattering delays in PTAs may currently be improperly estimated by a few percent, although additional efforts within NANOGrav are currently in place to estimate scattering delays by fitting $\nu^{-4}$ delays to output TOAs. Additionally, these effects are not currently accounted for in NANOGrav's timing pipeline, or the pipelines of other PTAs such as the European Pulsar Timing Array (EPTA), Parkes Pulsar Timing Array (PPTA), or, consequently, the global pulsar timing array effort, the International

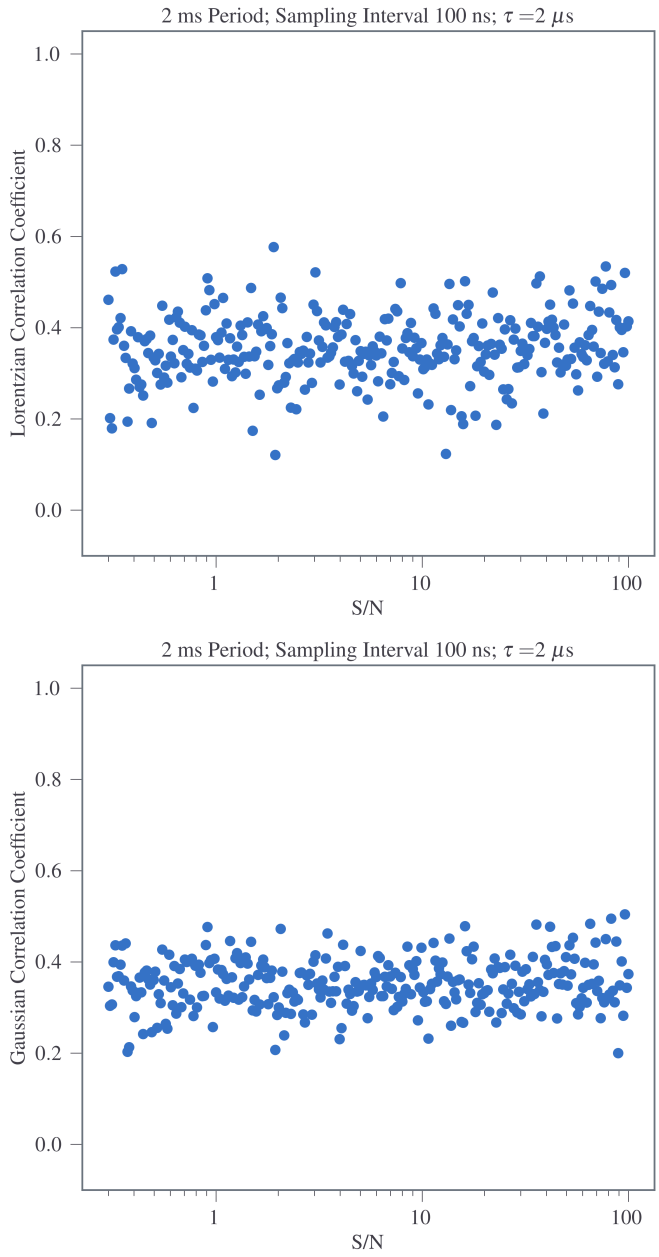


**Figure 4.11:** Lorentzian (top) and Gaussian (bottom) ACF estimator correlation coefficients for random noise draws for a $\tau$ of 2 $\mu$s for 300 values of S/N using a spin period of 2 ms and a sampling interval of 100 ns.

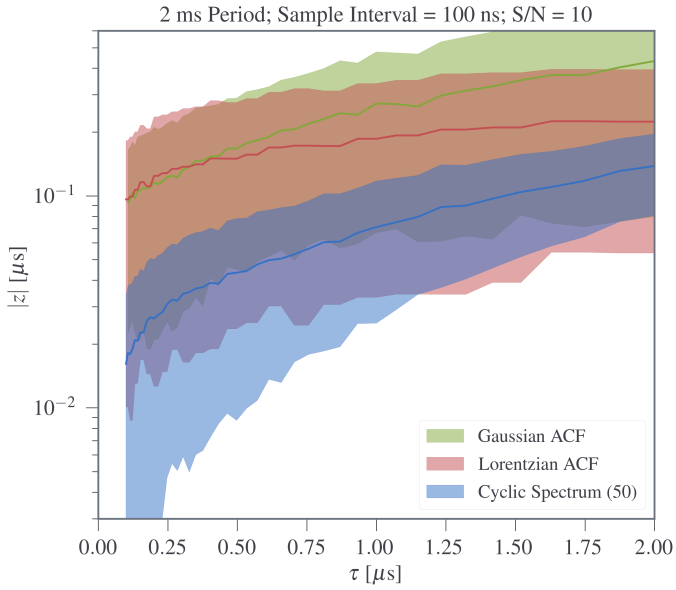


**Figure 4.12:** Absolute differences, $|z|$, between the various estimators and $\tau_{\text{cent}}$ as a function of the average injected scattering delay, $\tau$. For each of the three curves, the solid line indicates the mean value and the shaded region indicates the 1-$\sigma$ error range.

Pulsar Timing Array (IPTA), furthering the need for more accurate techniques such as cyclic spectroscopy to be both developed and implemented into future pulsar timing efforts. Efforts are currently ongoing to implement a real-time cyclic spectroscopy backend into existing timing pipelines with the goal of removing scattering effects before any further timing analysis has taken place. This work is currently being done on pipelines operating at the Green Bank Telescope, currently the primary observing site for NANOGrav, but may be implemented in the future at other NANOGrav telescopes such as CHIME and VLA or next-generation telescopes such as DSA-2000 should this endeavor prove successful.

This material is based upon work supported by the Green Bank Observatory which is a major facility funded by the National Science Foundation operated by Associated Universities, Inc. We gratefully acknowledge support of this effort from the NSF Physics Frontiers Cen-

ter grants 1430284 and 2020265 to NANOGrav. DRS acknowledges support from NSF grant 2009759. TD is supported by an NSF Astronomy and Astrophysics Grant (AAG) award number 2009468. Some of the simulations in this work utilized the resources of the Bowser & Link computing clusters at West Virginia University.

*Software*: SCIPY Virtanen et al. (2020), NUMPY van der Walt et al. (2011), and MATPLOTLIB Hunter (2007).

# Chapter 5. A Cyclic Spectroscopy-Aided Scintillation Study of Multi-Hour L-Band Observations of PSR B1937+21

# I. Intra-Epoch Frequency Evolution

## 5.1 Introduction

Pulsar scintillation is one of the most valuable tools we have for understanding the small scale structure of the ionized interstellar medium (ISM), while also acting as a significant source of noise in pulsar timing efforts. In many cases, gaining a better understanding of the former can lead to better mitigation efforts of the latter. It is also crucial to understand the frequency dependence of propagation through the ISM, as the effects seen in pulsar scintillation evolve with these frequencies.

As a consequence of interactions between interactions between pulsar emission and free electrons along the signal's propagation path, which we approximate as occurring at an infinite or finite thin screen around halfway between the pulsar and the observer, the emission will experience multipath propagation and its image will undergo angular broadening, resulting in interference between out-of-phase photons at our telescope and a broadening of the observed pulsar signal (Lorimer & Kramer, 2004). The effects of this interference can be seen in pulsar dynamic spectra, which track the intensity of the observed signal over frequency and time. The width of bright patches in these spectra, known as scintles, provide insight into the rapidity of these intensity fluctuations and therefore a means to quantify the level of scattering and the

In prep to be submitted to ApJ as J. E. Turner et al. 2023

corresponding arrival time delay a given pulse may experience. Additionally, if the broadened pulse can be deconvolved into the intrinsic pulsar signal and the impulse response function (IRF) of the ISM, the signal imparted by the ISM onto the pulse as a result of their interaction, fitting this IRF to an exponential decay function provides another way to quantify the level of scattering present in an observation. These delays, $\tau_{\rm d}$, are expected to scale as $\nu^{-4.4}$ under the assumptions that the ISM can be accurately characterized by Kolmogorov turbulence and that the subinertial part of the wavenumber spectrum dominates (Cordes & Rickett, 1998).

Additional information can be gained about the structure of the ISM along a given line of sight (LOS) by examining the secondary spectrum of an observation, where interference patterns in the dynamic spectrum can give rise to parabolic structures known scintillation arcs (Stinebring et al., 2001c), whose curvature, in conjunction with the pulsar's effective velocity, $\mathbf{V}_{\rm eff,\perp}$, and distance, can be used to determine the location of the corresponding scattering screen along the LOS. Structures within these arcs can also be used to gain insight into the structure of the scattering region (Hill et al., 2005). Under the assumption that pulsar scattering occurs at a thin screen, the arc curvatures are expected to scale with frequency as $\nu^{-2}$ (Hill et al., 2003b).

For many highly scattered pulsars, for which information about scattering effects are the most pertinent for mitigation in pulsar timing efforts and whose LOS's through the ISM are often the most interesting, observations that use filterbanks and incoherent dedispersion lack the filterbank channel resolution necessary to see scintillation structures within their dynamic spectra, particularly at L-band where wider bandwidths are typically used, leaving observers unable to effectively quantify the level of scattering present or resolve scintillation arcs. However, there exist techniques that can take advantage of the periodic and amplitude-modulated nature of the pulsar signal to drastically improve the resolution of baseband observations. Cyclic spectroscopy, used for years within various engineering communities, was first introduced to pulsar timing in Demorest (2011), where the technique made use of the phase information in the voltage data and exploited the fact that the scintillation time spans many pulse periods, allowing the impulse response of the multipath propagation to be estimated. The cyclic spectrum is

defined as

$$S_E(\nu, \alpha_k) = \langle H(\nu + \alpha_k/2) H^*(\nu - \alpha_k/2) \rangle S_x(\nu, \alpha_k), \tag{5.1}$$

where $H(\nu)$ is the transfer function of the ISM, also known as the Fourier transform of the ISM IRF, $\alpha_k = k/P$ is the cyclic frequency at the $k^{\text{th}}$ harmonic for pulse period $P$, and $S_x(\nu, \alpha_k)$ is the Fourier transform of the intrinsic pulse profile (Dolch et al., 2021), and be found by taking the 2D Fourier transform of the periodic spectrum in a cyclic spectroscopy-processed observation.

As a result of the additional information made available in the pulsar signal through this technique, while maintaining a given number of pulse phase bins, one can acquire significantly higher frequency resolution than accessible through the use of traditional filterbank channels, allowing for the emergence of previously unresolved features in periodic and dynamic spectra while maintaining high pulse phase resolution. This resolution improvement has already been used to great effect in low-frequency millisecond pulsar (MSP) observations (Walker et al., 2013; Archibald et al., 2014) and could hypothetically lead to PTAs where scintles and scintillation arcs (assuming observing times where scintillation timescales are obtainable) are resolved in all epochs. This would allow for scintillation arcs to be studied with preexisting high-cadence observations using many pulsars utilizing the wide bandwidths required for high timing sensitivity without the need to alter the observing parameters crucial to PTA feasibility, and providing many lines of sight through the ISM over which to examine arc evolution over frequency and time.

Additionally, this scintle resolution would make it possible for scattering delays to be estimated in all epochs, provided flux density is sufficient for visible scintles in dynamic spectra. This would provide a compelling case for the inclusion of scattering delays in pulsar timing models used by PTAs, as, while PTAs monitor these delays over time, many do not account for them in timing models, resulting in a noise floor of tens to hundreds of nanoseconds at L-band depending on the pulsar, and even higher at lower observing frequencies (Chapter, 2). There are attempts within PTAs to indirectly account for the effects of scattering, such as fitting

$\nu^{-4}$ delays to output TOAs, although this approach ignores that different scaling indices have been observed across many lines of sight and that indicies within single lines of sight appear to vary slightly from epoch to epoch, which could result in improper correction of these scattering effects and thus introducing unnecessary noise into PTA data (Chapter, 2).

The ideal situation when performing frequency-dependent analyses of pulsar propagation through the ISM is to obtain all measurements at the various frequencies simultaneously so that the same LOS is being sampled in throughout. Typically when frequency-dependent analyses are performed, they are limited by the frequency resolution and bandwidth of the observations, as well as the observing cadence. Some of these analyses used a large frequency range, but only $2-4$ measurements (Bhat et al., 2004), with these measurements sometimes taken on different days (Hill et al., 2003b; Liu et al., 2022), which should not generally affect results provided they were taken with in a pulsar's refractive timescale and the effective velocity remains similar over the course of the observations. Other methods make simultaneous measurements across many frequencies, with some breaking up those observations into smaller frequency slices for additional robustness (Krishnakumar et al. (2019); Chapter 3), although all such studies have been performed at lower frequency ranges (Archibald et al., 2014; Bansal et al., 2019). Studies in L-band have taken the approach of breaking up large bandwidth observations into smaller frequency slices as well, although this appears to have been limited to 200 MHz slices across 800 MHz bands (Levin et al., 2016; Chapter, 2).

In this chapter we used cyclic spectroscopy to acquire fine-frequency resolution across a relatively small bandwidth, allowing for eight simultaneous measurements per epoch for frequency-dependent analyses. In Section 5.2 we briefly discuss the data used for this work. In Section 5.3 we discuss the data processing and analyses performed on these data. Section 5.4 discusses the results of these analyses and their comparison to theory and previous literature. Finally, in Section 5.5 we discuss our conclusions and the potential for future work that can take full advantage of the cyclic spectroscopy techniques discussed in this work.

## 5.2 Data

Our observations (P2627 PI Dolch) took place on MJDs (and fractional years) 56183 (2012.70), 56198 (2012.74), and 56206 (2013.01). They spanned approximately 2.5 hours each and were taken in baseband mode with the FPGA-based PUPPI spectrometer at the Arecibo Observatory using 200 MHz of bandwidth with 6.25 MHz wide filterbank channels centered at 1373.125 MHz using standard NANOGrav observing methods (Arzoumanian et al., 2015a). Our raw baseband data were then processed via cyclic spectroscopy using `dspsr`[1] (van Straten & Bailes, 2011) with 1024 pulse phase bins and 1024 cyclic channels per filterbank channel, for a final channel resolution of around 6.1 kHz. Originally the data were taken in 170 second subintegrations, although we later resampled into 10 and 30 second subintegrations for our analyses using the "-L" flag in DSPSR. An example dynamic spectrum processed traditionally from this baseband data compared with the same spectrum processed with cyclic spectroscopy is shown in Figure 5.1.

## 5.3 Analyses

To examine the frequency dependence of the scintillations we divided the total band into eight 25 MHz wide subbands, which are wide enough to contain a large number of narrow scintles. This frequency slice size was chosen to allow for a high degree of robustness in our analyses while limiting the effects of both the finite scintle effect and the filterbank gaps. In all observations, each frequency slice had its two hands of polarization summed and had its dynamic spectrum recovered by determining the intensity, $S$, of the pulsar signal at each observing frequency, $\nu$, and time, $t$, using

$$S(\nu, t) = \frac{P_{\rm on}(\nu, t) - P_{\rm off}(\nu, t)}{P_{\rm bandpass}(\nu, t)}, \tag{5.2}$$

[1] `http://dspsr.sourceforge.net/`

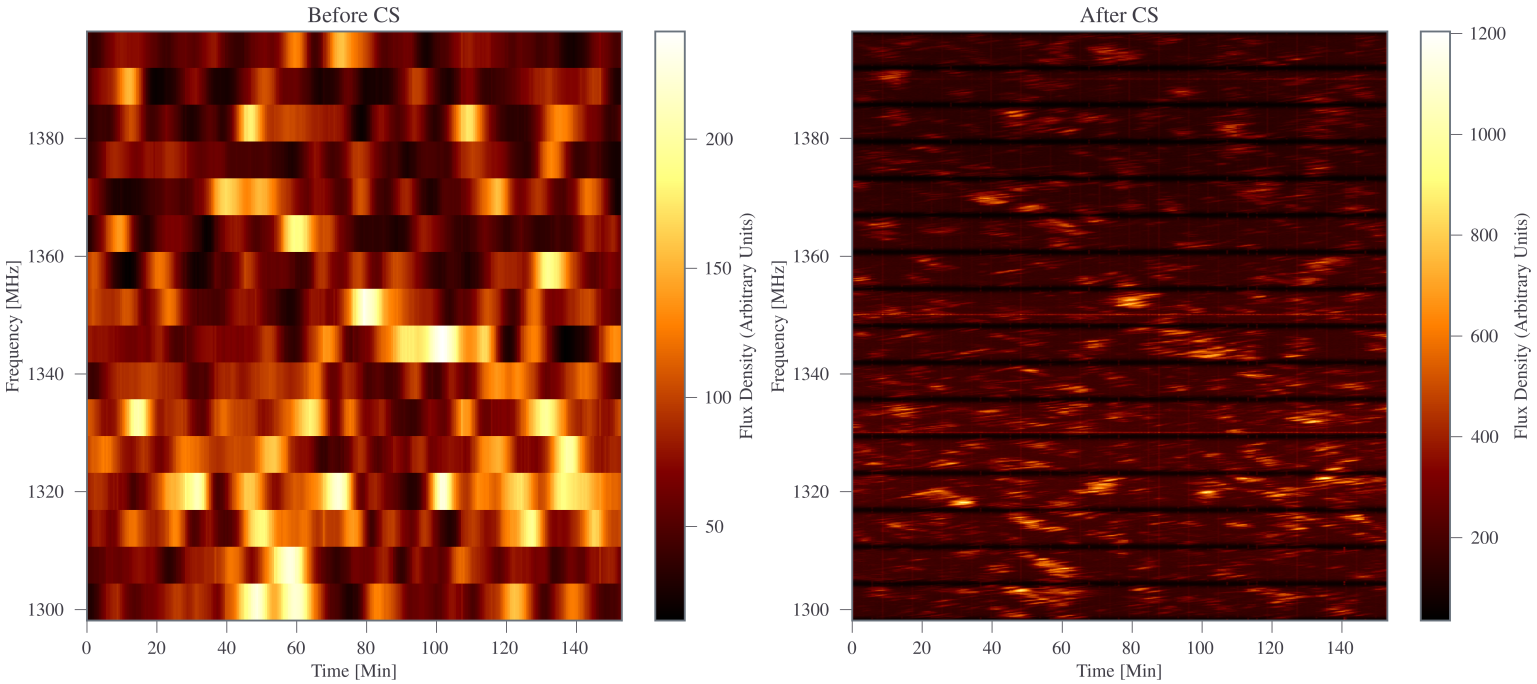


**Figure 5.1:** A 100 MHz slice of the dynamic spectrum on MJD 56198 showing processed data using conventional methods (left) and using cyclic spectroscopy (right), both using 1024 pulse phase bins. The resolution improvement and resulting scintillation structure that emerges as a result of this processing method is quite remarkable.

where $P_{\text{bandpass}}$ is the total power of the observation and $P_{\text{on}}$ and $P_{\text{off}}$ are the power in all on- and off-pulse components, respectively, at each frequency and time. The secondary spectrum for each observation was then acquired by performing a two-dimensional Fourier transform of the dynamic spectrum.

At each frequency slice, to measure the curvature of each arm in a given arc, we followed the approach described in Stinebring et al. (2022) whereby we divided each secondary spectrum along the center of its fringe frequency axis and took slices up the delay axis until we reached the approximate end of a given arm. After we found the maximum in each delay slice, we fit the resulting trend using $f_\nu = \eta f_t^2$, where $f_\nu$ is the differential time delay (Fourier conjugate

variable to observing frequency), $\eta$ is the arc curvature, and $f_t$ is the fringe frequency (Fourier conjugate variable observing time).

To determine our scintillation bandwidth for a given frequency slice, we first acquired the corresponding dynamic spectrum's 2D autocorrelation function (ACF), from which we retrieved its 1D frequency and time ACFs. We then fit the frequency ACFs with a Lorentzian and measured the scintillation bandwidth, $\Delta\nu_{\rm d}$, by finding the half width at half maximum of the frequency ACF fit.

The corresponding scattering delays $\tau_{\rm d}$, were then found via

$$2\pi\Delta\nu_{\rm d}\tau_{\rm d} = C_1, \tag{5.3}$$

where the dimensionless value $C_1$ can range between $0.6 - 1.5$ depending on the geometry of the medium and spectrum of the electron density fluctuations therein (Cordes & Rickett, 1998). In this work we chose $C_1 = 1$, as is common in many scintillation studies (Levin et al., 2016; Chapter, 2; Liu et al., 2022). As with all pulsar scintillation studies, our precision was limited by the number of scintles visible in a given observation, and as such our uncertainties was dominated by this finite scintle effect, which is given by

$$\begin{aligned} \epsilon &\approx \tau_{\rm d} N_{\rm scint}^{-1/2} \\ &\approx \tau_{\rm d}[(1+\eta_{\rm t}T/\Delta t_{\rm d})(1+\eta_\nu B/\Delta\nu_{\rm d})]^{-1/2}, \end{aligned} \tag{5.4}$$

with $N_{\rm scint}$ being the number of scintles observed over the course of the observation, $T$ and $B$ being the total integration time and total bandwidth, respectively, and $\eta_{\rm t}$ and $\eta_\nu$ being filling factors that can range from 0.1 to 0.3 depending on how one defines the characteristic timescale and scintillation bandwidth, which for this chapter are both set to 0.2 (Cordes, 1986a). An example dynamic spectrum, along with its 2D ACF and 1D ACF fits is shown in Figure 5.2. Also of note in our observations, and visible in Figure 5.2, is the strong slant in the 2D ACF, indicating a non-zero scintillation drift rate, $\mathrm{d}\nu/\mathrm{dt}$, indicative of strong refraction in our observations.

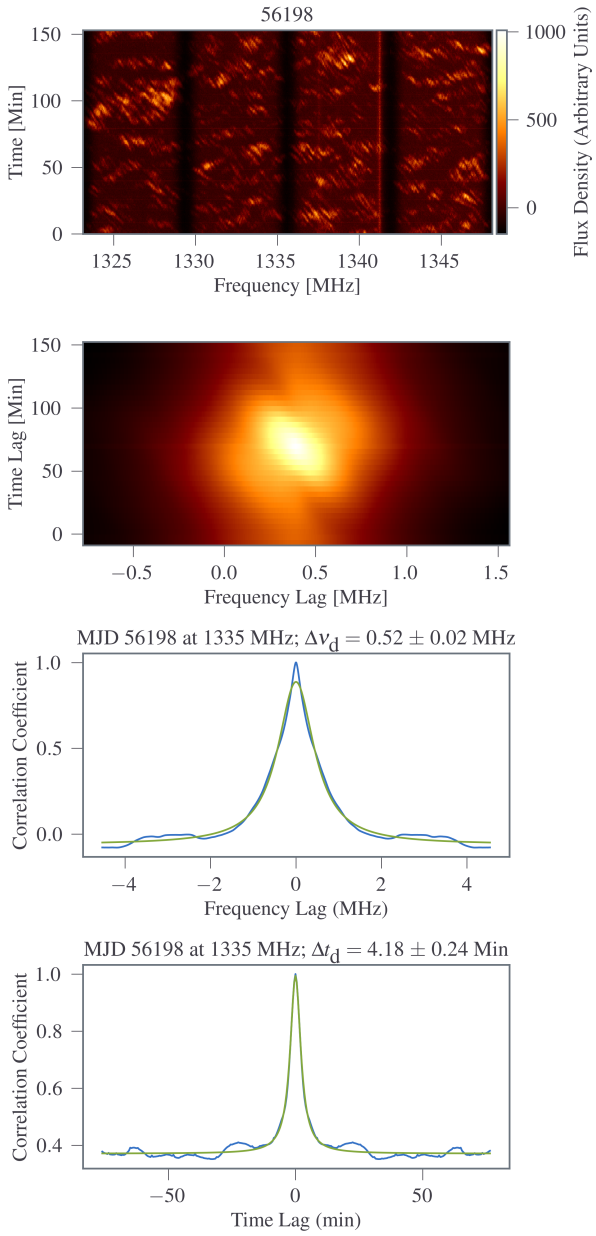


**Figure 5.2:** (Top) A dynamic spectrum from MJD 56198 taken at 1335.625 MHz. (Second from top) The corresponding 2D autocorrelation function. (Second from bottom) The 1D frequency slice (blue) of the 2D autocorrelation function with its corresponding Lorentzian fit (green). (Bottom) The 1D time slice of the 2D autocorrelation function (blue) with its corresponding Lorentzian fit (green). Note the strong slant in the 2D ACF, indicating strong refraction and a non-zero scintillation drift rate (Cordes, 1986a).

Following Hill et al. (2003b), to acquire our scintillation arc scaling indices, which we refer to as $\alpha$, we performed a weighted linear least-squares fit of the form

$$\log_{10} \eta = \alpha \log_{10} \nu + \beta, \tag{5.5}$$

where $\nu$ is the observing frequency, using the measured curvatures of a given arm across all frequency slices within a given MJD.

In an analogous method to Equation 5.5, our scattering delay scaling indices $\xi$ at each epoch were determined by performing a weighted linear least-squares fit of the form

$$\log_{10} \tau_{\rm d} = \xi \log_{10} \nu + b \tag{5.6}$$

across all delay measurements from a given MJD.

## 5.4 Results & Discussion

### 5.4.1 Scintillation Bandwidth Measurements & Scaling

Although scattering delays are not currently accounted for explicitly in PTA timing models, it has been shown that many pulsars can introduce delays on the order of tens to hundreds of nanoseconds (Levin et al., 2016; Chapter, 2; Liu et al., 2022). With the introduction of wideband timing into PTA efforts (Alam et al., 2020c), we can use larger observing bandwidths to improve precision of timing model parameters. However, wider band widths also means a wider range of frequencies over which effects of the ISM can vary in influence. In the North American Nanohertz Observatory for Gravitational Waves (NANOGrav) PTA collaboration, currently, for the most dominant source of delay from the ISM, dispersion measure (DM), wideband measurements of pulse time of arrival (TOA) assume a cold-plasma dispersion law and use an assumed $\nu^{-2}$ dependence to model the DM at a particular epoch. If a similar approach were to be used to account for scattering delays at a given epoch, we might assume the medium

exhibits Kolmogorov turbulence and use a $\nu^{-4.4}$ dependence for scattering delays across the band. However, it has been shown that many LOS frequently deviate from this dependence and have scaling indices that fluctuate across epochs. As such, this approach could result in TOA misestimations of tens to hundreds of nanoseconds depending on the pulsar. For this reason, it becomes crucial to understand how scattering delay vary across these wide observing bands when attempting to correct for scattering effects.

Thanks to our ability to fit eight simultaneous measurements across our observing band, our scattering delay scaling analyses are possibly to most robust scaling index measurement performed at L-band. The results of this effort are shown in Table 5.1, with an example fit from MJD 56206 shown in Figure 5.3.

**Table 5.1:** Fitted Pulsar Scattering Delay Scaling Indices

| MJD | Index |
|---|---|
| 56183 | $-2.40 \pm 0.67$ |
| 56198 | $-3.18 \pm 1.50$ |
| 56206 | $-2.84 \pm 0.67$ |

**Table 5.1:** Fitted scattering delay scaling indices to the eight frequency ACFs across the observing band. Errors are uncertainties from parameter fits. Our measurements are all consistent with a shallower power law than that expected of a Kolmogorov medium, agreeing with previous measurements in the literature.

Our scaling indices agree with those previously been reported in the literature, with sources generally reporting indices between $3-3.6$ within error both on indices averaged over many epochs as well as for individual epochs (Cordes et al., 1990; Ramachandran et al., 2006; Levin et al., 2016; Chapter, 2; Liu et al., 2022), although Levin et al. (2016) reported indices on individual days as shallow as 1 and as steep as 5.

While we have established that the approximation of scattering occurring at a thin screen along the LOS to this pulsar is proper, it is possible that the treatment of this screen

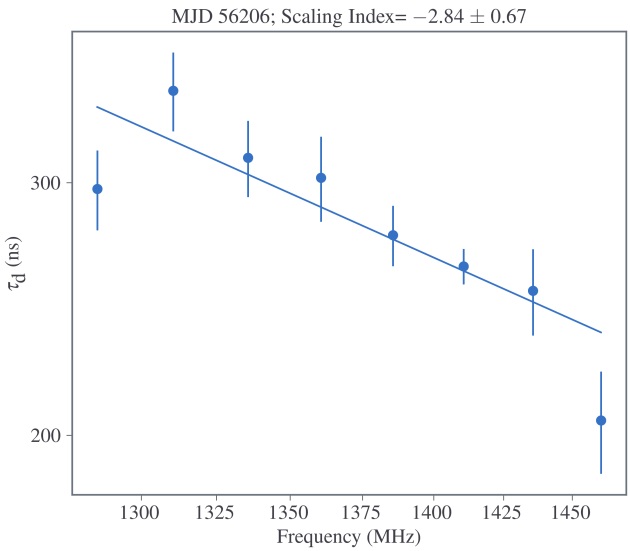


**Figure 5.3:** Example fit for scattering delay scaling index on MJD 56206. Our fits agree well with the scaling indices quoted in the literature.

as infinite is not appropriate, as it has been shown that shallower scaling indices such as the ones seen for this pulsar are more characteristic of finite thin screens (Rickett et al., 2009). It has also been observed that higher DM pulsars in general tend to exhibit shallower scaling laws (Löhmer et al., 2001), although this may also be a consequence of a truncated scattering region.

### 5.4.2 Scintillation Arcs

With our high frequency resolution measurements, we have the ability to analyze the intra-epoch evolution of scintillation arcs across a wide range of frequencies with significant depth, as we were able to resolve a scintillation arc in each of our 25 MHz slices across 200 MHz of bandwidth in all epochs. This represents a substantial improvement in arc sensitivity and indicates the use of cyclic spectroscopy in future studies of MSPs could lead to important developments in our understanding of intra-epoch arc evolution, particularly when observed over the large bandwidths used in PTAs. Some example scintillation arcs with overlaid fits can be seen in Figure 5.4.

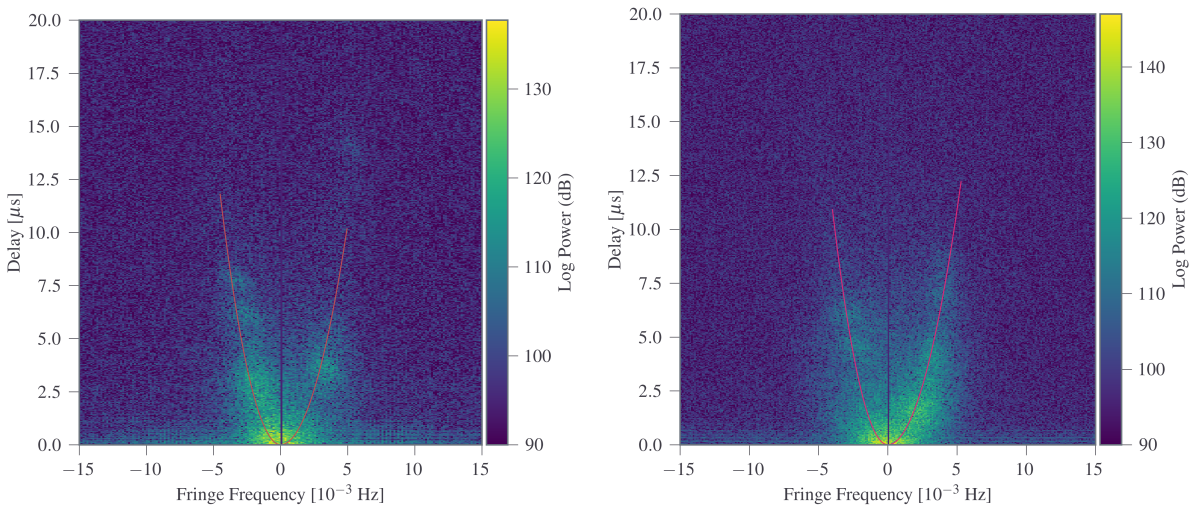


**(a)** Secondary spectrum on MJD 56183 at 1310.625 MHz, with the fits to both arms in the scintillation arc shown in red.

**(b)** Secondary spectrum on MJD 56198 at 1310.625 MHz, with the fits to both arms in the scintillation arc shown in orange.

**Figure 5.4:** Example scintillation arcs with overlaid fits. The blob-like structures in the arcs, known as arclets, indicate AU-scale inhomogeneities within the scattering screen.

#### 5.4.2.1 Arc Features & Evolution Over Frequency

Scintillation arcs for this pulsar have been previously shown once in the literature at 427 MHz also utilizing cyclic spectroscopy (Walker et al., 2013) and twice at L-band using conventional filterbank methods (Main, 2020; Main et al., 2023). While the arc power seen in Main (2020) is roughly symmetric, the arcs in both Walker et al. (2013) and this work all display noticeable asymmetry, believed to be an indicator of refraction (Cordes et al., 2006b). This asymmetry can be quantified by means of an asymmetry index, $A$, describing the relative power between the left and right arms by comparing the average power along each arm via

$$A(f_\nu) = \frac{\overline{P_R(f_\nu)} - \overline{P_L(f_\nu)}}{\overline{P_R(f_\nu)} + \overline{P_L(f_\nu)}}, \tag{5.7}$$

with a larger index magnitude indicating greater asymmetry. As discussed below, we noticed that arc evolution over frequency was more characterized by various features changing in log power than by growing or shrinking on the delay axis. As a result, our asymmetry analysis was limited to a fairly constant $f_\nu$ limit across all frequencies, with a maximum $f_\nu$ of 20 $\mu$s up to 1410 MHz and 10 $\mu$s for 1435 MHz and above.

Given that scintillation drift rates and arc asymmetry are related to refraction, and drift rates exhibit frequency dependent behavior ($\propto \nu^3$) as a result of this relation, one might expect arc asymmetry to also be strongly correlating with observing frequency, linearly or otherwise. This would require multiple arc measurements simultaneously across a range of frequencies and sign reversals in scintillation drifts can occur within hour to day timescales in some cases (Bhat et al., 1999a), although it has been demonstrated through simulations that the bias of the asymmetry may reverse over periods longer than the refractive timescale (Coles et al., 2010). Fortunately for us, there do not appear to be any indications of drift rate sign reversal during individual observations, signaling we are well within a given refractive timescale, making this test feasible. Indeed, an examination of our asymmetry index evolution over observing frequency yields highly linear trends and strong correlations (correlation coefficients with magnitudes between $0.89-0.97$) in all epochs, with the magnitude of the asymmetry index increasing with increasing frequency, confirming this relation. This successfully demonstrates another avenue through which we can quantify the effects of refraction over observing frequency in cyclic spectroscopy-aided PTA measurements. An example asymmetry index evolution over frequency can be seen in Figure 5.5.

Arclets, which are thought to be the result of AU-scale inhomogeneities within the scattering screen (Hill et al., 2005), can be seen in our secondary spectra, and indeed can be seen in all of our scintillation arcs on MJDs 56183 and 56198 in both arms and in the left arm on MJD 56206. These were also seen in the arcs shown in Walker et al. (2013), although only visible in the right arm, which perhaps relatedly is the brighter arc in those observations, but not in Main (2020) or in Main et al. (2023) (they mention their arcs are largely featureless, although they do report some discrete structures in a single epoch), making our observations

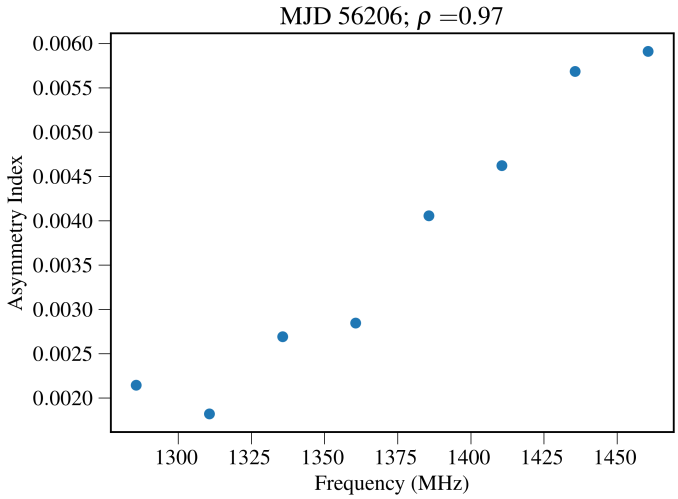


**Figure 5.5:** Asymmetry index vs observing frequency on MJD 56206 with a linear correlation coefficient given by $\rho$. There is a strong relation between the observed asymmetry in the scintillation arcs and the observing frequency, following the behavior seen in other proxies for refraction such as the scintillation drift rate.

the first reported detections of arclets in this pulsar at L-band. Per (Hill et al., 2003b), we expect arcs at lower frequencies to be wider and have more diffuse features. While difficult to discern throughout the evolution in our own arcs, the secondary spectrum seen in Walker et al. (2013) displays arcs agreeing with this expectation.

When examining how the arc structure evolves across observing frequency within our own observations, a consistent behavior across epochs is arcs gradually dimming over frequency, with arclets staying stationary and dimming inward from the cusps to the centers of the arclets. The first structures to fade away are the dim portions of the arc higher up the delay axis and the final structures to remain are the apexes of the arclets, which were in fact the brightest structures in the arc aside from the concentrated power at the base of the fringe frequency axis, which also remains visible. It is well established that pulsar flux decreases with frequency over the ranges we observe (Alam et al., 2020a), and we can quantitatively see this in our dynamic spectra, as the mean and median flux of our 25 MHz frequency slices of these spectra clearly

get progressively smaller at higher frequencies. As a result, it may be that we simply are unable to see some dimmer features in the higher frequency arcs as a consequence.

#### 5.4.2.2 Curvature Measurements & Scaling

The results of our scintillation arc scaling analysis are shown in Table 5.2, with example fits from MJD 56183 shown in Figure 5.6. We can see that the majority of our scaling indices agree with the $\eta \propto \nu^{-2}$ theory laid out in (Hill et al., 2003b), confirming that these arcs scale with frequency following the same power law as the angular deflection of the scattered rays. Other arc curvature analyses of MSPs have been performed (Bhat et al., 2016; Reardon et al., 2020c; Main et al., 2020; Mall et al., 2022), but only one (Bhat et al. 2016) has attempted to fit for frequency-dependent arc curvature evolution in an MSP. Unlike our fits, for which all eight measurements were taken simultaneously within the same observation, their fits used two measurements which were taken two weeks apart. They found a scaling index ($-2.35 \pm 0.07$) steeper than predicted by Hill et al. (2003b), which they attribute to a change in $\mathbf{V}_{\mathrm{eff},\perp}$ between their two epochs, an issue that we do not need to be concerned with for our observations, as all of our measurements for a given scaling fit are taken on the same day, and therefore have the same $\mathbf{V}_{\mathrm{eff},\perp}$. As such, our results mark the first agreement with the predicted arc curvature scaling relation for an MSP.

**Table 5.2:** Fitted Pulsar Scintillation Arc Curvature Scaling Indices

| MJD | Scaling Index Left Arc | Scaling Index Right Arc |
|---|---|---|
| 56183 | $-2.05 \pm 0.68$ | $-1.84 \pm 0.35$ |
| 56198 | $-1.76 \pm 0.16$ | $-1.83 \pm 0.36$ |
| 56206 | $-2.02 \pm 0.59$ | $-1.86 \pm 0.39$ |

**Table 5.2:** Fitted arc curvature scaling indices for both left and right arcs. We can see that the majority of our fits agree with arc curvatures scaling in the same way as angular deflection of the scattered rays Hill et al. (2003b). Different power laws and curvatures of the left and right arms on a given day can largely be attributed to high levels of refraction occurring during these observations.

## 5.5 Conclusions & Future Work

We have used cyclic spectroscopy to improve the frequency resolution of L-band baseband observations of PSR B1937+21 and performed among the most robust pulsar frequency scaling analyses performed at L-band, especially for an MSP. These results have yielded the first arc curvature scaling fits for an MSP that agree with theory, as well as scattering delay scaling indices that match previous observations and the first detection of arclets in this pulsar at L-band.

The thorough analysis in this work made possible through cyclic spectroscopy demonstrates the strong potential for larger scale efforts using this technique and adds to a growing case towards what we hope is its eventual adoption by PTAs as the primary method for correcting for scattering delays through IRF recovery. Many ISM studies on highly scattered pulsars have been limited to narrow bandwidths at low observing frequencies using traditional filterbanks, but future works may be able to incorporate valuable higher frequency data as well. Additionally, the ability to use cyclic spectroscopy to recover a pulsar's IRF through deconvolution (Walker et al., 2013) or other methods (Chapter, 4) adds another element to these studies, especially given that the IRF may present a more accurate picture of the scattering present in a given observation than the traditional ACF fitting approach (Chapter, 4).

Efforts are currently underway at the Green Bank Observatory to implement a real-time or near real-time cyclic spectroscopy backend, with development nearing completion and testing on real data to begin shortly. This will provide exciting opportunities for new science to all pulsar astronomers using this facility, as well as aid in the timing efforts of the NANOGrav

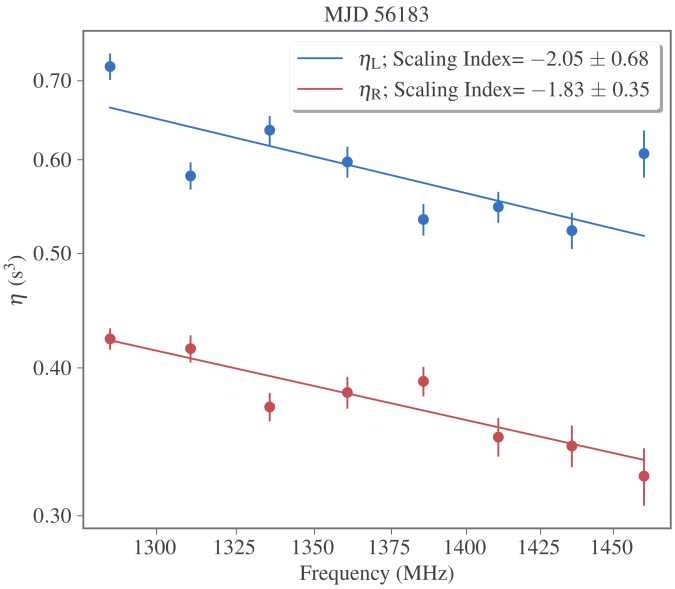


**Figure 5.6:** Scintillation arc curvature scaling indices in both arms on MJD 56183. The fits agree quite well with the frequency dependence of angular deflections as detailed in Hill et al. (2003b). The offset between the two fits can be largely attributed to the strong refraction visible in the scintillation arcs.

PTA collaboration, for whom the 100 meter telescope at the observatory plays a significant role in their efforts to detect low-frequency gravitational waves.

We gratefully acknowledge support of this effort from the NSF Physics Frontiers Center grants 1430284 and 2020265 to NANOGrav. All of the data processing in this work utilized the resources of the Link computing cluster at West Virginia University. We thank the NANOGrav Collaboration for helpful discussions and suggestions, the Noise Budget Working Group in particular. We thank the AO staff for their assistance during the observations reported in this work, in particular P. Perillat, J. S. Deneva, H. Hernandez, and the telescope operators. TD, MAM, and DRS were partially supported through the National Science Foundation (NSF) PIRE program award number 0968296. TD acknowledges NSF AAG award number 2009468 as well as sabbatical and summer leave funding from Hillsdale College.

*Software*: DSPSR (van Straten & Bailes, 2011), ASTROPY (Astropy Collaboration et al., 2013), PYPULSE (Lam, 2017), SCIPY (Virtanen et al., 2020), NUMPY (van der Walt et al., 2011), and MATPLOTLIB (Hunter, 2007).

# Chapter 6. Conclusions

We have examined various properties of interstellar scattering of radio pulsar emission. These studies have allowed for improved understanding of the structure of the interstellar medium across many lines of sight in our Galaxy as well as demonstrated the promise of newer data processing methods for future observations. We have shown that nontrivial amounts of delay from interstellar scattering exist within the NANOGrav 12.5-year data set, the mitigation of which will be crucial for improvement in sensitivity to gravitational wave sources. Simultaneous dual-frequency measurements of bright canonical pulsars revealed rich dynamic spectra and the detections of scintillation arcs, leading to valuable analyses of scintillation evolution across a wide range of observing frequencies. Simulations demonstrated the effectiveness of cyclic spectroscopy at quantifying the degree of interstellar scattering present in data, particularly when compared to conventional autocorrelation function methods. We also applied cyclic spectroscopy to L-band observations of the millisecond pulsar B1937+21 in the first such study using this technique in this frequency range, demonstrating strong promise for the widespread adoption of cyclic spectroscopy by pulsar timing arrays in the near future, particularly with the nearly-completed real-time cyclic spectroscopy observing mode at the Green Bank Observatory.

## 6.1 Assessing the Effects of Scattering Delays Within NANOGrav Data

Understanding and effectively mitigating all sources of non-gravitational wave timing noise in pulsar timing data is crucial to improving the sensitivity of pulsar timing arrays for nanohertz frequency gravitational waves. We used dynamic spectra from the NANOGrav 12.5-year data release to measure scintillation bandwidths and (in some cases) timescales, in many cases across multiple observing bands, from 28 pulsars within this data set.

We determined that in most cases these pulsars exhibit tens to hundreds of nanoseconds of scattering delay that are unaccounted for in current pulsar timing models, with the epoch to epoch variations of the delays for a given pulsar appearing to be directly tied to the dispersion measure of the pulsar. The delays we measured also agreed well with predictions of Galactic electron density models and predictions for how scattering delay should scale with dispersion measure (Bhat et al., 2004; Krishnakumar et al., 2015; Yao et al., 2017; Cordes et al., 2016). We were also able to measure delay scaling indices and found all of them to exhibit shallower behavior than one would expect from a medium displaying Kolmogorov turbulence, with pulsars for which many indices were measured exhibiting minimal changes from epoch to epoch.

Significant number of pulsars had scattering delays measured as upper limits due to unresolved scintles in our dynamic spectra, necessitating the need for finer frequency channelization in our observations. Newer techniques like cyclic spectroscopy (Chapter 4, Chapter 5) will allow for this finer resolution while also allowing for the determination of scattering delays via deconvolution of the intrinsic pulse from the ISM's impulse response function.

## 6.2 Studying Scintillation Arcs Using Simultaneous Dual-Frequency Observations

Scintillation arcs provide a valuable probe of the structure and behavior of the ISM. Examining this behavior over a wide range of frequencies allows for a more thorough probe of the ISM over a wider variety of length scales. We used the Upgraded Giant Metrewave Radio Telescope (uGMRT) to perform simultaneous dual-frequency observations of bright pulsars across 450 MHz of bandwidth at low frequencies. This allowed for examinations of frequency-dependent scintillation properties within the same epoch, whereas similar studies may have multiple days between observations at different frequency bands.

We performed robust scaling law analysis of arc curvature, scintillation bandwidth, and scintillation timescales, which we find to agree with earlier measurements that were taken over multiple epochs and/or contained fewer measurements. We also were able to compare

intra-epoch values of curvature and pseudo-curvature across a wide variety of frequencies, and found general agreement in all epochs, indicating assumptions of one-dimensional, thin screen scattering are valid in these observations. Finally, we found a strong correlation between arc asymmetry and curvature in PSR J1136+1551, which attribute to a bias in the Hough transform method used to determine arc curvatures. Future work on this data, along with upcoming high-cadence measurements of PSR J1136+1551, will perform even more in-depth analsis on this rich data set.

## 6.3 Determining the Effectiveness of Cyclic Spectroscopy at Recovering Scattering Delays in Pulsar Timing Data

Scattering delays are a sizeable but currently uncorrected source of timing noise in pulsar timing data. One highly promising approach for mitigating this noise is with the use of cyclic spectroscopy, which can deconvolve the intrinsic pulse from the impulse response function of the ISM. This would allow for a more direct measure of scattering present in the data, as it uses both the amplitude and phase of the observed signal rather than just the amplitude as is measured in the dynamic spectrum.

We simulated many scattered pulses over a wide range of S/N and compared the precision and accuracy of delays measured from the impulse response function recovered using cyclic spectroscopy and from the scintillation bandwidth measured autocorrelation functions (ACF) of dynamic spectra. While the ACF approach had greater accuracy at low S/N, once the cyclic spectroscopy approach converged at moderate S/N, the latter had noticeably greater precision and accuracy on average compare with the ACF-based estimators, especially as more cyclic frequencies were used. We also found much higher correlation between cyclic spectroscopy-estimated delays and injected delays for individual epochs, which is crucial for effective mitigation in pulsar timing efforts. These results demonstrate strong promise for the upcoming real-time cyclic spectroscopy pipeline at the Green Bank Observatory, which aims to perform cyclic spectroscopy-based deconvolution of the signal as observations are taking place.

## 6.4 Using Cyclic Spectroscopy to Reveal Rich Scintillation Information In L-Band Observations of a Millisecond Pulsar

Cyclic spectroscopy is poised to provide massive benefits to pulsar timing, one of particular significance being significant improvements in frequency resolution. We used cyclic spectroscopy to improve the frequency resolution of L-band observations of the millisecond pulsar PSR B1937+21 by around a factor of 1000, resulting in rich structures being revealed in dynamic and secondary spectra across 200 MHz of bandwidth. The spectra were detailed enough that our observations were able to be broken up into 50 MHz subbands for robust frequency-dependent analyses of arc curvature, scintillation bandwidth and timescale, and arc asymmetry.

Well-resolved arclets were also visible across all subband secondary spectra, allowing for examination of arc structure evolution over frequency. We found the various features within the spectra to get gradually dimmer with increasing frequency, which matches expectations based on flux density spectral index. Clear asymmetries in the arcs across all epochs were also detected. The striking detail made possible through cyclic spectroscopy demonstrates both the power and utility of this processing technique and this paper presents a strong case for the benefits of its widespread adoption within the pulsar timing community.

## 6.5 Looking to the Future

Having finally seen strong evidence of a gravitational wave background, pulsar timing arrays are poised to pave the way for groundbreaking physics discoveries in the near future. To accomplish this goal, further improvements in both precision and accuracy of our detectors are paramount. For this reason, careful mitigation of all non-gravitational wave sources of noise, such as effects from interstellar scattering, will undoubtedly help to unveil this new science.

Cyclic spectroscopy's ability to deconvolve IRFs, which has been demonstrated to be both more precise and accurate than ACF approaches to recovering scattering delays, (Chapter

4), may prove crucial to this effort. We are currently in the final stages of implementation of a real-time cyclic spectroscopy backend at the Green Bank Observatory, which will allow for cyclic spectroscopy-based processing of pulsar timing data either in parallel with or shortly following PTA observations, allowing for speedy and accurate removal/accounting of scattering delays present in data. This backend will also allow for improvements in frequency resolution previously infeasible with PTA observing setups, allowing for significant, high resolution studies of the ISM across tens or hundreds of LOS, providing unparalleled opportunities to study the AU-to-pc-scale structure of our Galaxy.

# References


Ables, J. G., & Manchester, R. N. 1976, , 50, 177

Agazie, G., Anumarlapudi, A., Archibald, A. M., et al. 2023a, The Astrophysical Journal Letters, 951, L8

Agazie, G., Alam, M. F., Anumarlapudi, A., et al. 2023b, The Astrophysical Journal Letters, 951, L9

—. 2023c, The Astrophysical Journal Letters, 951, L9

Alam, M. F., Arzoumanian, Z., Baker, P. T., et al. 2020a, The Astrophysical Journal Supplement Series, 252, 4

—. 2020b, The Astrophysical Journal Supplement Series, 252, 4

—. 2020c, The Astrophysical Journal Supplement Series, 252, 5

Antoni, J. 2007, Mechanical Systems and Signal Processing, 21, 597

Antoniadis, J., Arzoumanian, Z., Babak, S., et al. 2022, , 510, 4873

Antoniadis, J., Babak, S., Bak Nielsen, A. S., et al. 2023, arXiv e-prints, arXiv:2306.16224

Archibald, A. M., Kondratiev, V. I., Hessels, J. W. T., & Stinebring, D. R. 2014, The Astrophysical Journal, 790, L22

Arzoumanian, Z., Brazier, A., Burke-Spolaor, S., et al. 2015a, The Astrophysical Journal, 813, 65

—. 2015b, The Astrophysical Journal, 813, 65

—. 2018, The Astrophysical Journal Supplement Series, 235, 37

Arzoumanian, Z., Baker, P. T., Blumer, H., et al. 2020a, , 905, L34

—. 2020b, , 905, L34

Astropy Collaboration, Robitaille, T. P., Tollerud, E. J., et al. 2013, , 558, A33

Backer, D. C. 1970, Nature, 228, 42

Backer, D. C., Kulkarni, S. R., Heiles, C., Davis, M. M., & Goss, W. M. 1982, , 300, 615

Bansal, K., Taylor, G. B., Stovall, K., & Dowell, J. 2019, The Astrophysical Journal, 875, 146

Bates, S. D., Lorimer, D. R., & Verbiest, J. P. W. 2013, Monthly Notices of the Royal Astronomical Society, 431, 1352

Bhat, N. D. R., Cordes, J. M., Camilo, F., Nice, D. J., & Lorimer, D. R. 2004, The Astrophysical Journal, 605, 759

Bhat, N. D. R., Cordes, J. M., Camilo, F., Nice, D. J., & Lorimer, D. R. 2004, ApJ, 605, 759

Bhat, N. D. R., Gupta, Y., & Rao, A. P. 1999a, The Astrophysical Journal, 514, 249

Bhat, N. D. R., Ord, S. M., Tremblay, S. E., McSweeney, S. J., & Tingay, S. J. 2016, , 818, 86

Bhat, N. D. R., Ord, S. M., Tremblay, S. E., McSweeney, S. J., & Tingay, S. J. 2016, The Astrophysical Journal, 818, 86

Bhat, N. D. R., Rao, A. P., & Gupta, Y. 1999b, The Astrophysical Journal, 514, 272

Bhat, N. D. R., Tremblay, S. E., Kirsten, F., et al. 2018, The Astrophysical Journal Supplement Series, 238, 1

Bilous, A. V., Kondratiev, V. I., Kramer, M., et al. 2016, , 591, A134

Bisnovatyi-Kogan, G. S., & Ruzmaikin, A. A. 1974, , 28, 45

Bracewell, R. 1978, The Fourier Transform and its Applications, 2nd edn. (Tokyo: McGraw-Hill Kogakusha, Ltd.)

Brown, W., & Loomis, H. 1993, IEEE Transactions on Signal Processing, 41, 703

Chapter, J. E. 2, , 917, 10

—. 4, , 944, 191

Chatterjee, S., Brisken, W. F., Vlemmings, W. H. T., et al. 2009, The Astrophysical Journal, 698, 250

Chen, S., Caballero, R. N., Guo, Y. J., et al. 2021, Monthly Notices of the Royal Astronomical Society, 508, 4970

Coles, W. A., Rickett, B. J., Gao, J. J., Hobbs, G., & Verbiest, J. P. W. 2010, ApJ, 717, 1206

Coles, W. A., Kerr, M., Shannon, R. M., et al. 2015, The Astrophysical Journal, 808, 113

Collaboration, T. C., Amiri, M., Bandura, K., et al. 2022, The Astrophysical Journal Supplement Series, 261, 29

Cordes, J., Wharton, R., Spitler, L., Chatterjee, S., & Wasserman, I. 2016, arXiv:1605.05890

Cordes, J. M. 1986a, The Astrophysical Journal, 311, 183

—. 1986b, ApJ, 311, 183

Cordes, J. M. 2002, in Astronomical Society of the Pacific Conference Series, Vol. 278, Single-Dish Radio Astronomy: Techniques and Applications, ed. S. Stanimirovic, D. Altschuler, P. Goldsmith, & C. Salter, 227–250

Cordes, J. M., & Lazio, T. J. W. 2001, The Astrophysical Journal, 549, 997

Cordes, J. M., & Lazio, T. J. W. 2002, ArXiv:astro-ph/0207156, arXiv:astro-ph/0207156

Cordes, J. M., & Lazio, T. J. W. 2002, NE2001.I. A New Model for the Galactic Distribution of Free Electrons and its Fluctuations, arXiv:astro-ph/0207156

—. 2003, NE2001. II. Using Radio Propagation Data to Construct a Model for the Galactic Distribution of Free Electrons, arXiv:astro-ph/0301598

Cordes, J. M., Pidwerbetsky, A., & Lovelace, R. V. E. 1986, ApJ, 310, 737

Cordes, J. M., & Rickett, B. J. 1998, The Astrophysical Journal, 507, 846

Cordes, J. M., & Rickett, B. J. 1998, ApJ, 507, 846

Cordes, J. M., Rickett, B. J., Stinebring, D. R., & Coles, W. A. 2006a, ApJ, 637, 346

—. 2006b, , 637, 346

Cordes, J. M., & Shannon, R. M. 2010, A Measurement Model for Precision Pulsar Timing, arXiv:1010.3785

Cordes, J. M., Shannon, R. M., & Stinebring, D. R. 2016, , 817, 16

Cordes, J. M., Weisberg, J. M., & Boriakoff, V. 1985, ApJ, 288, 221

Cordes, J. M., Weisberg, J. M., & Boriakoff, V. 1985, , 288, 221

Cordes, J. M., Wolszczan, A., Dewey, R. J., Blaskiewicz, M., & Stinebring, D. R. 1990, , 349, 245

Demorest, P. B. 2011, MNRAS, 416, 2821

Demorest, P. B. 2011, MNRAS, 416, 2821

Demorest, P. B., Ferdman, R. D., Gonzalez, M. E., et al. 2012, The Astrophysical Journal, 762, 94

Dirson, L., Pétri, J., & Mitra, D. 2022, , 667, A82

Dolch, T., Stinebring, D. R., Jones, G., et al. 2020, arXiv e-prints, arXiv:2008.10562

Dolch, T., Stinebring, D. R., Jones, G., et al. 2021, The Astrophysical Journal, 913, 98

DuPlain, R., Benson, J., & Sessoms, E. 2008, in Advanced Software and Control for Astronomy II, ed. A. Bridger & N. M. Radziwill, Vol. 7019, International Society for Optics and Photonics (SPIE), 467 – 476

Ford, J. M., Demorest, P., & Ransom, S. 2010, in Software and Cyberinfrastructure for Astronomy, ed. N. M. Radziwill & A. Bridger, Vol. 7740, International Society for Optics and Photonics (SPIE), 127 – 139

Foster, R. S., & Backer, D. C. 1990, , 361, 300

Foster, R. S., & Backer, D. C. 1990, ApJ, 361, 300

Gardner, W. 1987, IEEE Transactions on Communications, 35, 584

Goncharov, B., Shannon, R. M., Reardon, D. J., et al. 2021, The Astrophysical Journal Letters, 917, L19

Gupta, Y., Rickett, B. J., & Lyne, A. G. 1994, , 269, 1035

Gupta, Y., Ajithkumar, B., Kale, H. S., et al. 2017, Current Science, 113, 707

Güver, T., Özel, F., Göğüş, E., & Kouveliotou, C. 2007, The Astrophysical Journal, 667, L73

Hankins, T. H., & Rickett, B. J. 1975, in Methods in Computational Physics Volume 14 — Radio Astronomy (New York: Academic Press), 55–129

Hazboun, J. S., Simon, J., Madison, D. R., et al. 2022, The Astrophysical Journal, 929, 39

Heger, A., Fryer, C. L., Woosley, S. E., Langer, N., & Hartmann, D. H. 2003, , 591, 288

Hemberger, D. A., & Stinebring, D. R. 2008a, The Astrophysical Journal, 674, L37

—. 2008b, ApJ, 674, L37

Hesse, K. H., & Wielebinski, R. 1974, , 31, 409

Hewish, A. 1980, , 192, 799

Hill, A. S., Stinebring, D. R., Asplund, C. T., et al. 2005, ApJL, 619, L171

Hill, A. S., Stinebring, D. R., Barnor, H. A., Berwick, D. E., & Webber, A. B. 2003a, ApJ, 599, 457

—. 2003b, The Astrophysical Journal, 599, 457

Hobbs, G. B., Edwards, R. T., & Manchester, R. N. 2006, , 369, 655

Hotan, A. W., van Straten, W., & Manchester, R. N. 2004, , 21, 302

Huguenin, G. R., Taylor, J. H., Goad, L. E., et al. 1968, , 219, 576

Hunter, J. D. 2007, Computing in Science & Engineering, 9, 90

Johnston, S., Nicastro, L., & Koribalski, B. 1998, Monthly Notices of the Royal Astronomical Society, 297, 108

Jones, M. L., McLaughlin, M. A., Lam, M. T., et al. 2017, The Astrophysical Journal, 841, 125

Jones, M. L., McLaughlin, M. A., Lam, M. T., et al. 2017, , 841, 125

Keith, M. J., Coles, W., Shannon, R. M., et al. 2013, Monthly Notices of the Royal Astronomical Society, 429, 2161

Komesaroff, M. M. 1970, Nature, 225, 612

Kramer, M., Xilouris, K. M., Lorimer, D., et al. 1998, ApJ, 501, 270

Kramer, M., Xilouris, K. M., Lorimer, D. R., et al. 1998, , 501, 270

Krishnakumar, M. A., Joshi, B. C., & Manoharan, P. K. 2017, The Astrophysical Journal, 846, 104

Krishnakumar, M. A., Maan, Y., Joshi, B. C., & Manoharan, P. K. 2019, The Astrophysical Journal, 878, 130

Krishnakumar, M. A., Mitra, D., Naidu, A., Joshi, B. C., & Manoharan, P. K. 2015, , 804, 23

Kuzmin, A., Losovsky, B. Ya., Jordan, C. A., & Smith, F. G. 2008, A&A, 483, 13

Lam, M., McLaughlin, M., Cordes, J., Chatterjee, S., & Lazio, T. 2017, The Astrophysical Journal, 861, doi:10.3847/1538-4357/aac48d

Lam, M. T. 2017, PyPulse: PSRFITS handler, ascl:1706.011

Lambert, H. C., & Rickett, B. J. 2000, ApJ, 531, 883

Large, M. I., Vaughan, A. E., & Wielebinski, R. 1968, , 220, 753

—. 1969, , 223, 1249

Lentati, L., Kerr, M., Dai, S., et al. 2017, Monthly Notices of the Royal Astronomical Society, 468, 1474

Levin, L. 2015, in Journal of Physics Conference Series, Vol. 610, Journal of Physics Conference Series, 012020

Levin, L., McLaughlin, M. A., Jones, G., et al. 2016, The Astrophysical Journal, 818, 166

Lewandowski, W., Dembska, M., Kijak, J., & Kowalińska, M. 2013a, Monthly Notices of the Royal Astronomical Society, 434, 69

—. 2013b, Monthly Notices of the Royal Astronomical Society, 434, 69

Lewandowski, W., Kijak, J., Gupta, Y., & Krzeszowski, K. 2011, , 534, A66

Liu, Y., Verbiest, J. P. W., Main, R. A., et al. 2022, , 664, A116

Löhmer, O., Kramer, M., Mitra, D., Lorimer, D. R., & Lyne, A. G. 2002, The Astrophysical Journal, 562, L157

Lommen, A. N., & Demorest, P. 2013, Classical and Quantum Gravity, 30, 224001

Lorimer, D. R., & Kramer, M. 2004, Handbook of Pulsar Astronomy, Vol. 4

Löhmer, O., Kramer, M., Mitra, D., Lorimer, D. R., & Lyne, A. G. 2001, The Astrophysical Journal, 562, L157

Maan, Y., van Leeuwen, J., & Vohl, D. 2021, , 650, A80

Main, R. 2020, international Pulsar Timing Array 2020 Conference

Main, R., van Kerkwijk, M., Pen, U.-L., Mahajan, N., & Vanderlinde, K. 2017, The Astrophysical Journal Letters, 840, L15

Main, R. A., Sanidas, S. A., Antoniadis, J., et al. 2020, , 499, 1468

Main, R. A., Sanidas, S. A., Antoniadis, J., et al. 2020, Monthly Notices of the Royal Astronomical Society, 499, 1468

Main, R. A., Parthasarathy, A., Johnston, S., et al. 2023a, , 518, 1086

Main, R. A., Antoniadis, J., Chen, S., et al. 2023b, , 525, 1079

Main, R. A., Antoniadis, J., Chen, S., et al. 2023, Variable Scintillation Arcs of Millisecond Pulsars observed with the Large European Array for Pulsars, arXiv:2306.13462

Mall, G., Main, R. A., Antoniadis, J., et al. 2022, Monthly Notices of the Royal Astronomical Society, 511, 1104

Manchester, R. N., Hobbs, G. B., Teoh, A., & Hobbs, M. 2005a, , 129, 1993

—. 2005b, , 129, 1993

Manchester, R. N., Hobbs, G., Bailes, M., et al. 2013, , 30, e017

McKee, J. W., Lyne, A. G., Stappers, B. W., Bassa, C. G., & Jordan, C. A. 2018, Monthly Notices of the Royal Astronomical Society, 479, 4216

McKee, J. W., Zhu, H., Stinebring, D. R., & Cordes, J. M. 2022, , 927, 99

McKee, J. W., Zhu, H., Stinebring, D. R., & Cordes, J. M. 2022, The Astrophysical Journal, 927, 99

McKee, J. W., Stappers, B. W., Bassa, C. G., et al. 2019, , 483, 4784

McLaughlin, M. A. 2013, Classical and Quantum Gravity, 30, 224008

McLaughlin, M. A., Arzoumanian, Z., Cordes, J. M., et al. 2002, The Astrophysical Journal, 564, 333

McLaughlin, M. A., Lyne, A. G., Lorimer, D. R., et al. 2006, Nature, 439, 817

Narayan, R., & Goodman, J. 1989, Monthly Notices of the Royal Astronomical Society, 238, 963

Nicastro, Nigro, F., D'Amico, N., Lumiella, V., & Johnston, S. 2001, A&A, 368, 1055

O'Dell, S. L., & Sartori, L. 1970, , 162, L37

Osłowski, S., & Walker, M. A. 2023, , 519, 1261

Palliyaguru, N., Stinebring, D., McLaughlin, M., Demorest, P., & Jones, G. 2015, The Astrophysical Journal, 815, 89

Pilkington, J. D. H., Hewish, A., Bell, S. J., & Cole, T. W. 1968, , 218, 126

Ramachandran, R., Demorest, P., Backer, D. C., Cognard, I., & Lommen, A. 2006, , 645, 303

Ramachandran, R., Mitra, D., Deshpande, A. A., McConnell, D. M., & Abies, J. G. 1997, Monthly Notices of the Royal Astronomical Society, 290, 260

Rankin, J. M., Comella, J. M., Craft, H. D., J., et al. 1970, , 162, 707

Rankin, J. M., & Counselman, C. C., I. 1973, , 181, 875

Reardon, D. J., Coles, W. A., Hobbs, G., et al. 2019, Monthly Notices of the Royal Astronomical Society, 485, 4389

Reardon, D. J., Coles, W. A., Bailes, M., et al. 2020, , 904, 104

Reardon, D. J., Coles, W. A., Bailes, M., et al. 2020a, The Astrophysical Journal, 904, 104

—. 2020b, The Astrophysical Journal, 904, 104

—. 2020c, The Astrophysical Journal, 904, 104

Rickett, B., Johnston, S., Tomlinson, T., & Reynolds, J. 2009, Monthly Notices of the Royal Astronomical Society, 395, 1391

Rickett, B. J. 1975, , 197, 185

Rickett, B. J. 1977, Ann. Rev. Astr. Ap., 15, 479

—. 1990, Annual Review of Astronomy and Astrophysics, 28, 561

Rickett, B. J., Coles, W. A., Nava, C. F., et al. 2014, The Astrophysical Journal, 787, 161

Roberts, N., Lorimer, D., Kramer, M., et al. 2005, Handbook of Pulsar Astronomy, Cambridge Observing Handbooks for Research Astronomers (Cambridge University Press)

Roberts, R., Brown, W., & Loomis, H. 1991, IEEE Signal Processing Magazine, 8, 38

Romani, R. W., Narayan, R., & Blandford, R. 1986, , 220, 19

Ruderman, M. A., & Sutherland, P. G. 1975, , 196, 51

Scheuer, P. A. G. 1968, , 218, 920

Shapiro-Albert, B. J., Hazboun, J. S., McLaughlin, M. A., & Lam, M. T. 2021, The Astrophysical Journal, 909, 219

Shapiro-Albert, B. J., McLaughlin, M. A., Lam, M. T., Cordes, J. M., & Swiggum, J. K. 2020, The Astrophysical Journal, 890, 123

Sprenger, T., Main, R., Wucknitz, O., Mall, G., & Wu, J. 2022, Monthly Notices of the Royal Astronomical Society, 515, 6198

Staelin, D. H., & Reifenstein, Edward C., I. 1968, Science, 162, 1481

Staff, G. S. 2017, Green Bank Observatory Proposer's Guide for the Green Bank Telescope, `https://science.nrao.edu/facilities/gbt/proposing/GBTpg.pdf`, [Accessed 22-08-2023]

Stinebring, D. R., Faison, M. D., & McKinnon, M. M. 1996, , 460, 460

Stinebring, D. R., McLaughlin, M. A., Cordes, J. M., et al. 2001a, ApJ, 549, L97

—. 2001b, , 549, L97

—. 2001c, , 549, L97

Stinebring, D. R., Rickett, B. J., & Ocker, S. K. 2019, , 870, 82

Stinebring, D. R., Smirnova, T. V., Hankins, T. H., et al. 2000a, ApJ, 539, 300

—. 2000b, The Astrophysical Journal, 539, 300

Stinebring, D. R., Rickett, B. J., Minter, A. H., et al. 2022, The Astrophysical Journal, 941, 34

Stovall, K., Ray, P. S., Blythe, J., et al. 2015, The Astrophysical Journal, 808, 156

Susobhanan, A., Maan, Y., Joshi, B. C., et al. 2021, , 38, e017

Tarafdar, P., Nobleson, K., Rana, P., et al. 2022, , 39, e053

Trang, F. S., & Rickett, B. J. 2007, , 661, 1064

van der Walt, S., Colbert, S. C., & Varoquaux, G. 2011, Computing in Science Engineering, 13, 22

van Kerkwijk, M. H., & van Lieshout, R. 2022, mhvk/screens: v0.1, doi:10.5281/zenodo.7455536

van Straten, W., & Bailes, M. 2011, , 28, 1

Virtanen, P., Gommers, R., Oliphant, T. E., et al. 2020, Nature Methods, 17, 261

Walker, M. A., Demorest, P. B., & van Straten, W. 2013, , 779, 99

Walker, M. A., Demorest, P. B., & van Straten, W. 2013, The Astrophysical Journal, 779, 99

Walker, M. A., Koopmans, L. V. E., Stinebring, D. R., & van Straten, W. 2008, MNRAS, 388, 1214

Walker, M. A., Melrose, D. B., Stinebring, D. R., & Zhang, C. M. 2004, , 354, 43

Walker, M. A., & Stinebring, D. R. 2005, , 362, 1279

Wang, N., Manchester, R. N., Johnston, S., et al. 2005, MNRAS, 358, 270

Wu, Z., Verbiest, J. P. W., Main, R. A., et al. 2022, , 663, A116

Yao, J. M., Manchester, R. N., & Wang, N. 2017, The Astrophysical Journal, 835, 29

Zic, A., Reardon, D. J., Kapur, A., et al. 2023, arXiv e-prints, arXiv:2306.16230

# Appendix A: Derivation of Fractional Error and Uncertainty As Related To Observable Quantities

The following work uses Equations A9 and A10 of Appendix A of Dolch et al. (2021). The first part of A9 defines cyclic merit as

$$m_{\rm cyc} = \frac{b}{\delta b}, \tag{A.1}$$

where $b = 2\pi\tau_{\rm CS}/P$ and $\delta b = 2\pi\delta\tau_{\rm CS}/P$, while equation A10 defines it as

$$m_{\rm cyc} = \frac{2\pi\tau_{\rm CS}W_e}{P^2}({\rm S/N})\sqrt{\sum_k k^2 a_k}, \tag{A.2}$$

where $W_e$ is the effective pulse width and $a_k = A_k/A_0$, the ratio of the k$^{\rm th}$ coefficient and the 0$^{\rm th}$ coefficient of the intensity pulse profile's Fourier transform. For a sharp pulse, Fourier coefficients should stay substantial out to some high number $k_{\rm max}$ before falling off rapidly, with the number of cyclic frequencies we go up to being roughly the inverse of the duty cycle. This means that $k_{\rm max}$ should be roughly $P/W_e$. If we assume that $a_k$ stays constant out to $k_{\rm max}$, the radical becomes

$$\sqrt{\sum_{k=1}^{k_{\rm max}} k^2} = \sqrt{\frac{k_{\rm max}(k_{\rm max}+1)(2k_{\rm max}+1)}{6}} \approx \sqrt{k_{\rm max}^3} \approx \left(\frac{P}{W_e}\right)^{3/2}. \tag{A.3}$$

From here we can say that

$$\frac{b}{\delta b} \approx \frac{2\pi\tau_{\rm CS}W_e}{P^2}({\rm S/N})\left(\frac{P}{W_e}\right)^{3/2} = \frac{2\pi\tau_{\rm CS}({\rm S/N})}{\sqrt{PW_e}}. \tag{A.4}$$

We can then express this inverse fractional error as

$$\frac{b}{\delta b} = \frac{2\pi\tau_{\mathrm{CS}}}{P\delta b} = \frac{2\pi\tau_{\mathrm{CS}}(\mathrm{S/N})}{\sqrt{PW_e}} \tag{A.5}$$

$$\implies \delta b = \sqrt{\frac{W_e}{P}}\frac{1}{(\mathrm{S/N})}, \tag{A.6}$$

meaning the uncertainty in $\tau_{\mathrm{CS}}$ can be expressed as

$$\delta\tau_{\mathrm{CS}} = \frac{\sqrt{PW_e}}{2\pi(\mathrm{S/N})}. \tag{A.7}$$